# High Efficiency Mid and Deep Ultraviolet Optoelectronic Devices

by

Ayush Pandey

A dissertation submitted in partial fulfillment
of the requirements for the degree of
Doctor of Philosophy
(Electrical and Computer Engineering)
in the University of Michigan
2021

Doctoral Committee:

Professor Pallab Bhattacharya, Co-Chair
Professor Zetian Mi, Co-Chair
Associate Professor Emmanouil Kioupakis
Professor Mackillo Kira

Ayush Pandey

ayushp@umich.edu

ORCID iD: 0000-0002-9582-3709

© Ayush Pandey 2021

**Acknowledgements**

Firstly, I will thank my doctoral advisors, Professor Zetian Mi and Professor Pallab Bhattacharya for the tremendous support and guidance since I initially started working with them in mid-2016, as a master's student. Their dedication as mentors, attention to detail, and advice has helped me to evolve as a researcher. Numerous discussions with them have helped to broaden my understanding of this fast-paced area of research and explore new avenues. The resources that they provided have proven invaluable in bringing my ideas from the realm of theory into practical realities. They are truly exceptional role models for any researcher who is looking to further advance in their field.

I would like to also thank the members of my dissertation committee – Professor Mack Kira and Professor Emmanouil Kioupakis. They have been valuable collaborators in several projects, providing insightful suggestions and directions for future research.

I am grateful for the contributions, company and knowledge provided by current and former group members. My early mentors included Dr. Arnab Hazari, Dr. Aniruddha Bhattacharya, Dr. David Laleyan, Dr. Anthony Aiello and Dr. Yuanpeng Wu. Group members who joined later have helped me design and perform several experiments, and discussions with them have been a veritable font of knowledge. In no particular order, I would like to thank Dr. Xianhe Liu, Dr. Srinivas Vanka, Dr. Yongjie Wang, Dr. Ping Wang, Dr. Yi Sun, Dr. Debabrata Das, Dr. Tinh Tran, Dr. Ding Wang, Dr. Baowen Zhu, Walter Shin, Eric Reid, Yakshita Malhotra, Kishwar Mashooq, Majid Aalizadeh, Ishtiaque Navid, Chiyo Ahn, Boyu Wang, Zhenwei Ye, Wan

Jae Dong, Peng Zhou, Nick Pant, Chan Ho Soh, Yongbum Park, Yongjin Ma, Yixin Zhao and Ronglei Fan.

Collaborators are an intrinsic part of research, and I would like to thank Dr. Jiseok Gim. Zihao Deng, and Professor Robert Hovden from the Materials Science and Engineering Department at the University of Michigan for their contributions. I am also grateful to Subhajit Mohanty, Kamruzzaman Khan, Ashley Jian, Professor Jamie Phillips, and Professor Elaheh Ahmadi from the Electrical Engineering and Computer Science Department at the University of Michigan for their assistance and the use of their equipment.

Significant portions of my research work involved using the facilities provided by the University of Michigan. Primarily, the Lurie Nanofabrication Facility, which is staffed with a team of engineers that maintain and calibrate the sophisticated equipment used there. Without their ceaseless work, the facility would soon fall into chaos. I am grateful to Dennis Schweiger, Dr. Sandrine Martin, Dr. Pilar Herrera-Fierro, Nadine Wang, Vishva Ray, Katharine Beach, Kevin Owen, Shawn Wright, Brandon Woo, Matthew Oonk, Samuel Edwards, David Sebastian, Steven Sostrom, Jorge Barreda, Tony Sebastian, Terre Briggs and Gregg Allion. I am also grateful to Ying Qi at the X-Ray Micro-Analysis Laboratory for her help in operating the X-ray diffraction equipment.

I would also like to thank the several friends I made in Ann Arbor, especially those made at the co-op I stayed at for the majority of my studies, and those I made at the tennis courts whacking tennis balls after a frustrating day of research.

Finally, I would like to thank my family, scattered as it is. Despite having oceans separating us, and not seeing each other for several years, we remain tight knit. Their infinite love and support for my decisions have been a solid foundation, pushing me forward in my work.

## Table of Contents

Acknowledgements ii
List of Tables vii
List of Figures viii
List of Appendices xvi
Abstract xvii
Chapter 1. Introduction 1
1.1 Ultraviolet Light and Its Applications 1
1.2 Light Emitting Diodes 2
1.3 III-Nitride Semiconductors 5
1.4 Polarization Field in III-Nitrides 7
1.4.1 High Electron Mobility Transistors 9
1.4.2 Polarization Effects in Optical Devices 10
1.4.3 Polarization-Induced Doping 10
1.4.4 Polarization-Engineered Tunnel Junctions 11
1.5 Current State of III-Nitride Optoelectronic Devices 12
1.6 Challenges Facing AlGaN LEDs 13
1.6.1 Role of Threading Dislocations on IQE 14
1.6.2 Low Extraction of TM-polarized Light 15
1.6.3 Poor p-type Doping 17
1.6.4 Carrier Overflow from Active Region 18
1.7 Recent Developments in AlGaN UV LED Technology 18
1.7.1 Improvement of Material Quality 18
1.7.2 Approaches for Enhanced Light Extraction 20
1.7.3 Advances in p-type Doping 22
1.7.4 New Heterostructure Designs 22
1.7.5 AlGaN-based Nanostructures 23
1.8 Dissertation Overview 24
Chapter 2. Methods 27

2.1 Overview 27
2.2 Molecular Beam Epitaxy 27
2.2.1 Epitaxial Growth 29
2.2.2 Advantages of MBE 31
2.2.3 Challenges with MBE 32
2.2.4 MBE Growth of AlGaN 32
2.3 Optical Material Characterization Techniques 35
2.3.1 Photoluminescence Spectroscopy 35
2.3.2 Time-Resolved Photoluminescence Spectroscopy 36
2.3.3 Spectroscopic Ellipsometry 36
2.4 Structural Characterization Techniques 37
2.4.1 X-Ray Diffraction 37
2.4.2 Scanning Electron Microscopy 38
2.4.3 Scanning Transmission Electron Microscopy 38
2.4.4 Atomic Force Microscopy 39
2.4.5 Secondary Ion Mass Spectrometry 39
2.5 Electrical and Device Characterization Techniques 40
2.5.1 Hall Measurements 40
2.5.2 Current-Voltage Measurements 41
2.5.3 LED Power Measurements 41
2.5.4 Electroluminescence Spectroscopy 42
Chapter 3. Enhanced Doping Efficiency of Ultrawide Bandgap Semiconductors by Metal-Semiconductor Junction Assisted Epitaxy 43
3.1 Author Contribution and Copyright Disclaimer 43
3.2 Background 43
3.3 Epitaxial Growth of Mg-doped AlGaN 48
3.4 Effect of Growth Method on Mg Incorporation 50
3.5 Low-Resistivity p-type AlGaN Layers 52
3.6 UV LED Fabrication and Measurements 55
3.7 Summary 57
Chapter 4. Effect of Electron Blocking Layer on AlGaN UV LED Efficiency 59
4.1 Author Contribution and Copyright Disclaimer 59
4.2 Background 59
4.3 Epitaxy of UV LED Structures 62
4.4 Fabrication and Characterization of Mid-UV LEDs 64

4.5 Summary 68

Chapter 5. High Efficiency AlGaN/GaN/AlGaN Tunnel Junction UV LEDs 70

5.1 Author Contribution and Copyright Disclaimer 70

5.2 Overview 70

5.3 Epitaxial Growth of LEDs 73

5.4 Structural Characterization of the LED Structure 75

5.5 Tunnel Junction Design Optimization 76

5.6 Characterization of Optimized Tunnel Junction Device 80

5.7 Summary 84

Chapter 6. An AlGaN Tunnel Junction Light Emitting Diode Operating at 255 nm 85

6.1 Author Contribution and Copyright Disclaimer 85

6.2 Overview 85

6.3 Device Structure Epitaxy and Structural Characterization 88

6.4 LED Fabrication and Characterization 91

6.5 Role of Temperature on LED Performance 96

6.6 Summary 98

Chapter 7. Electron Overflow of AlGaN Deep Ultraviolet Light Emitting Diodes 99

7.1 Author Contribution and Copyright Disclaimer 99

7.2 Introduction 99

7.3 Tunnel Junction UV LEDs Structure and Growth 102

7.4 LED Fabrication and Comparison 104

7.5 Optical Measurements of Active Region 110

7.6 Summary 113

Chapter 8. Summary and Future Work 114

8.1 Summary 114

8.2 Future Work 116

8.2.1 Using Nanostructures for AlGaN Devices 116

8.2.2 Extending Tunnel-Junction UV LEDs to Shorter Wavelengths 118

8.2.3 Substrate Removal 119

8.2.4 P-doping using Beryllium as Dopant 120

8.2.5 Understanding the Carrier Dynamics in AlGaN UV Devices 121

8.2.6 Development of UV-C Laser Diodes Using MBE 121

Appendices 123

Bibliography 136

## List of Tables

Table 1.1: Material Properties of wurtzite III-nitride semiconductors [5-7]. 6

Table 4.1: AlGaN mid-UV LED samples with different EBL designs. 63

Table 5.1: List of tunnel junction LED structures. 74

Table C.1: Formation energy and activation energy of neutral Mg dopants on different substitutional sites on $Al_{0.5}Ga_{0.5}N$ under metal-rich conditions. 132

.

## List of Figures

Figure 1.1: An illustration of the electromagnetic spectrum. The marked region indicates the most effective wavelength range for sterilizing pathogens. (Source [1]) 1

Figure 1.2: Schematic of an LED. (Source [2]) 2

Figure 1.3: Bandgaps and lattice constants of III-nitride materials. (Source [4]) 5

Figure 1.4: Wurtzite crystal structure. (Source [8]) 7

Figure 1.5: Polarization direction and sheet charge density for AlGaN/GaN heterostructure [11].8

Figure 1.6: Structure and band-diagram of a typical AlGaN/GaN HEMT [13]. 9

Figure 1.7: Band diagram of a conventional III-nitride quantum well in equilibrium [20]. 10

Figure 1.8: Band-diagram of a compositionally graded AlGaN layer on GaN [21]. 11

Figure 1.9: Energy band diagram of a p-n junction (top) and a polarization-engineered tunnel junction (bottom) [26]. 12

Figure 1.10: Plot of EQE of UV LEDs vs. emission wavelengths. (Source [37]) 13

Figure 1.11: Variation of maximum IQE for different dislocation densities at different wavelengths. (Source: [42]) 15

Figure 1.12: (a) Schematic of extraction of light for TE and TM polarized emission [45]. (b) Band structure for AlGaN with a high Al composition [46]. (c) Comparison of LEE for a planar structure and different configurations of photonic crystal structures [44]. 16

Figure 1.13: (a) Activation energy of Mg acceptor dopant for different Al composition AlGaN [50]. (b) Formation energy of Mg substitutional incorporation in AlN under N-rich and metal-rich growth regimes [51]. 18

Figure 1.14:(a) Schematic of a growth on a patterned sapphire substrate [64]. (b) Cross-sectional SEM image of AlN wafer grown using epitaxial lateral overgrowth [65]. (c) Image of an AlN single crystal substrate produced by Hexatech, Inc. [66]. 19

Figure 1.15:(a) Schematic of an LED die with encapsulation [87]. (b) Schematic of an LED that has had its substrate removed [88]. (c) Schematic of an LED with a photonic crystal etched into the top contact layer [82]. (d) SEM image of a selective-area growth nanowire photonic crystal [83]. 21

Figure 1.16:(a) Cross-sectional TEM image of a spontaneously grown nanowire [114]. (b) Elemental mapping of the marked region from Fig. 1.16(a). (c) SEM image of an SAG nanowire photonic crystal. 24

Figure 2.1: An image of the Veeco Gen930 MBE system used in this work. 28

Figure 2.2: Schematic of RHEED operation [123]. 29

Figure 2.3: Schematic representation of the film growth modes. (Source: [130] ) 30

Figure 2.4:(a) SEM image of Ga droplets on the surface of AlGaN immediately after growth. (b) Crystalline defect formed at Ga droplet. 34

Figure 2.5: Schematic of the photoexcitation process in a semiconductor [146]. 35

Figure 2.6: Schematic of the TRPL setup. 36

Figure 2.7: Schematic of the ellipsometry technique [147]. 37

Figure 2.8:(a) Schematic of the XRD experiment [148]. (b) A Rigaku SmartLab XRD system. 38

Figure 2.9: Diagram of the Hall effect [149]. 40

Figure 3.1:(a) Schematic of conventional epitaxy. (b) Energy band diagram of the Mg-doped AlGaN layer during conventional epitaxy. (c) Schematic of metal-semiconductor junction assisted epitaxy, with the presence of a liquid Ga layer on the surface during epitaxy. (d) Energy band diagram at the growth front of Mg-doped AlGaN during metal-semiconductor junction assisted epitaxy, showing the pinning of the surface Fermi level away from the valence band edge. (e) Calculated formation energy for Mg substitution in GaN, AlN, and $Al_{0.5}Ga_{0.5}N$ as a function of the separation between the Fermi level and the valence band with substitutional Mg formation energies for the different growth processes indicated by their respective arrows. 45

Figure 3.2:(a) Mg atom concentration versus depth obtained from SIMS measurements on Mg-doped $Al_{0.75}Ga_{0.25}N$ grown using metal-semiconductor junction assisted epitaxy and conventional epitaxy. (b) Mg concentration versus the Mg flux for Mg-doped $Al_{0.75}Ga_{0.25}N$ grown using metal-semiconductor junction assisted epitaxy and conventional epitaxy. (c) Photoluminescence spectra of a Mg-doped $Al_{0.75}Ga_{0.25}N$ sample grown using metal-semiconductor junction assisted epitaxy with band-edge peak and Mg-acceptor peak shown with arrows. 50

Figure 3.3: Room-temperature Hall measurement data for Mg-doped AlGaN epilayers plotted against Al composition, showing (a) free hole concentration, (b) hole mobility, (c) resistivity and (d) resistivities of Mg-doped AlGaN layers obtained from literature and this work. 52

Figure 3.4: Temperature dependent Hall measurement of Mg-doped AlGaN epilayers grown by metal-semiconductor junction assisted, with Al content between 75% and 90%, for (a) hole concentration, (b) hole mobility and (c) resistivity plotted against the inverse of temperature. 54

Figure 3.5:(a) EL spectrum for an UV LED grown using metal-semiconductor junction assisted epitaxy. (b) I-V characteristics for LEDs grown using metal-semiconductor junction assisted epitaxy and conventional epitaxy. (c) EQE versus current density for these devices. 56

Figure 4.1: Schematic illustration of AlGaN mid-UV LEDs with the incorporation of (a) a p-type AlN/AlGaN superlattice EBL and (b) an n-type AlN/AlGaN superlattice EBL. Equilibrium energy band diagram for the LED heterostructures with (c) a p-type AlN/AlGaN superlattice EBL and (d) an n-type AlN/AlGaN superlattice EBL. 62

Figure 4.2: I-V characteristics for AlGaN mid-UV LEDs measured at room temperature. Blue curve: LED A with 10× p-AlN/$Al_{0.7}Ga_{0.3}N$ superlattice EBL; Black curve: LED B with 10× n-AlN/$Al_{0.7}Ga_{0.3}N$ superlattice EBL; Red curve: LED C with 20× n-AlN/$Al_{0.7}Ga_{0.3}N$ superlattice EBL. The inset shows a top-emitting 100 μm × 100 μm device from sample B at a current density of ~50 A/cm$^2$. 64

Figure 4.3: (a) Normalized electroluminescence spectra measured at 100 A/cm$^2$ at room temperature for LED A (10× p-AlN/$Al_{0.7}Ga_{0.3}N$ superlattice EBL) and LED B (10× n-AlN/$Al_{0.7}Ga_{0.3}N$ superlattice EBL). (b) Spectral linewidths versus current density for LEDs A and B. (c) Peak wavelength versus current density for LEDs A and B. The measurement error bars are also shown in (b) and (c). 66

Figure 4.4:(a) EQE (b) power density, and (c) WPE versus current density measured at room temperature for LED A (10× p-AlN/$Al_{0.7}Ga_{0.3}N$ superlattice EBL), LED B (10× n-AlN/$Al_{0.7}Ga_{0.3}N$ superlattice EBL), and LED C (20× n-AlN/$Al_{0.7}Ga_{0.3}N$ superlattice EBL). 67

Figure 5.1:(a) Schematic illustration of the tunnel junction LED structures. (b) Simulated equilibrium band diagram for a representative LED using a 5 nm GaN layer. The different layers used in the structure are labelled and shown with different colors. 73

Figure 5.2:(a) HAADF-STEM overview of cross-sectional AlGaN multilayers shows the complete device structure. (b) High-resolution HAADF-STEM of the p-AlGaN/GaN/n-AlGaN tunnel junction shows crystalline epitaxial growth with sharp interfaces for enhanced hole injection by tunneling. (c) Atomic-resolution HAADF-STEM of $Al_{0.6}Ga_{0.4}N$ quantum wells coupled to $Al_{0.85}Ga_{0.15}N$ barriers with sharp epitaxial interfaces for carrier confinement. 75

Figure 5.3:(a) I-V characteristics of tunnel junction LED samples A and B, with 2.5 nm GaN layer width and different thicknesses, 50 nm and 150 nm respectively, of top $n^+$-AlGaN contact layer. (b) I-V characteristics of samples B, C and D grown with the same thickness of top $n^+$-AlGaN but different GaN layer widths of 2.5 nm, 5 nm and 10 nm, respectively. Variations of (c) EQE and (d) WPE with injected current density, for samples B, C and D. 77

Figure 5.4: I-V characteristics of an optimized tunnel junction LED from sample E with a GaN layer thickness of 5 nm and top $n^+$-AlGaN contact layer thickness ~480 nm. 80

Figure 5.5 (a) Electroluminescence spectra measured at different injection currents for a representative tunnel junction LED. The inset shows an electroluminescence spectrum measured at 25 $A/cm^2$ current density with the intensity in log scale. (b) Variations of peak position (red circles) and spectral linewidth (black squares) vs. injected current density. 81

Figure 5.6:(a) Variations of (b) EQE and (c) WPE with injected current density for an LED from sample E. 83

Figure 6.1:(a) Schematic tunnel junction deep UV LED. The tunnel junction is shown in the marked region. (b, c) Atomic scale HAADF-STEM images of an $Al_{0.75}Ga_{0.25}N$ layer showing the presence of nanoscale Ga-rich layers due to compositional variation. The brighter regions correspond to higher Ga content. FFT shows the superlattice peak (red arrows) associated with atomic ordering in wurtzite AlGaN along c-plane direction. (d) SEM image of the sample surface

after epitaxial growth showing a smooth surface over a wide area. (e) High-resolution AFM scan of the sample surface after epitaxial growth. (f) Photoluminescence spectrum of the sample measured using a 193 nm laser for excitation at room temperature. 88

Figure 6.2:(a) J-V characteristic of the tunnel junction deep UV LED. The inset shows an LED under a CW bias injection current of ~10 A/cm$^2$. (b) RT EL spectra measured at different injection currents. Inset: EL spectrum at an injection current of 10 A/cm$^2$ measured from 200 nm to 500 nm, showing the absence of defect-related emission. (c) Plot of the peak positions of the EL spectra at different injected current densities. (d) Variation of the FWHM extracted from the EL spectra recorded at different injected current densities. 92

Figure 6.3:(a) EQE and (b) WPE of the tunnel junction deep UV LED vs. current density measured under CW bias at room temperature. (c) EQE and (d) WPE of the tunnel junction deep UV LED measured using pulsed bias with a 0.5% duty cycle. Error bars are provided. 94

Figure 6.4:(a) J-V characteristics at different temperatures for a tunnel junction deep UV LED. (b) Inverse of the ideality factor extracted from the J-V curves plotted against temperature. (c) EL spectra for a device at different temperatures, under the same injection current. (d) Variation of the peak emission wavelength with temperature. 96

Figure 7.1: (a) Schematic of the different tunnel junction UV LED device structures fabricated. (b) HAADF-STEM image of the complete device structure of Sample A. (c) Atomic-scale HAADF-STEM image of the tunnel junction region. FFT shows the superlattice peak associated with atomic ordering in wurtzite Al(Ga)N along c-plane direction. (d) Atomic-scale HAADF-STEM image of the active region. FFT shows the superlattice peak associated with atomic ordering in wurtzite AlGaN along c-plane direction. 102

Figure 7.2: (a) J-V characteristics of the different tunnel junction UV LED device structures. (b) Room-temperature electroluminescence spectra measured for the different devices under current injection densities ~40 A/cm$^2$. The electroluminescence of sample B has been magnified by a factor of 100. The inset shows a device from sample A under an injection current of ~100 A/cm$^2$. (c) Electroluminescence spectra measured at polarization angles of 0˚ and 90˚ for sample A (245 nm), shown as straight lines, and an identical device with emission at 265 nm, shown as dashed lines. (d) Variation of electroluminescence intensity with polarization angle measured for sample A (245 nm) in red, and an identical device with emission at 265 nm, in purple. 106

Figure 7.3:(a) EQE vs. current density of Sample A and C, measured using CW bias. (b) WPE vs. current density of Sample A and C, measured using CW bias. 109

Figure 7.4:(a) Structure of the sample used for optical measurements. (b) Room-temperature photoluminescence spectra for the structure measured using 193 nm excitation. (c) Intensity-dependent photoluminescence spectra measured for the sample using quasi-resonant excitation of the active region. (d) Relative EQE measured for optical emission at different excitation powers. (e) Variation of peak position with excitation power density. (f) Plot of measured full-width half maximum for the emission peak at different excitation power densities. 110

Figure 7.5:(a) Time-resolved photoluminescence decays at different excitation powers collected for the sample used in optical measurements. (b) Plot of extracted carrier lifetime vs. excitation power density. 112

Figure 8.1: (a) SEM image of an N-polar nanowire array. (b) EL spectra of a green-emitting N-polar nanowire LED. 117

Figure 8.2:(a) SEM image of N-polar AlGaN nanowires grown by SAG. (b) PL spectrum of AlGaN nanowire array. 118

Figure 8.3: Schematics of (a) the growth and peeling-off process of AlGaN DUV LED structure on graphene. (b) The growth and laser lift-off process of AlGaN DUV LED structure on sacrificial layer/sapphire. (c) The device fabrication process of transferred AlGaN DUV LED. 120

Figure 8.4: SEM images of etched GaN ridges. 122

Figure B.1: Etching to form device mesa. 126

Figure B.2: Schematic of the sample after deposition of insulation layer. 127

Figure B.3: Etching of vias and contact deposition. 127

Figure C.1: Band structure at the growth interface during the growth of Mg-doped AlGaN by (a) conventional epitaxy and (b) metal-semiconductor junction assisted epitaxy. 133

Figure C.2: SEM images of the sample surface of p-AlGaN grown using (a) conventional epitaxy and (b) metal-semiconductor junction assisted epitaxy. RHEED patterns for (c) conventional epitaxy and (d) metal-semiconductor junction assisted epitaxy. 134

Figure C.3:Mg atom concentration plotted against Mg flux for samples grown using metal-semiconductor junction assisted epitaxy with different Al compositions. 135

**List of Appendices**


Appendix A Substrate Preparation for MBE Growth 124

Appendix B Fabrication Procedure for AlGaN Epilayer LEDs 125

Appendix C Supporting Information for Chapter 3 130

Section 1: Theoretical Calculations 130

Section 2: RHEED Pattern during Epitaxy 133

Section 3: Mg Incorporation in AlGaN Epilayers 135

**Abstract**

Ultraviolet (UV) light is a critical component of future technological products, having applications in curing polymers, sensors, medical diagnostics, as well as in the sterilization of pathogens – a need which is of prime importance to curtail the spread of diseases and possibly a future pandemic. Solid state UV devices can replace existing sources, such as mercury lamps and xenon lamps, by providing non-hazardous, scalable, easy to use, durable, compact and more efficient performance. The III-nitride material system has established itself as the basis for optoelectronic devices operating in the visible and ultraviolet (UV) wavelength range. While InGaN-based devices have already been commercialized for visible light applications, demonstrating a high external quantum efficiency (EQE) and wall-plug efficiency (WPE), the adoption of AlGaN-based UV devices has been hindered due to their correspondingly lower efficiencies. The primary reasons for the low efficiency of AlGaN LEDs include the low internal quantum efficiency because of defects and dislocations in the device active region, inadequate light extraction due to the primarily transverse-magnetic (TM) polarized light emission, and inefficient carrier injection efficiency from the poor p-type doping of the wide band-gap materials. In this work, we have investigated the design, epitaxy, fabrication and characterization of high efficiency AlGaN devices operating in the mid and deep UV wavelength regime.

We used molecular beam epitaxy (MBE) to grow high-quality Mg-doped AlGaN layers under slightly Ga-rich conditions. The unique growth conditions pinned the Fermi level away from the valence band during epitaxy, which improved Mg incorporation by over an order of magnitude as compared to conventional epitaxy. We demonstrated Mg-doped AlGaN layers having Al

compositions up to 90% with resistivities several orders of magnitude lower than previous reports, which is further supported by the dramatically improved EQE of LEDs with emission at 280 nm grown using this technique.

Despite significantly improving the p-type doping, the disparity in the electron and hole concentrations and mobilities is large for Si-doped and Mg-doped AlGaN, respectively. The imbalance of the electron and hole injection to the active region can cause reduced injection efficiency. To address this issue, we investigated different electron-blocking layers (EBLs) and their positioning. We demonstrated that by placing the EBL before the active region as an n-type EBL, instead of a conventional p-type EBL, the flow of electrons can be impeded without hindering hole transport.

We have also utilized polarization-engineered tunnel junctions to increase the hole injection from the p-contacts, which is a critical challenge for wide-bandgap AlGaN. The thickness of the critical tunnel junction layer was optimized for an LED at 265 nm, and we demonstrated a maximum EQE of 11%, the highest value ever reported for devices operating at this wavelength. We also extended this heterostructure design towards shorter wavelengths. Extensive temperature-dependent optical and electrical measurements of 245 and 255 nm LEDs indicate the pivotal role of carrier overflow on device performance and efficiency.

This work provides a unique path for achieving high efficiency mid and deep UV LEDs that were not previously possible. The techniques developed here can be extended to even shorter wavelengths to maximize the efficiency of UV-C AlGaN light sources. Future work includes the development of AlGaN mid and deep UV laser diodes and UV-C and far UV-C LEDs with efficiency comparable to commercial blue LEDs.

# Chapter 1. Introduction

## 1.1 Ultraviolet Light and Its Applications

Light in the ultraviolet (UV) range of the electromagnetic spectrum consists of high-energy photons having a wavelength in between ~10 nm and ~400 nm. It is broadly divided into three parts – UV-A (315-400 nm), UV-B (280-315 nm) and UV-C (<280 nm), depending on the wavelength. These light sources have a variety of useful commercial applications including sensing, curing of polymers, treatment of organic pollutants, and high-speed data storage. UV-B and UV-C light also have the potential to cause damage to DNA, making human exposure dangerous to them. This property, however, makes them crucial aids in the sterilization of pathogens. Figure 1.1 shows the light spectrum with the effective range for sterilization marked. Widespread adoption of such tools can play a vital role in curbing the spread of transmittable diseases, and possibly prevent a future pandemic.

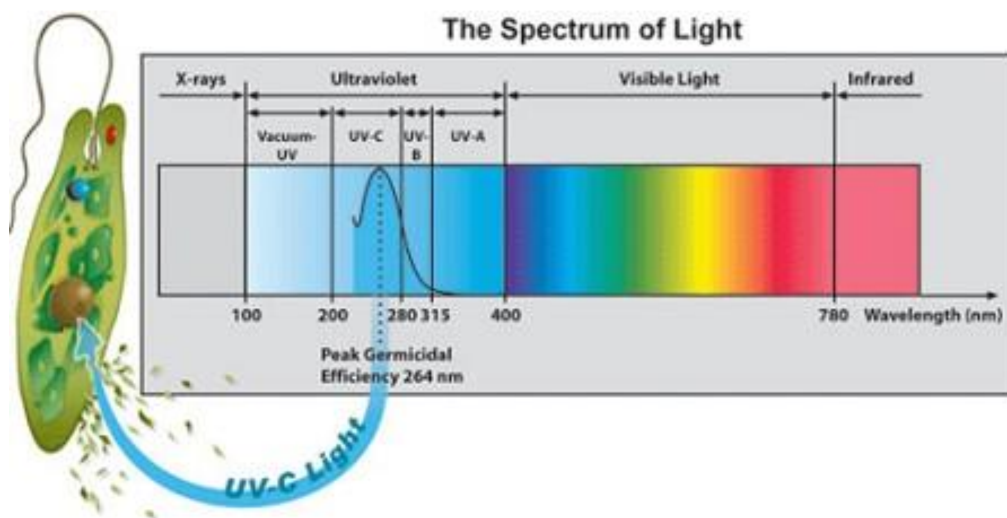


*Figure 1.1: An illustration of the electromagnetic spectrum. The marked region indicates the most effective wavelength range for sterilizing pathogens. (Source [1])*

However, at present most sources of ultraviolet light rely on the use of mercury or gas mixtures, which result in them being potentially hazardous, as well as quite bulky. Efficient semiconductor based optoelectronic devices can provide safe, compact, reliable and easily scalable sources of ultraviolet light, opening up new avenues for their application.

## 1.2 Light Emitting Diodes

Light emitting diodes (LEDs) are optoelectronic devices that use charge carrier recombination to convert an electrical input into an optical output. As they are based on semiconductor technology, these devices are easily scalable, have long lifetimes, are safe to use, and their emission properties can be varied by changing the design and composition of the layers comprising the device. The devices consist of a p-n diode that is specifically designed to maximize radiative recombination. The structure can also comprise of different materials, to tailor the emission properties. Holes are injected from the p-doped region of the semiconductor, and electrons are injected from an n-doped region and they recombine within the device active region to generate light. A schematic of an LED device is shown in Fig. 1.2.

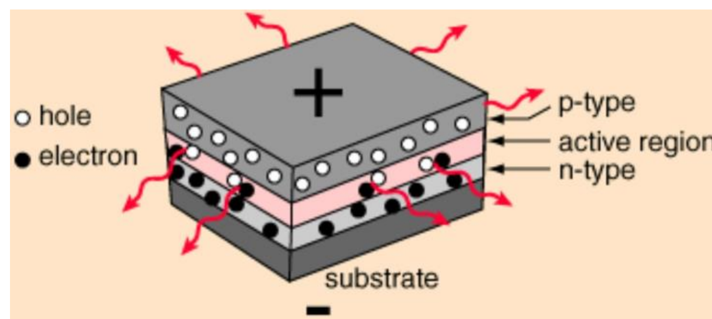


*Figure 1.2: Schematic of an LED. (Source [2])*

The emission wavelength of an LED depends on the bandgap of the semiconductor where recombination takes place, which is generally the active region. The wavelength can be changed by tuning the composition of the active region, or by using quantum confinement effects. As an LED relies on spontaneous emission, the emission spectrum is broad and incoherent, making the full-width half-maximum (FWHM) of the emission peak an important parameter for comparison.

The electrical properties of an LED are dominated by the doping of the n-type and p-type layers. Insufficient doping can result in delayed turn-on voltages and more resistive devices. These factors would increase the energy losses incurred during operation, reducing the electrical to optical energy conversion efficiency.

The internal quantum efficiency (*IQE*) of an LED is defined as the ratio of photons that are generated through radiative recombination to the total number of electrons injected into the device, as shown in Equation 1.1.

$$IQE = \frac{Photons\ generated\ in\ active\ region}{Electrons\ injected\ to\ active\ region} \qquad \text{(Equation 1.1)}$$

As the IQE is a parameter that strongly depends on the material and its quality, it can be characterized using the *ABC* model [3]:

$$IQE = \frac{Bn^2}{An+Bn^2+Cn^3} \qquad \text{(Equation 1.2)}$$

where $n$ is the carrier concentration, A is the Shockley-Read-Hall (SRH) recombination coefficient, B is the radiative recombination coefficient, and C is the Auger recombination coefficient. The numerator in Equation 1.2 corresponds to the ratio of carriers that recombine to produce light, and the denominator corresponds to the total carriers that recombine within the active region. These parameters depend strongly on the composition and bandgap of the active region, as well as the quality of the grown layers, such as the presence of defects. A high quality active region is crucial to maximizing radiative emission and hence the IQE.

For the carriers injected into the device, not all of them will be injected into the active region, as they can recombine outside it, or pass through it because of leakage paths. The injection efficiency (*IE*) of an LED is defined as the ratio of electrons that are injected into the active region divided by the total electrons injected into the device, as described in Equation 1.3.

$$IE = \frac{Electrons\ injected\ into\ active\ region}{Electrons\ injected\ into\ device} \qquad \text{(Equation 1.3)}$$

Once light is generated within the device active region, not all of the photons are able to escape due to internal loss mechanisms, absorption as well as total internal reflection. The ratio of photons that can escape from the device and be collected, to the total number of generated photons is defined as the light extraction efficiency (*LEE*), shown in Equation 1.4.

$$LEE = \frac{Photons\ emitted\ out\ of\ the\ device}{Photons\ generated\ in\ the\ device} \qquad \text{(Equation 1.4)}$$

The external quantum efficiency (*EQE*) of an LED is defined as the ratio of photons emitted from the device to the total carriers injected into it. It can be calculated as shown in Equation 1.5:

$$EQE = IQE \times IE \times LEE \qquad \textit{(Equation 1.5)}$$

For practical applications of an LED, it is also important to know the energy conversion efficiency of electrical to optical power. This parameter is defined by the wall-plug efficiency (*WPE*) in Equation 1.6:

$$WPE = \frac{Power\ of\ optical\ output}{Power\ of\ electrical\ input} \qquad \textit{(Equation 1.6)}$$

## 1.3 III-Nitride Semiconductors

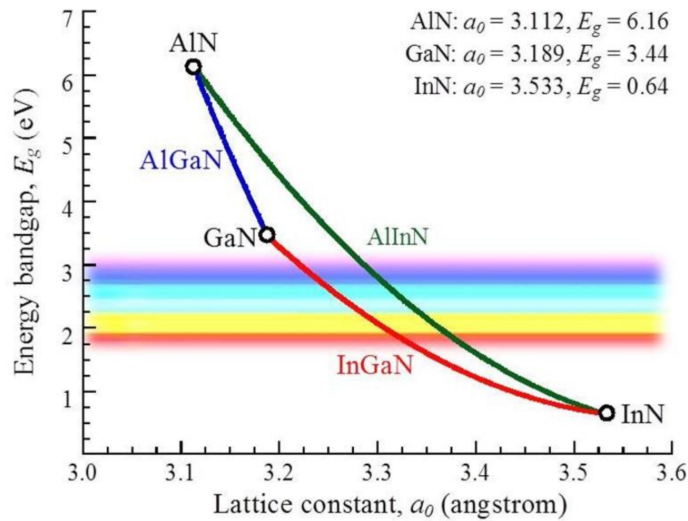


*Figure 1.3: Bandgaps and lattice constants of III-nitride materials. (Source [4])*

The III-nitride material system consists primarily of AlN, GaN and InN and their alloys. The three binary semiconductors are direct bandgap materials with bandgaps spanning from 6.1

eV for AlN, to 0.7 eV for InN as shown in Fig. 1.3. These properties make them attractive candidates for visible and ultraviolet optoelectronic devices, as well as for high-power electronic devices. A summary of the material characteristics are provided in Table 1.1.

*Table 1.1: Material Properties of wurtzite III-nitride semiconductors [5-7].*

| **Property** | **AlN** | **GaN** | **InN** |
|---|---|---|---|
| Bandgap $E_g$ (eV) | 6.1 | 3.44 | 0.7 |
| a (nm) | 0.3111 | 0.3189 | 0.3544 |
| c (nm) | 0.4978 | 0.5185 | 0.5718 |
| Spontaneous Polarization ($C/m^2$) | -0.081 | -0.029 | -0.032 |
| Piezoelectric Coefficient $e_{33}$ ($C/m^2$) | 1.46 | 0.73 | 0.97 |
| Piezoelectric Coefficient $e_{31}$ ($C/m^2$) | -0.6 | -0.49 | -0.57 |

The III-nitrides are commonly used in their wurtzite crystal phase, as shown in Fig. 1.4. However, the bonding in the structure is asymmetric, which results in a strong spontaneous polarization field in the materials. The direction of this field is determined by the direction of the crystal – it is directed towards the substrate for metal polarity and towards the surface for nitrogen polarity. The polarization fields are further compounded by the effect of piezoelectric polarization due to the large lattice mismatch between the individual binary compounds, which results in mechanical stress during their epitaxial growth.

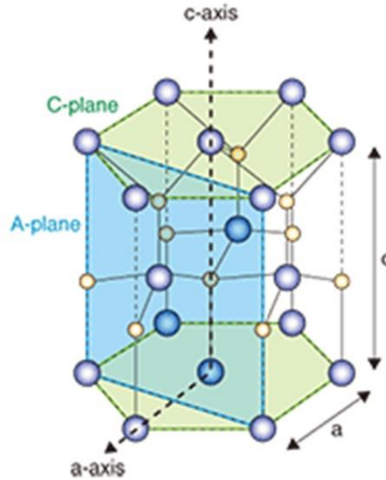


*Figure 1.4: Wurtzite crystal structure. (Source [8])*

Furthermore, having the ability to controllably dope semiconductors is essential to realizing practical devices. While GaN can be doped both n-type and p-type, using Si and Mg as donor and acceptor impurities, respectively, it remains challenging for ultra-wide bandgap AlGaN alloys, especially the p-type doping.

### 1.4 Polarization Field in III-Nitrides

As mentioned previously, the III-nitrides have an inbuilt spontaneous polarization field due to the strongly ionic nature of the chemical bonds and the asymmetric crystal structure, which exists without an external electric field [9, 10]. This results in a net dipole moment within each unit cell. The spontaneous polarization charge for the binary unit cells are included in Table 1.1 [6]. The spontaneous polarization field direction lies along the c-axis of the wurtzite crystal, with the direction being dependent on the polarity of the crystal. For growth with a Ga-polar crystal orientation the spontaneous polarization field points towards the substrate, while in the case of N-polar crystals it points towards the surface.

Furthermore, as there is a significant mismatch in the lattice constants of the individual III-nitride binaries, as well as typical substrates, the grown layers are also put under either compressive or tensile strain. The strain results in a piezoelectric polarization field which is aligned with the spontaneous polarization for tensile strain, while it is opposed for compressive strain. The net effect of the combination of the fields is shown in Fig. 1.5.

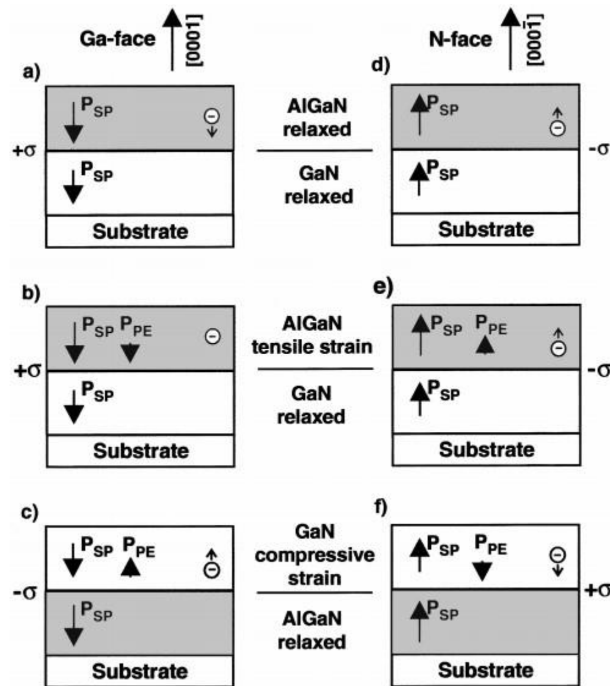


*Figure 1.5: Polarization direction and sheet charge density for AlGaN/GaN heterostructure [11].*

The presence of the strong polarization can result in the generation of huge charge densities at heterointerfaces, which by using Gauss' Law $\sigma = -\nabla \cdot \vec{P}$, will create an electric field of the MV order within the active layer of devices that will have a profound impact on device performance. It is also important to note that the vast difference in spontaneous polarization between AlN and

GaN, coupled with the relatively small mismatch in lattice constants, implies that for AlGaN based heterostructures spontaneous polarization will have a dominant effect, while for InGaN based heterostructures piezoelectric polarization will be of more importance. Some consequences of the polarization are elaborated on below.

### *1.4.1 High Electron Mobility Transistors*

As can be seen from Fig. 1.5, it is possible to generate large electric fields within AlGaN/GaN heterostructures, that result in the formation of 2D carrier gasses at the heterointerface, depending on the stacking and orientation of the structure. The carrier concentration of the 2D carrier gasses is very high from the large electric fields, and they have extremely high mobility due to the absence of impurity scattering from dopants. These properties have been utilized for developing high power and high speed transistors [12]. A schematic and corresponding band-structure of a typical GaN high electron mobility transistor (HEMT) is shown in Fig. 1.6.

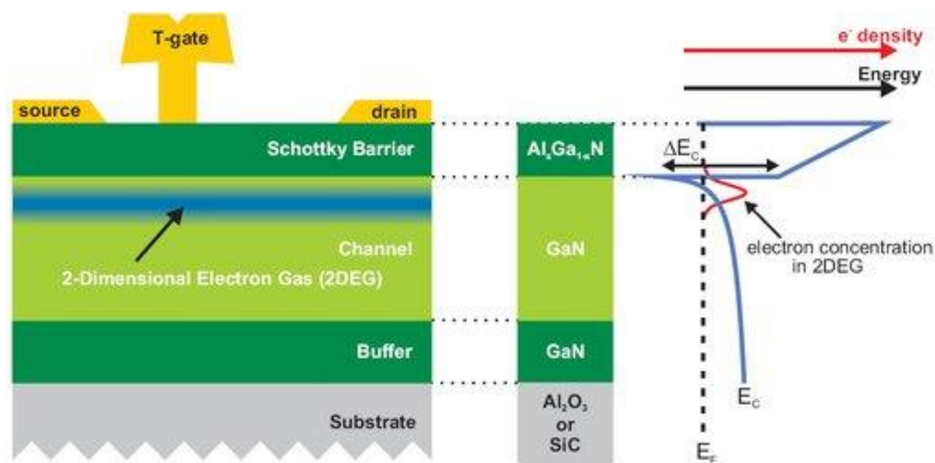


*Figure 1.6: Structure and band-diagram of a typical AlGaN/GaN HEMT [13].*

### 1.4.2 Polarization Effects in Optical Devices

The band diagram of a typical III-nitride quantum well is shown in Fig. 1.7, with the electron and hole wavefunctions also marked. The presence of the polarization fields results in a strong band-bending within the quantum well that has a strong impact on radiative efficiency and carrier dynamics under injection [14-17]. The presence of the electric field spatially separates the wavefunctions of the holes and electrons within the quantum well, decreasing the probability for radiative carrier recombination [18]. Another effect observed at high injections is the quantum confined Stark effect, where a blue-shift in emission wavelength is seen as injection increases. This is because initially at low injection the tilt of the bands reduces the effective bandgap, however as the injection increases, the polarization field is screened by the injected carriers [17, 19]. This effectively flattens the bands, causing a blue shift in emission.

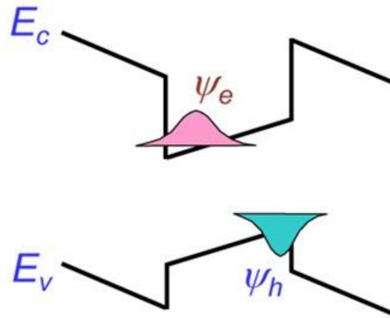


*Figure 1.7: Band diagram of a conventional III-nitride quantum well in equilibrium [20].*

### 1.4.3 Polarization-Induced Doping

While an abrupt heterointerface manifests as a 2D sheet of a carrier gas, a layer with a graded composition can create a mobile 3D carrier gas [21], as shown in Fig. 1.8. The polarization charge is obtained from the gradient of the polarization field vector, so by varying the grading

different concentrations of carriers can be generated – for example a linear grading would result in a uniform carrier concentration.

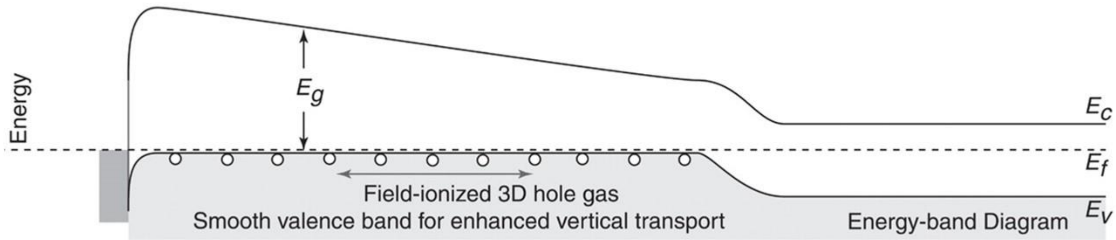


*Figure 1.8: Band-diagram of a compositionally graded AlGaN layer on GaN [21].*

This technique provides a powerful tool for the doping of wide bandgap semiconductors, where impurity doping may be challenging. It enables high carrier concentrations without degrading mobility by impurity doping, and the generated carriers do not have an activation energy like dopants, so they are able to conduct even at cryogenic temperatures.

### *1.4.4 Polarization-Engineered Tunnel Junctions*

GaN-based tunnel junctions have been previously demonstrated and they have been also incorporated in LEDs [22, 23]. However, these homojunctions require extremely high doping for both the p-type and n-type layers to facilitate interband tunneling, and this proves challenging for wide bandgap alloys. A technique around this is the polarization engineered tunnel junction [24-27], shown in Fig. 1.9, which utilizes the heterointerface polarization charges generated to achieve tunneling despite the poor doping and large bandgap of the materials. These tunnel junctions are essentially double heterostructures, where the polarization charges generate a huge electric field

and band-bending in the intermediate layer. The sheet charges compensate for the ionized impurity charges in the depletion region, effectively narrowing the depletion region width.

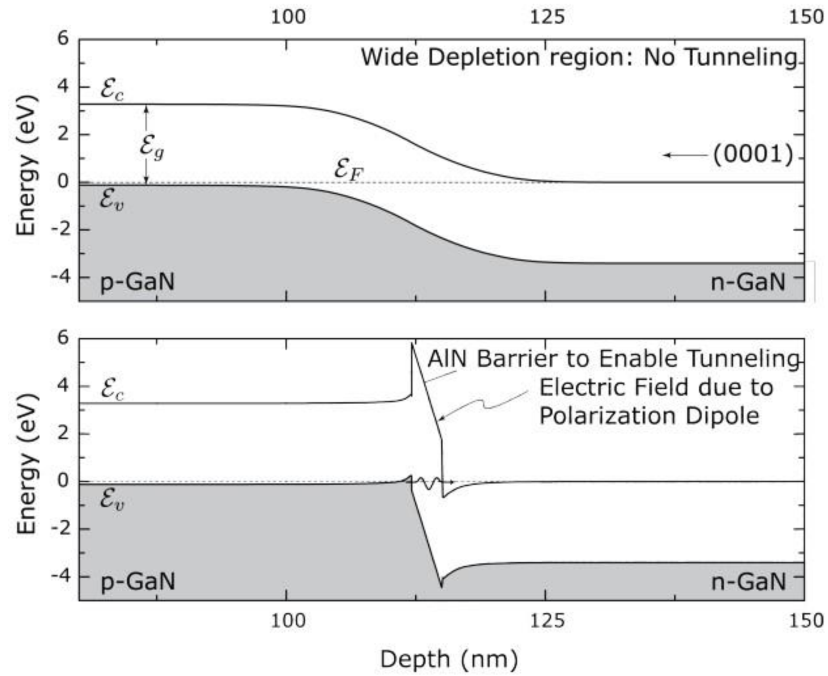


*Figure 1.9: Energy band diagram of a p-n junction (top) and a polarization-engineered tunnel junction (bottom) [26].*

### 1.5 Current State of III-Nitride Optoelectronic Devices

GaN has been intensively studied for several decades due to its promising properties for electrical and optical devices [28-30]. Initially, the focus was on visible light devices consisting of an InGaN active region. Such was the demand for these devices that for the invention of high-brightness blue InGaN LEDs, Nakamura et al received the Nobel Prize in Physics in 2014 [31]. This breakthrough was a direct consequence of advances in the p-type doping of the III-nitride materials [32, 33]. Soon after their emergence, GaN-based LEDs were rapidly commercialized, and they have now largely replaced fluorescent bulbs and other similar light sources for lighting.

Apart from LEDs, other devices such as laser diodes (LDs) have also been demonstrated utilizing InGaN.

Despite the advances in InGaN visible light sources, III-nitride devices emitting in the UV range have lagged. Due to the larger bandgaps required, these devices are commonly made utilizing AlGaN. While the wall-plug efficiency of blue LEDs can cross 80% [34], to date the efficiency of UV LEDs with emission below 265 nm is less than 10%. It has also remained challenging to achieve electrically pumped laser diodes in this wavelength range. Recently, AlGaN quantum well based laser diodes were demonstrated with emission below 300 nm [35, 36]. However, these devices can only operate in pulsed mode with extremely high threshold current and very low output power. Nevertheless, these developments show the great potential for realizing efficient AlGaN UV LEDs and lasers as household solid-state UV devices.

## 1.6 Challenges Facing AlGaN LEDs

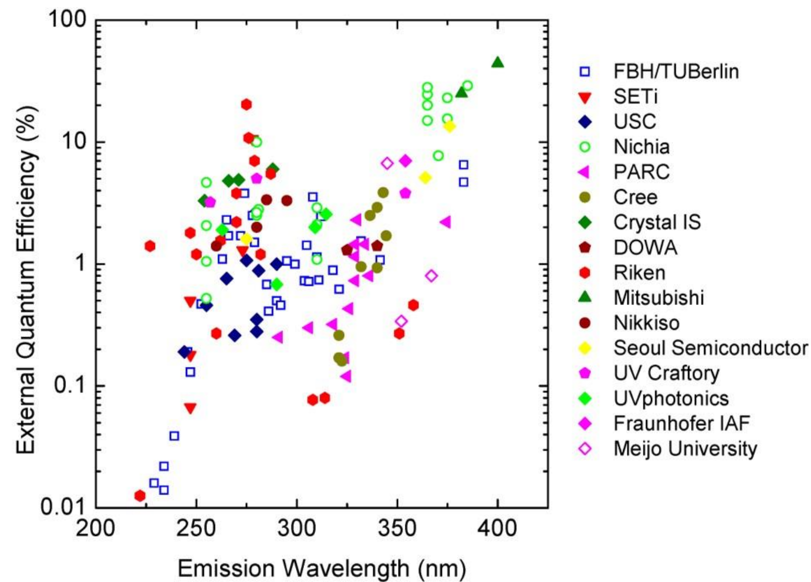


*Figure 1.10: Plot of EQE of UV LEDs vs. emission wavelengths. (Source [37])*

Figure 1.10 shows a plot of the EQE of AlGaN UV LEDs versus their emission wavelengths [37]. While tremendous efforts have been made in the past, the peak EQE measured for a diode emitting at 275 nm is still only around 20% [38]. This value falls sharply at even shorter emission wavelengths, with values less than 1% for emission below 250 nm. The corresponding WPE of the UV devices is even lower, which is a far way off the benchmark WPE of ~30-40% measured for conventional sources. There are several causes for the low efficiency of these devices and unless they are all tackled, they will compromise device performance.

### *1.6.1 Role of Threading Dislocations on IQE*

The low internal quantum efficiency is primarily a result of the huge density of threading dislocations that are present on the epitaxial layers when grown on substrates having a lattice mismatch (such as sapphire or silicon) [39, 40]. Furthermore, GaN cannot be utilized as a buffer or contact layer as the AlGaN alloy would be under tensile strain, which might form cracks on the surface [41]. The threading dislocations provide pathways for carrier leakage and sites for the non-radiative recombination of carriers, lowering the device efficiency. Figure 1.11 plots the peak IQE possible for different dislocation densities at several emission wavelengths in the UV. Typically for AlN layers grown on sapphire, the dislocation density is of the order of $10^8 – 10^9$ $cm^{-2}$ for high-quality layers, which already restricts the efficiency to <70%. While the density of these defects can be significantly reduced when the growth is performed on single crystalline AlN substrates, these substrates remain prohibitively expensive for most commercial applications.

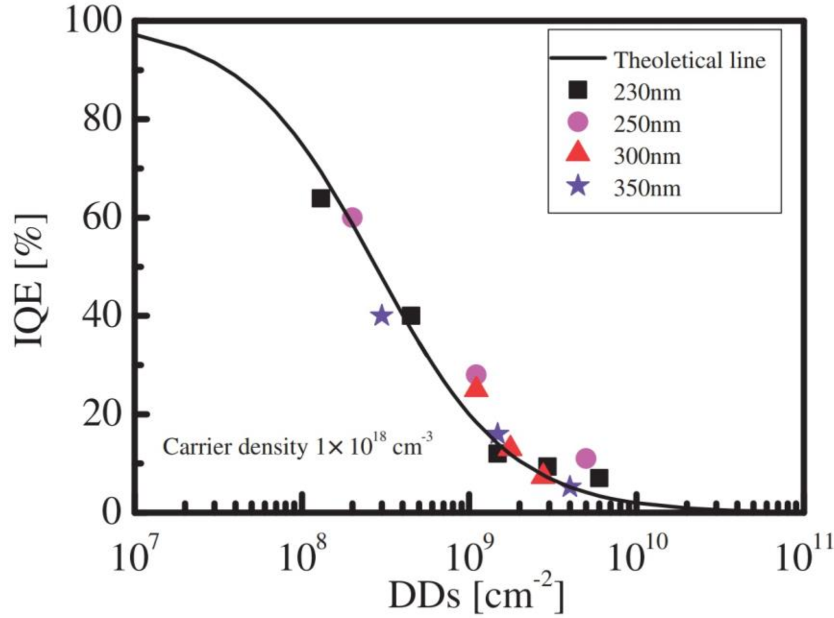


*Figure 1.11: Variation of maximum IQE for different dislocation densities at different wavelengths. (Source: [42])*

### *1.6.2 Low Extraction of TM-polarized Light*

The emission from optical devices may be polarized either transverse-electric (TE) or transverse-magnetic (TM). As TE-polarized light is emitted in the out-of-plane direction it can be readily extracted for surface or backside emitting devices. However, TM-polarized emission is emitted in-plane, which is relatively harder to extract. A schematic of the emission is shown in Fig. 1.12(a). In AlGaN, the valence band maximum is split into three sub-bands, the heavy hole (HH), light hole (LH) and the crystal-field split-off hole (CH) bands [41]. For a low Al content, the HH and LH hole bands are above the CH band, and the resultant emission from carrier recombination is mostly TE-polarized. As the Al content for the alloy increases, the CH moves up, while the HH and LH bands shift downward, until there is a crossover at ~60% Al content [43]. For higher Al compositions (shorter wavelengths), carrier recombination primarily occurs in the CH band, from which the photons generated are mostly TM-polarized. A schematic of the

bandstructure for such high Al composition AlGaN is shown in Fig. 1.12(b). The predominantly TM-polarized emission from deep UV LEDs incorporating such an AlGaN active region results in light extraction efficiency <10% [44], shown in Fig. 1.12(c).

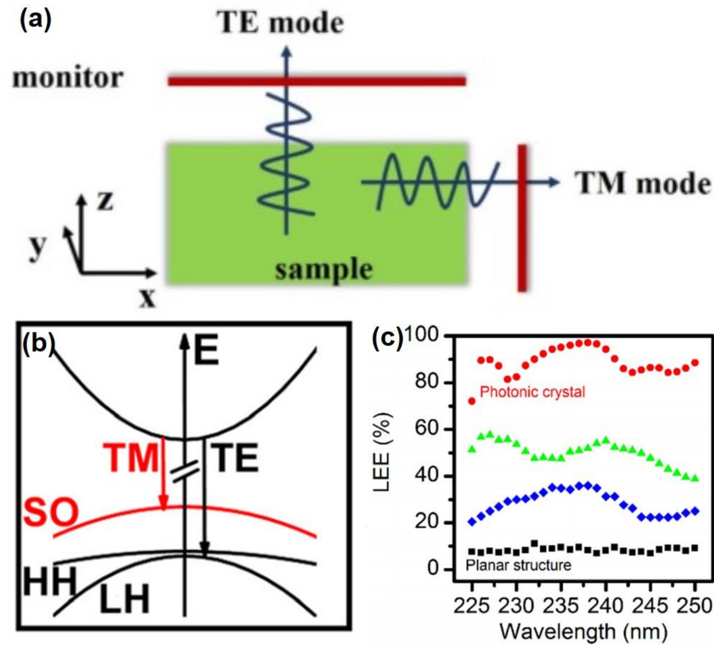


*Figure 1.12: (a) Schematic of extraction of light for TE and TM polarized emission [45]. (b) Band structure for AlGaN with a high Al composition [46]. (c) Comparison of LEE for a planar structure and different configurations of photonic crystal structures [44].*

Apart from the difficulty of extracting the light, the high energy photons emitted from UV devices can also be absorbed by the substrate if its bandgap is small enough. Therefore, if absorptive substrates such as GaN or Si are used then substrate removal would be essential to maximize efficiency.

### *1.6.3 Poor p-type Doping*

Another major challenge standing in the way of high efficiency AlGaN devices is the injection of charge carriers, especially for devices operating at shorter wavelengths, where the Al content required for the structure is higher. This is primarily due to the difficulty in the p-type doping of these wide bandgap alloys. Magnesium has been established as the most viable p-type dopant for III-nitrides, however the doping efficiency is very poor for AlGaN due to the high activation energy for the Mg acceptor, which can reach up to 600 meV for AlN [47]. The activation energies of Mg for different Al compositions are shown in Fig. 1.13(a). Therefore, to realize low resistivity p-type conduction in AlGaN films, it is essential to incorporate enough Mg atoms so as to form an impurity band for the hole transport [48, 49]. However, the formation energy for the substitutional incorporation of Mg atoms into the crystal lattice increases as the Fermi level moves closer to the valence band and when the Al content of the alloy increases, adversely impacting the doping of the layers. This is shown in Fig. 1.13(b). From a growth perspective, the excessive incorporation of Mg can degrade the crystal quality, and contribute to the formation of compensating defects, nullifying the expected increase in hole concentration. The resistance of devices is also quite high as low hole concentration makes it difficult to obtain a good ohmic contact directly to p-doped AlGaN.

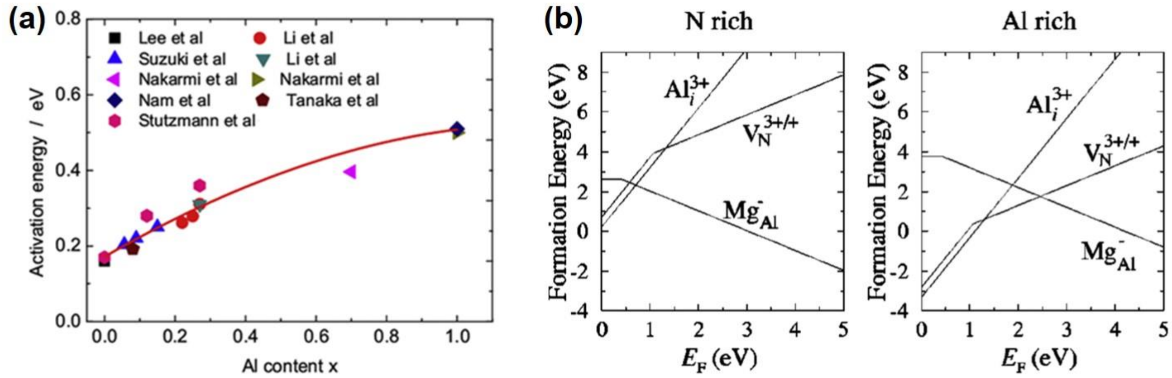


*Figure 1.13: (a) Activation energy of Mg acceptor dopant for different Al composition AlGaN [50]. (b) Formation energy of Mg substitutional incorporation in AlN under N-rich and metal-rich growth regimes [51].*

### *1.6.4 Carrier Overflow from Active Region*

Despite the difficulties facing the efficient p-type doping of AlGaN, on the other hand, relatively high n-type doping, using Si as a dopant, can be readily obtained in n-type AlGaN films even with high Al composition [52]. The electron mobility is also significantly greater than the hole mobility [53, 54]. Therefore, there is a highly imbalanced electron and hole injection, leading to significant electron overflow in the device active region and poor carrier injection efficiency under moderate current injection conditions [55]. Such an issue becomes more severe for AlGaN LEDs operating at shorter wavelengths, due to the further reduced free hole concentration.

## 1.7 Recent Developments in AlGaN UV LED Technology

### *1.7.1 Improvement of Material Quality*

Typically, AlGaN UV LEDs are grown on sapphire substrates. Before the growth of the device layers AlN is commonly used as a buffer layer. The lattice mismatch between AlN and sapphire results in the formation of threading dislocations that play a critical role on IQE, as had

been discussed above. Several techniques have been investigated including the growth of interlayers [56], $NH_3$ pulsed flow technique in metal-organic chemical vapor deposition (MOCVD) [57], migration enhanced epitaxy [58] and growth on nano-patterned substrates (NPSS) [59], which also improves the light extraction as is schematically shown in Fig. 1.14(a). Epitaxial lateral overgrowth (ELO) [60, 61] involves the regrowth of material on patterned substrates, and an example is shown in Fig. 1.14(b). These techniques have helped to reduce the dislocation density in the AlN layers to the $10^7$ $cm^{-2}$ order. Furthermore, bulk AlN crystals have been grown by hydride vapor phase epitaxy (HVPE) [62], and they are commercially available, although the substrates are extremely expensive and they often have deep-level defects that absorb UV light [63], rendering them impractical for devices. An AlN single crystal wafer from Hexatech, Inc is shown in Fig. 1.14(c), and it is seen to be a yellow-orange color as a result of UV-absorbing defects.

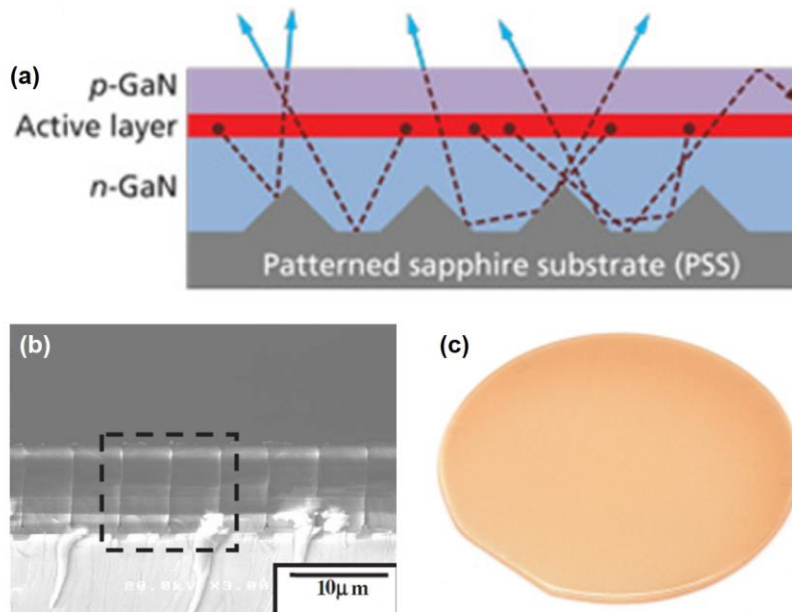


*Figure 1.14:(a) Schematic of a growth on a patterned sapphire substrate [64]. (b) Cross-sectional SEM image of AlN wafer grown using epitaxial lateral overgrowth [65]. (c) Image of an AlN single crystal substrate produced by Hexatech, Inc. [66].*

Compared to other growth methods, MBE is more versatile as it enables growth of the epilayer under conditions of excess metal on the surface. When AlGaN films are grown under such conditions, they form Ga clusters within the epilayers that can provide sites where localized carriers can recombine radiatively [67-70]. The presence of these clusters has a distinct effect on the emission properties of these layers, enabling extremely high IQE, even on substrates with a high dislocation density.

Recently, high temperature annealing of AlN layers has attracted significant attention as a low-cost and relatively simple method of obtaining high-quality material. MBE growth of AlN films, followed by high-temperature annealing has been shown to dramatically improve material quality, even for very thin AlN layers [71]. The sputtering of Al(Ga)N films, followed by annealing can also provide substrates with dislocation densities comparable to films grown epitaxially [72, 73]. UV LEDs have also been demonstrated on these sputtered films [74].

### *1.7.2 Approaches for Enhanced Light Extraction*

Several techniques have been developed in the process flow for device fabrication to improve the low light extraction of UV LEDs. Growth on patterned sapphire substrates, which can improve material quality, also improves light extraction by reducing the total internal reflection of generated light [75]. By encapsulating LED dies [76, 77], as shown in Fig. 1.15(a), the light extraction from the device can be increased, while simultaneously alleviating heating issues. Work has also been done on the removal of substrates for growth of III-nitrides, which can substantially increase the extracted light for III-nitride LEDs [78-80]. The removed epitaxial film, schematically

shown in Fig. 1.15(b), can be transferred onto reflective and thermally conductive substrates to further improve performance. Photonic crystals also promise alternative routes to improve LEE, and their ability to guide light modes can be utilized for the development of lasers [44, 67, 81-86]. These photonic crystals can be either etched down as shown in Fig. 1.15(c), or they can be grown bottom-up using selective area growth, as shown in Fig. 1.15(d). Reflective contacts have also been used in bottom-emitting UV LEDs to reduce collection losses [38]. However, even if these techniques are implemented, unless the absorbing contact layers commonly used in UV LEDs are removed, their efficacy will be limited.

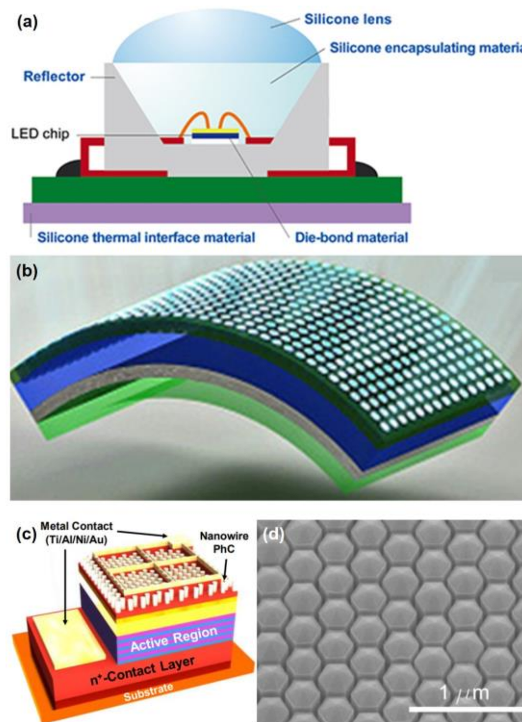


*Figure 1.15:(a) Schematic of an LED die with encapsulation [87]. (b) Schematic of an LED that has had its substrate removed [88]. (c) Schematic of an LED with a photonic crystal etched into the top contact layer [82]. (d) SEM image of a selective-area growth nanowire photonic crystal [83].*

### *1.7.3 Advances in p-type Doping*

GaN is commonly used as the p-type contact layer for UV LEDs, as it can provide a good contact for hole injection. However, due to its comparatively smaller bandgap, it absorbs light in the UV range. Therefore, it is critical to replace this layer with a transparent p-doped AlGaN contact layer.

Extensive work has been done to realize low-resistivity p-AlGaN including using a high nitrogen overpressure during growth [48], delta-doping [89], utilizing superlattices [90, 91], using In surfactant [91], metal-modulation epitaxy [92], and polarization-induced doping [21, 93]. In this thesis, we present the use of metal-semiconductor junction assisted epitaxy [94] using MBE, which demonstrates record low resistivities even for AlGaN alloys with a high Al composition.

### *1.7.4 New Heterostructure Designs*

The imbalance between the electron and hole injections into the active regions make it necessary to utilize an electron blocking layer (EBL) within the device. This layer serves to confine electrons to within the active region, preventing carrier overflow. However, for shorter wavelength devices the inclusion of this layer is not trivial as the AlGaN system approaches compositions close to AlN. Furthermore, this layer is often p-doped and placed after the active region, where the band offset in the valence band between the EBL and the active region can further impede hole injection to the active region. Alternative techniques of using the EBL such as the growth of a superlattice have been demonstrated to improve efficiency [95-97]. In this thesis, we investigated the effect of the EBL on device performance for a 280 nm LED, and we show that for AlGaN devices an n-doped EBL placed immediately before the active region is more effective at

improving device performance [98]. Such a design would decrease electron injection to the active region, while maintaining the hole injection, thereby attaining a more equitable injection of carriers.

The use of tunnel junctions as p-type contact layers has garnered attention due to its ability to solve several problems associated with the p-type contact [99-102]. As the n-type doping of AlGaN is relatively easier than p-type doping, highly conductive AlGaN layers that are transparent to the emitted light can be utilized for the contacts. This would help to improve contact resistivity, improve current spreading, and allow the use of lower resistivity reflective contacts. Tunneling across an AlGaN homojunction is difficult due to the wide bandgap of the materials and the difficulty in achieving high hole concentration, so polarization-engineering is commonly utilized to significantly lower the barrier height for the tunneling of carriers [25]. In this thesis, we have utilized the tunnel junction design to demonstrate high efficiency tunnel junction UV LEDs emitting at 265 nm and 255 nm [103, 104].

### *1.7.5 AlGaN-based Nanostructures*

Nanostructures are an important future direction for AlGaN-based devices, as they promise high IQE due to the nearly perfect crystalline structure [105, 106], improved doping efficiency [107, 108] and a high surface-to-volume ratio enabling enhanced LEE [109]. AlGaN nanowires have been demonstrated with emission across the entire compositional range. These nanostructures also typically grow with a core-shell structure, where the higher Al composition layer forms the shell [67, 83, 110]. This layer can suppress non-radiative surface recombination in devices, improving IQE. A cross-sectional TEM image of a nanowire is shown in Fig. 1.16(a) and Fig.

1.16(b) displays an elemental map of the marked region. Selective-area growth (SAG) of nanowire arrays has also been demonstrated [83], which enables the bottom-up formation of photonic crystal arrays that can allow for improved extraction of light, like in Fig. 1.16(c), or for guiding the modes of a laser [44, 111]. Nanostructures can also be grown on different substrates, which allows for the possibility of integrating such devices on flexible or novel substrates [112, 113].

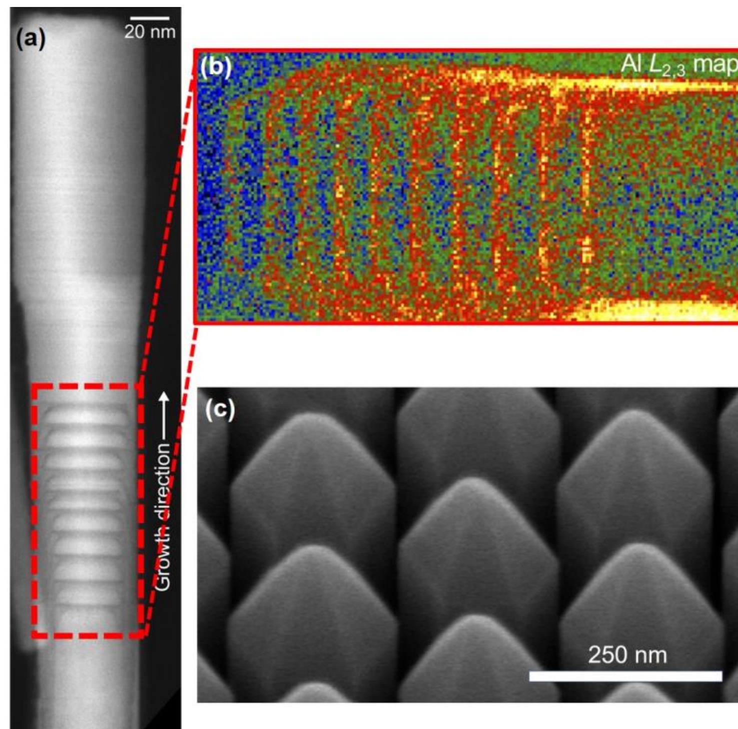


*Figure 1.16:(a) Cross-sectional TEM image of a spontaneously grown nanowire [114]. (b) Elemental mapping of the marked region from Fig. 1.16(a). (c) SEM image of an SAG nanowire photonic crystal.*

## 1.8 Dissertation Overview

The primary objective of this dissertation is to understand and develop the techniques required to grow and fabricate high efficiency AlGaN mid and deep UV LEDs.

Chapter 2 describes the molecular beam epitaxial growth of the semiconductor structures in this work. An overview of the growth technique utilized is presented along with descriptions of commonly used characterization methods.

Chapter 3 presents the work published in [94], where we utilize the unique growth environment of the MBE system to implement the metal-semiconductor junction assisted growth technique. This growth method was used for the growth of p-doped AlGaN epilayers with extremely low resistivity <10 Ω·cm even for an Al composition ~90%. The measured resistivities were orders of magnitude lower than previously reported alloys with a similar Al composition. UV LEDs with emission at 280 nm fabricated using this technique showed a great improvement in external quantum efficiency, and lower turn-on voltage, as compared to devices grown using conventional epitaxy.

Chapter 4 is a report on the investigation of the effect of the electron blocking layer on device performance, published in [98]. Different types and thicknesses of EBLs were compared to study their effect on the performance of a 280 nm LED. An improvement in device efficiency is observed for an n-type EBL placed before the active region, which can hamper hole injection to the active region, while not impeding hole injection, thereby resulting in more balanced carrier injection.

Chapter 5 is a report on the demonstration of a high-efficiency tunnel junction LED with emission at 265 nm [104]. Different polarization-engineered tunnel junction designs were investigated to study their effect on device performance. For the optimum tunnel junction design with a 5 nm thick GaN layer sandwiched between highly doped n-type and p-type AlGaN layers, a maximum EQE of 11% was measured, with a corresponding WPE of 7.6%.

Chapter 6 presents a study on the electrical and optical emission properties of an AlGaN tunnel-junction UV LED with emission at 255 nm [103]. The device operated with a maximum EQE of 7.2% and WPE of 4%, with highly stable emission. This efficiency is two orders of magnitude greater than previously reported tunnel junction UV LEDs at this short wavelength. Temperature-dependent measurements were also performed to further study the device properties.

Chapter 7 describes the work on the further extension of tunnel junction UV LEDs to even shorter emission wavelengths. A double-heterostructure design is implemented for emission at 245 nm. Different designs of the heterostructure were fabricated and measured, which along with optical studies of the device active region, were used to examine the critical role of electron overflow on the device efficiency.

Finally, chapter 8 presents some future directions towards further improvement of AlGaN LEDs and for short-wavelength UV laser diodes. This includes the utilization of tunnel-junction structures for maximizing current injection in UV laser structures, the use of nanostructures to improve device performance, with a special emphasis on N-polar nanostructures, as well as incorporating methods to lift-off the grown layers which can aid substrate removal.

# Chapter 2. Methods

## 2.1 Overview

This section provides an overview of the molecular beam epitaxy system and the epitaxial techniques used in this thesis. The principles behind the different characterization techniques used for evaluating the grown layers and subsequently fabricated devices are also detailed.

## 2.2 Molecular Beam Epitaxy

Molecular beam epitaxy has been well established as a method for the epitaxial growth of III-V compounds and novel materials [115-120]. In an MBE, crystal growth takes place under conditions of ultra-high vacuum (~$10^{-12}$ Torr). To establish such a low background pressure, several pumps including cryo pumps and ion pumps are used to reduce the pressure of the growth chamber. The panels of the system are also cooled using a constant stream of liquid nitrogen, which helps to collect impurities on the walls of the chamber.

These systems contain several different elements contained in sources that all point towards a substrate, mounted on a heater. During epitaxy, these sources are heated to slowly evaporate material which emerges as a beam from the sources. The ultra-high vacuum environment enables extremely long mean free paths for the evaporated atoms, so that they only react when the elemental beams converge on the substrate [121]. The MBE used in this work was a Veeco Gen 930 MBE system, pictured in Fig. 2.1. The system is equipped with two cells containing Ga, two

cells containing Al, one In cell, one Mg cell and one Si dopant cell. It should also be noted that elemental nitrogen is produced by striking a plasma, using a radio-frequency (RF) assisted plasma source, through a high purity nitrogen gas flow.

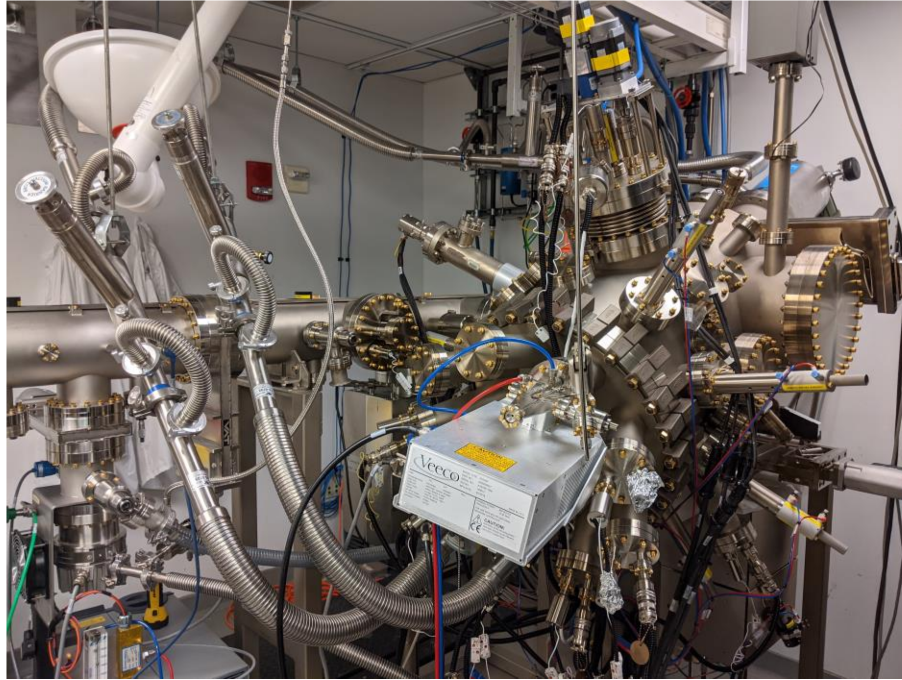


*Figure 2.1: An image of the Veeco Gen930 MBE system used in this work.*

To determine the amount of material being evaporated for a given source temperature, a beam flux monitor (BFM) is used in MBE. Calibration of the source fluxes using the BFM is crucial for ensuring the repeatability and control of grown structures.

Reflection high-energy electron diffraction (RHEED) is a powerful tool available in the used MBE system, that can provide real-time *in-situ* feedback of the grown layer. The RHEED system consists of an electron gun aimed at a very shallow angle to the substrate, and a phosphor screen. During operation, the electron gun shoots electrons towards the substrate, where they glance off

and present a pattern on the phosphor screen, schematically shown in Fig. 2.2. The shallow angle that the gun is aimed at ensures that the electrons are diffracted by only the first few monolayers present at the sample surface [122]. The observed patterns indicate the surface morphology and crystallinity of the grown films. For certain crystalline samples, reconstructions can appear on the surface providing an indicator of the growth conditions.

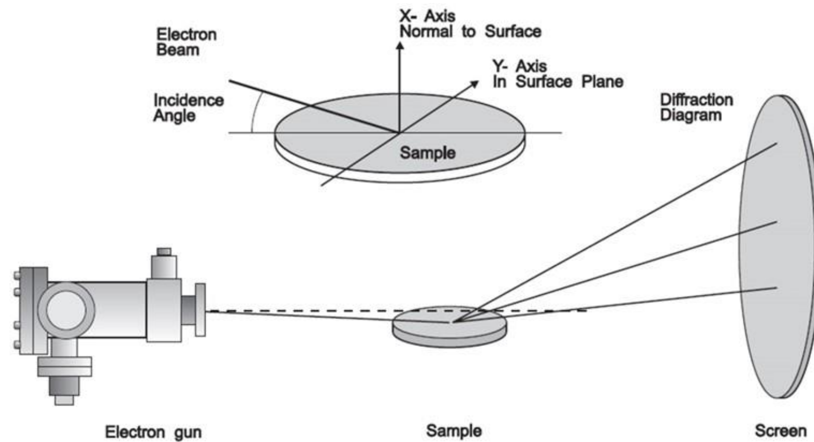


*Figure 2.2: Schematic of RHEED operation [123].*

The MBE system used was also equipped with a pyrometer, used for calibrating the substrate growth temperature across different samples, along with the substrate heater thermocouple.

### *2.2.1 Epitaxial Growth*

Epitaxial growth using MBE is unique as it is a physical deposition method, where the morphology, composition and structure of the grown layer are dependent on the surface kinetics of adatoms and the thermodynamics of crystal formation [124-126]. The combination of these factors results in three main growth modes: Volmer-Weber (VW) [127], Stranski-Krastanow (SK)

[128] and Frank van der Merwe (FM) [129]. A schematic of the three growth modes is shown in Figure 2.1.

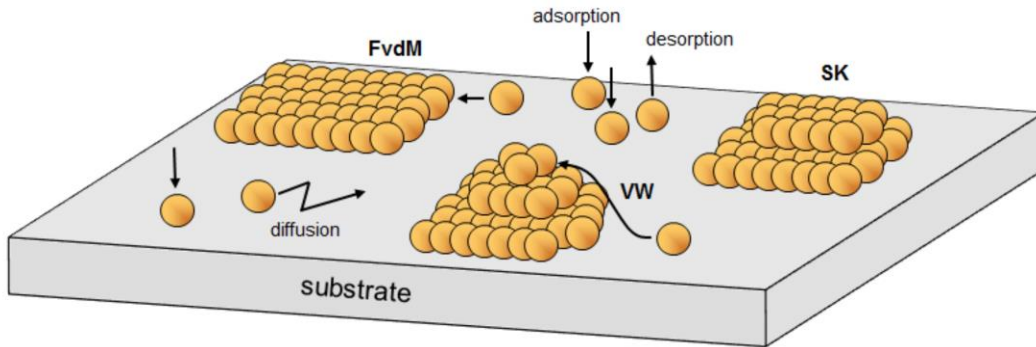


*Figure 2.3: Schematic representation of the film growth modes. (Source: [130] )*

In the VW growth mode, the interaction between the impinging adatoms is stronger among themselves than with the substrate, resulting in the clustering of the grown material. These clusters form islands, and in certain conditions (such as under N-rich conditions and high temperature for GaN) they can also form nanowires [131, 132]. This growth mode is commonly seen when there is a large lattice mismatch between the substrate and the grown material. The SK growth mode is an intermediate 2D-3D growth mode, where initially a wetting layer is grown in a layer-by-layer manner, however beyond a certain critical thickness that is strongly dependent on the strain of the grown layer, a transition to a 3D growth mode occurs. This growth mode has been utilized for the growth of InGaN and GaN quantum dots [133-139]. FM growth is the ideal layer-by-layer growth mode, observed in homoepitaxial and high-quality layers. This growth mode is preferred for epilayers, and the films grown using this method have very low surface roughness.

### *2.2.2 Advantages of MBE*

Plasma-assisted MBE has the advantage of being a physical process, relying on impinging nitrogen active species to react with the elements provided from the substrate, which allows the flux of nitrogen to the substrate to be precisely controlled through the flow of nitrogen and the plasma power applied. This in contrast to methods like ammonia-based MBE which rely on the cracking of ammonia molecules on the substrate surface to generate nitrogen. The cracking of ammonia is strongly dependent on substrate temperature, and its efficiency is also very low even at elevated temperatures. Also, unlike methods like MOCVD and HVPE that utilize a high nitrogen overpressure, in MBE it is possible to perform epitaxy under conditions of excess metal, which is a completely unique growth regime.

For III-nitride devices, MBE has a huge advantage over MOCVD in the growth of p-doped layers, as there is no need to anneal the doped layers after its growth. MOCVD requires the annealing of p-doped layers to diffuse hydrogen out, so as to activate them, however the absence of hydrogen in MBE negates the need for this process. The lower growth temperatures in PA-MBE systems can also promote the incorporation of Mg dopants.

Apart from these advantages, in general MBE has a very low impurity concentration due to the ultra-high vacuum environment. The lower growth rates of MBE compared to other methods and the use of shutters to block the supply of material flux allow for the sub-monolayer precision in controlling the thicknesses of layers. Nitride-based MBE systems also do not contain any toxic or hazardous materials, unlike the extremely toxic precursors used in MOCVD.

### *2.2.3 Challenges with MBE*

Typically, the lower growth temperatures in MBE-grown materials results in a higher density of point defects in grown layers. The presence of these point defects has been correlated with the lower efficiency of MBE-grown devices as compared to MOCVD-grown devices [140, 141]. To overcome this problem, new high-temperature MBE systems have been developed, enabling material growth, as well as annealing at temperatures up to 1800 ˚C. Utilizing one such system, the Veeco GenXplor, my colleague Dr. David Laleyan had demonstrated thin, smooth, high-quality AlN layers grown directly on a sapphire substrate through a multi-cycle anneal-regrowth process [71].

The growth rates of materials are typically much lower in an MBE system, as compared to an MOCVD system, so it is comparatively more difficult to grow thick buffer layers. Recently, with the use of modified and improved sources, relatively high growth rates have also been demonstrated using MBE [142], which are comparable or even higher than MOCVD.

### *2.2.4 MBE Growth of AlGaN*

Prior to epitaxy, the substrates used must follow a rigorous cleaning procedure to minimize contamination to the chamber, and to maximizing the yield and performance of devices. This procedure is outlined in Appendix A. For the epilayers in this work, we utilized conditions where there was an excess of metal flux as compared to the incoming active nitrogen species. This resulted in an accumulation of metal on the sample surface during epitaxy. To confirm this, we observed a dimming in the RHEED pattern during the growth of the AlGaN epilayers. This growth

regime ensures good layer-by-layer growth with a smooth surface morphology, as could be observed with a streaky RHEED pattern.

As the growth of the epilayers took place under slightly metal-rich conditions, this means that the impinging metal flux was greater than the supplied nitrogen species. Due to the stronger bond between Al and N, AlN is preferentially formed on the sample surface, and the remaining nitrogen reacts with the gallium present on the surface. Excess gallium accumulates on the surface forming a metal layer. Therefore, under this growth regime, the growth rate is limited by nitrogen, while the composition of the alloy depends on the ratio of Al to N [69, 70, 115, 143, 144]. By controlling these parameters, while ensuring that the gallium flux is enough to accumulate metal on the growth front, we could vary the composition and emission wavelength of the grown layers. However, prolonged growth in this regime can result in the formation of gallium droplets, as shown in Fig. 2.4(a), as well as crystalline defects underneath them, like in Fig. 2.4(b), so the Ga metal layer was periodically desorbed during the growth. This was done through an annealing process, where the source shutters were closed, and the substrate temperature was increased by 50 ˚C. The RHEED was then monitored to see the transformation from a dim, streaky RHEED pattern to a bright, streaky pattern, which indicated that there was no excess metal present on the growth surface. The substrate temperature was then ramped down, and the growth resumed.

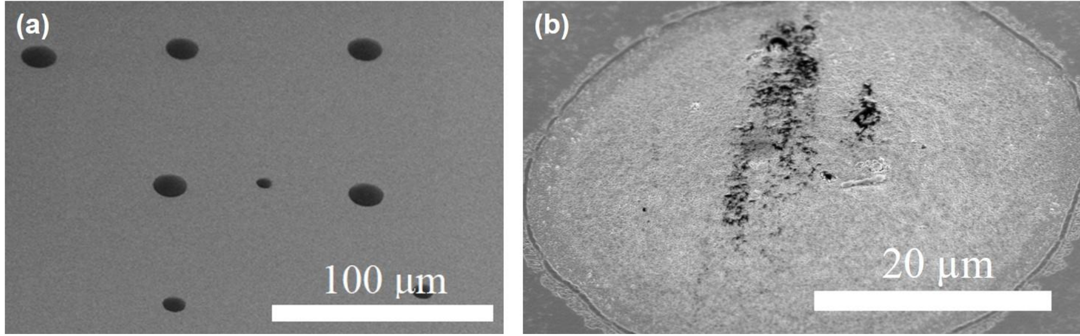


*Figure 2.4:(a) SEM image of Ga droplets on the surface of AlGaN immediately after growth. (b) Crystalline defect formed at Ga droplet.*

During epitaxy, the growth temperature is a critical parameter that affects dopant incorporation, substrate morphology, adatom kinetics and the growth rate [145]. In this work, the substrate temperature was set to 680-700 ˚C (calibrated to the pyrometer). The thermocouple temperature used for pyrometer temperature varied from ~650-750 ˚C, with the wide variation a result of changes in the MBE system, as well as variations between different sample wafers. At higher temperatures, the Ga flux required to maintain a metal-rich growth regime was too high, while lower temperatures had worse optical quality.

Two separate Al cells were used in the growth of the AlGaN layers to provide Al metal flux. This was done so as to enable the rapid opening and closing of the cell shutters for obtaining sharp hetero-interfaces between AlGaN layers of different compositions, while avoiding any interruptions during the growth.

## 2.3 Optical Material Characterization Techniques

### *2.3.1 Photoluminescence Spectroscopy*

Photoluminescence (PL) spectroscopy is commonly used to determine the emission wavelength and composition of semiconductor samples [5]. The process works by photoexcitation of the sample with a light source having a photon energy greater than the bandgap of the material. This results in the generation of charge carriers in the sample, and the light emitted from the radiative recombination of these carriers is collected and analyzed using a spectrometer. A schematic of this process for a typical direct bandgap semiconductor is shown in Fig. 2.5.

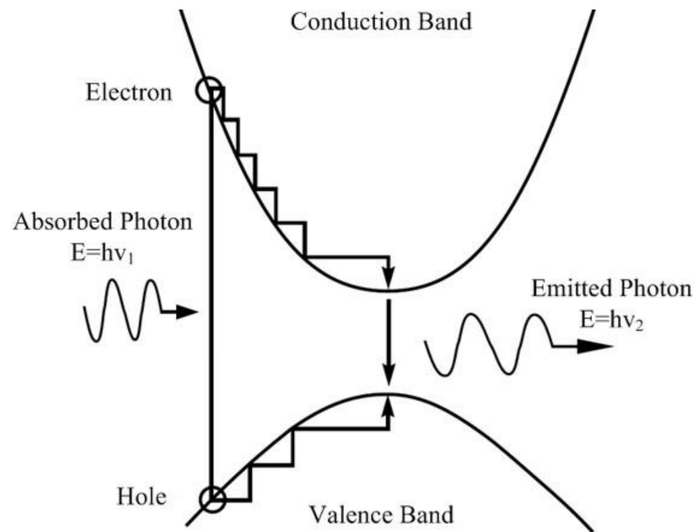


*Figure 2.5: Schematic of the photoexcitation process in a semiconductor [146].*

As the AlGaN alloys are wide bandgap materials, a Coherent Excistar XS500 ArF excimer laser was used, having emission at 193 nm, for exciting the samples and a UV-sensitive charge coupled detector (CCD) was used to measure their photoluminescence spectra. We also used a neutral density filter to adjust laser power and measure spectra at different excitation powers. While PL spectroscopy is a useful method to determine the emission wavelength of the grown

layers, it was not very helpful in determining composition, as the growth regime used in this work results in large potential fluctuations, which can cause the emission peak to be considerably different than the expected bandgap of the material [68].

### *2.3.2 Time-Resolved Photoluminescence Spectroscopy*

Time-resolved photoluminescence (TRPL) spectroscopy can provide information on the recombination of charge carriers created by photoexcitation. For the measurements in this work, we used a frequency-tripled Ti:Sapphire laser, tuned to 736 nm with an 80 MHz repetition rate and 100 fs pulse width. The emission was collected and analyzed by a 0.75m monochromator, using a photomultiplier tube for detection. A schematic of the setup is shown in Fig. 2.6.

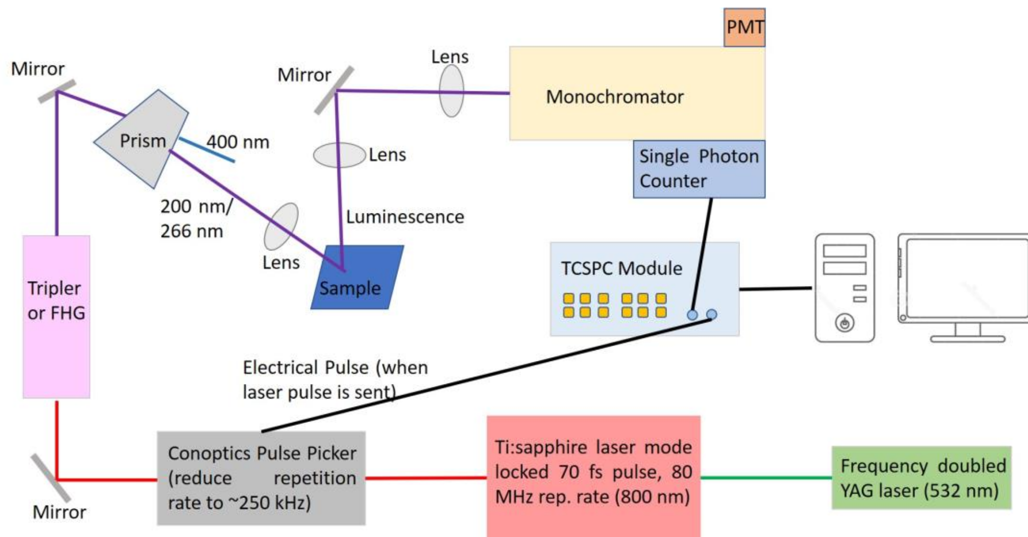


*Figure 2.6: Schematic of the TRPL setup.*

### *2.3.3 Spectroscopic Ellipsometry*

Spectroscopic ellipsometry of grown epilayers has been used to calibrate the growth rates of the materials. In this method, elliptically polarized light of different wavelengths is reflected off

the sample, and a detector is used to measure changes in the phase and amplitude of the individual polarizations [147]. A schematic of the setup is shown in Fig. 2.7. This data can then be used to calculate the refractive index and thickness of the layers by fitting it to a Cauchy model in a wavelength range where the material is transparent.

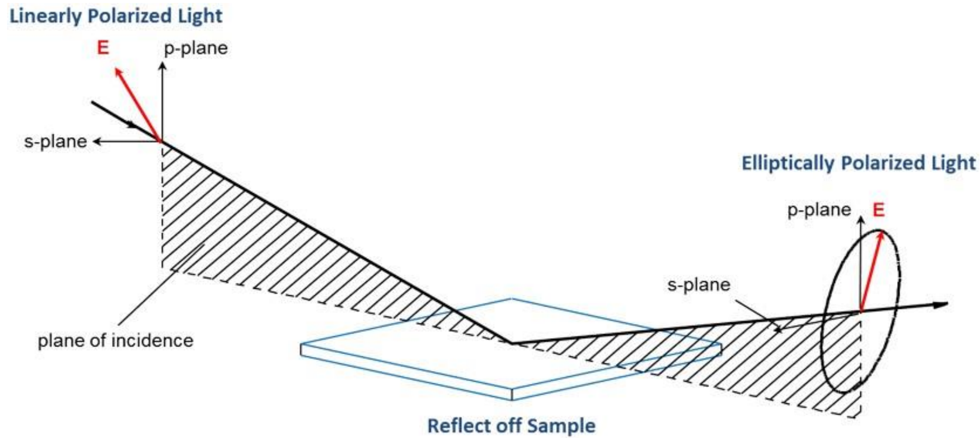


*Figure 2.7: Schematic of the ellipsometry technique [147].*

## 2.4 Structural Characterization Techniques

### *2.4.1 X-Ray Diffraction*

X-ray diffraction (XRD) is a powerful method for determining the material quality, lattice constants, strain and composition of layers grown using epitaxy. In XRD, the sample is hit with an incident X-ray beam having a fixed wavelength. The X-ray photons scatter in the crystal lattice, based on Bragg's Law, diffracting constructively and destructively for different incident and detection angles. This is shown in Fig. 2.8(a). The reflected photons are then collected at the detector. Depending on the angle of incidence, collection, and the substrate orientation, the intensity of the collected signal will vary, detailing information on the crystal.

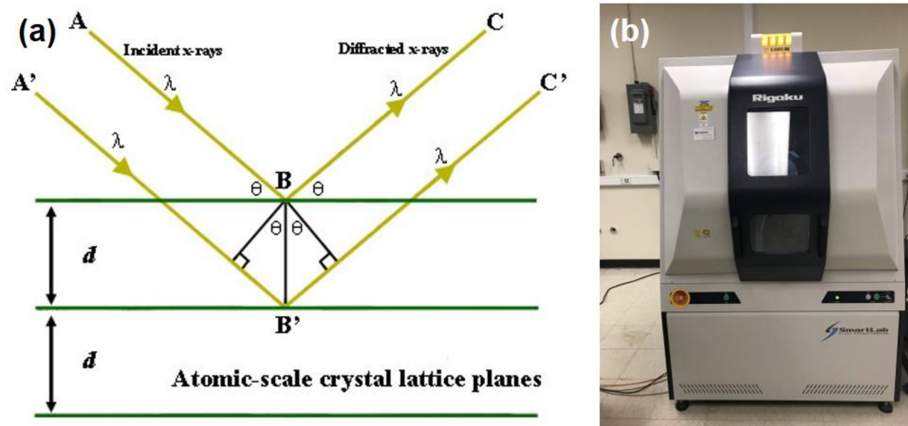


*Figure 2.8:(a) Schematic of the XRD experiment [148]. (b) A Rigaku SmartLab XRD system.*

This work used a Rigaku SmartLab XRD system, pictured in Fig. 2.8(b), for performing coupled 2θ-ω scans. These measurements can provide the lattice constant of the grown material, and then Vegard's law can be used for estimating the alloy composition.

### *2.4.2 Scanning Electron Microscopy*

Scanning electron microscopy (SEM) involves focusing a beam of high-energy electrons onto the surface of the sample, generating secondary electrons, backscattered electrons and X-rays, which are then collected. From these, information regarding the sample surface, composition and phase can be determined. SEM provides significantly better magnification than optical microscopes, and it allows for the resolution of features in the nanometer scale range.

### *2.4.3 Scanning Transmission Electron Microscopy*

Scanning transmission electron microscopy (STEM) has the capability of providing atomic level resolution of materials, even providing data on the distribution of elements, defect density

and crystal structure. In STEM, electrons with energy greater than 100 keV are transmitted through a thin cross-section of the sample under investigation. High-angle annular dark-field (HAADF) STEM collects incoherently scattered electrons, which can provide contrast that is sensitive to the atomic number of the elements composing the material. This is critical for investigating the heterojunctions studied. In this work, HAADF-STEM was performed on several samples by our collaborators Dr. Jiseok Gim and Prof. Robert Hovden in the Materials Science and Engineering department at the University of Michigan.

### *2.4.4 Atomic Force Microscopy*

Atomic force microscopy (AFM) can provide detailed information of sample surfaces. A small tip is attached to the end of a cantilever, which then oscillates close to the sample surface. The difference in the interaction of the tip with the sample surface can provide information on the height of features, phase, and surface roughness. In this work, a Bruker Icon AFM was used in tapping mode in air to map the surface and determine the surface roughness of the grown AlGaN layers.

### *2.4.5 Secondary Ion Mass Spectrometry*

Secondary ion mass spectrometry (SIMS) is a destructive technique which can be used to determine the composition and thickness of different layers. A primary ion beam sputters material from the surface of the sample, and the ejected secondary ions are collected using a mass spectrometer. In this work, SIMS was performed on certain samples by EAG Laboratories.

## 2.5 Electrical and Device Characterization Techniques

Details on the device fabrication can be found in Appendix B. This section describes the measurement techniques used to characterize the fabricated devices.

### *2.5.1 Hall Measurements*

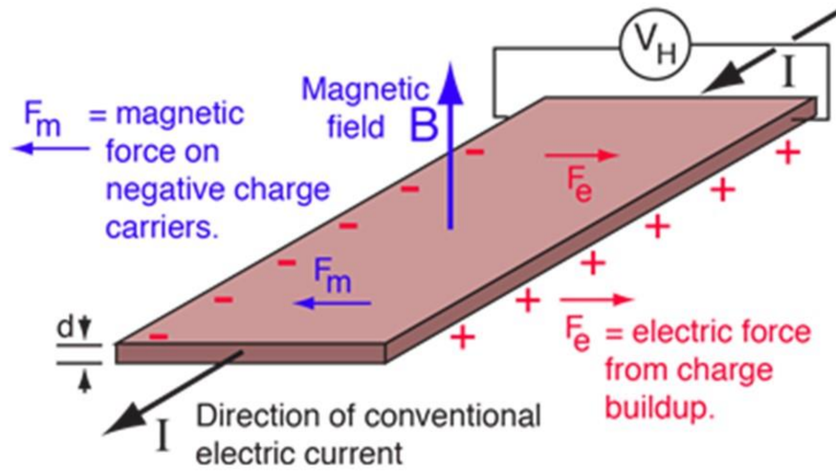


*Figure 2.9: Diagram of the Hall effect [149].*

Hall measurements using the van der Pauw configuration is a quick and efficient method of determining the free carrier concentrations in doped semiconductor layers. These methods rely on the Hall effect, where a current is injected through the sample, and a magnetic field is applied in a direction perpendicular to current. The magnetic field causes the carriers to be deflected to one side of the sample (perpendicular to both the magnetic field and the current), which results in an electric field, and a corresponding voltage (the Hall voltage). Figure 2.9 shows a diagram of the Hall effect in a semiconductor bar. The Hall voltage is given by Equation 2.1:

$$V_H = \frac{I_x B_z}{ent} \qquad \textit{(Equation 2.1)}$$

where, $V_H$ is the Hall voltage, $I_x$ is the injected current, $B_z$ is the magnetic field, $n$ is the carrier density, $t$ is the layer thickness and $e$ is the electronic charge. The charge of the carriers determines the polarity of the Hall voltage.

In this work, an Ecopia Hall Measurement System was used for determining the carrier concentrations in the grown layers. This system also has the capability of heating the substrate to 500 ˚C, allowing us to measure the carrier concentration over a wide range of temperature.

### *2.5.2 Current-Voltage Measurements*

As LEDs are essentially diode structures, their current-voltage (I-V) characteristics are an important parameter in studying the device physics and performance. For an ideal diode, we would see a sharp turn-on voltage close to the material bandgap, and there would be negligible reverse bias leakage. Tunnel junction diodes are also expected to show similar characteristics.

In this work, we used both pulsed and continuous-wave (CW) sources for measuring the current-voltage characteristics of devices. A Keithley 2400 SMU was used for CW measurements, while an AV-1010B pulse generator was used for generating short duration voltage pulses.

### *2.5.3 LED Power Measurements*

To determine device efficiency, it is critical to collect as much light as possible from the samples. Here, we used a Newport 818-ST-2 UV photodetector with a Newport 1919-R power

meter. The samples were placed directly on the detector, and then a bias was applied. The measured power was then recorded, along with the voltage and current, to determine device efficiency.

### *2.5.4 Electroluminescence Spectroscopy*

In electroluminescence (EL) spectroscopy, the device is first put under bias at a voltage where there is light being emitted. A UV-transmissive fiber optic cable is then used to collect the light, and it is analyzed through a UV-sensitive CCD. Through proper alignment of the collecting fiber, it is possible to measure the EL spectra over several orders of magnitude of injection current variations.

# Chapter 3. Enhanced Doping Efficiency of Ultrawide Bandgap Semiconductors by Metal-Semiconductor Junction Assisted Epitaxy

## 3.1 Author Contribution and Copyright Disclaimer

The contents of this chapter were published in Physical Review Materials in May 2019 [94], for which I retain the right to include it in this thesis/dissertation, provided it is not published commercially. The co-authors were Xianhe Liu, Zihao Deng, Walter Shin, David Laleyan, Kishwar Mashooq, Eric Reid, Emmanouil Kioupakis, Pallab Bhattacharya, and Zetian Mi from the University of Michigan. I designed, conducted and authored most of the work. X. L. and D. L. contributed to the growth process. W. S., K. M., and E. R. contributed to the sample characterization measurements. Z. D. and E. K. performed the simulations presented. The work was supervised by Z. M., who contributed to the design of the experiments with P. B. and E. K. as part of a collaboration. This work was supported by the National Science Foundation (Grant DMR-1807984) and from the University of Michigan, College of Engineering. This research used resources of the National Energy Research Scientific Computing Center (NERSC), a U. S. Department of Energy Office of Science User Facility, operated under Contract No. DE-AC02-05CH11231.

## 3.2 Background

Wide bandgap semiconductors such as GaN, AlN and their alloys have emerged as the materials of choice for high power and high frequency electronic devices [150, 151], as well as a

broad range of photonic devices including UV LEDs, lasers and solar blind photodetectors [152, 153]. Critical for the operation and performance of these devices is a precise control of the doping level in the different layers of the structure. To date, however, it has remained extremely challenging to achieve efficient p-type conduction of AlN and AlGaN with relatively high Al content, which has been identified as one of the major obstacles to realize high performance optoelectronic devices operating in the mid and deep UV spectra. Magnesium has been established as the only viable p-type dopant of group III-nitride semiconductors [51]. However, it exhibits very large activation energy (up to 600 meV) in Al-rich AlGaN [154-156], severely limiting the doping efficiency and the realization of large hole concentration at room temperature. Extensive studies have been performed to realize low-resistivity p-type AlGaN, including the use of a high V/III ratio to suppress formation of compensating nitrogen vacancies, superlattices consisting of alternating AlGaN layers, metal modulation epitaxy, Mg δ-doping, indium as a surfactant and polarization-induced doping, but with very limited success [47-49, 89-91, 157-169]. For example, the lowest resistivity reported for p-type $Al_{0.85}Ga_{0.15}N$ epilayers [165] to date is well over $10^3$ Ω·cm, which is more than three orders of magnitude larger than that of Mg-doped GaN.

To achieve p-type AlGaN with large hole concentration and low resistivity, it is essential to incorporate large densities of Mg-dopant atoms. At very large concentrations (~$10^{19}$-$10^{20}$ cm$^{-3}$), an Mg impurity band is expected to form, which enables hole hopping conduction [170, 171]. Moreover, the significantly broadened acceptor energy levels at large Mg-doping concentrations, together with the band tailing effect, also reduces the ionization energy for a fraction of Mg-dopants. In practice, however, it becomes more difficult to incorporate Mg into AlGaN with increasing Al concentration, due to the larger formation enthalpy (lower solubility) for Mg

substituting Al in the AlGaN lattice sites, compared to Ga [154, 172]. The formation energy for various compensating point defects also depends critically on the position of the Fermi level [51, 154].

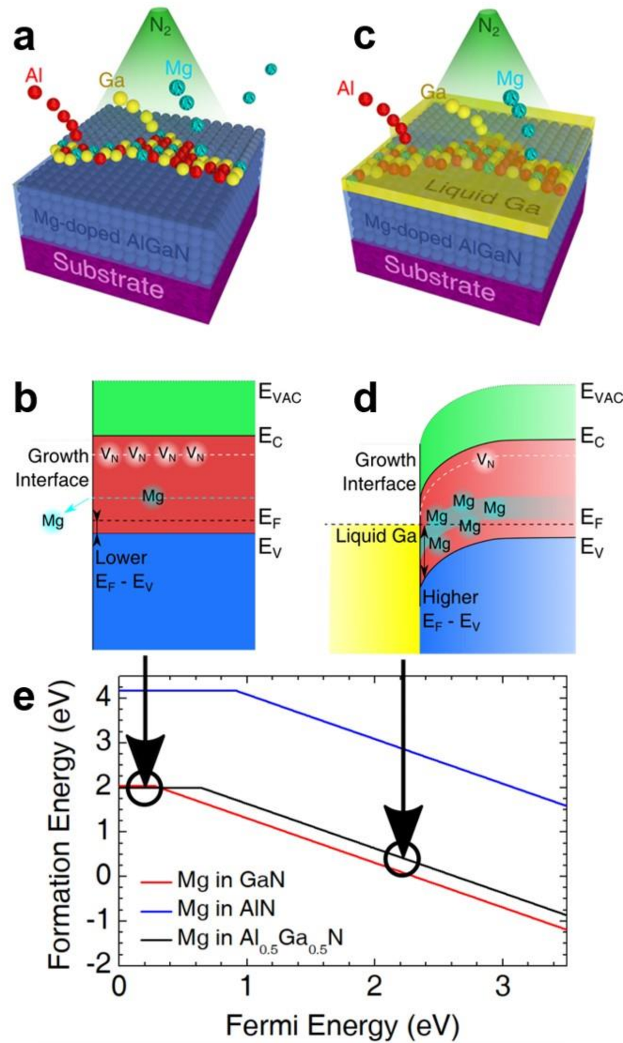


*Figure 3.1:(a) Schematic of conventional epitaxy. (b) Energy band diagram of the Mg-doped AlGaN layer during conventional epitaxy. (c) Schematic of metal-semiconductor junction assisted epitaxy, with the presence of a liquid Ga layer on the surface during epitaxy. (d) Energy band diagram at the growth front of Mg-doped AlGaN during metal-semiconductor junction assisted epitaxy, showing the pinning of the surface Fermi level away from the valence band edge. (e) Calculated formation energy for Mg substitution in GaN, AlN, and $Al_{0.5}Ga_{0.5}N$ as a function of the separation between the Fermi level and the valence band with substitutional Mg formation energies for the different growth processes indicated by their respective arrows.*

During conventional epitaxy, with Mg-dopant incorporation, the Fermi level shifts towards the valence band edge, illustrated in Figs. 3.1(a) and (b), which significantly reduces the formation energy for carbon, oxygen, and nitrogen vacancies [90, 154, 173, 174]. These defects have a strong compensating effect and further degrade the structural, electronic, and optical properties of Mg-doped AlGaN. In addition, the formation energy of N-substitutional and interstitial Mg incorporation decreases drastically with Mg incorporation, and becomes comparable to that of Al(Ga)-substitutional Mg incorporation when the Fermi level is positioned close to the valence band edge, further limiting the doping efficiency and the achievement of large hole concentrations. Evidently, some of the critical issues for achieving efficient p-type conduction of AlGaN can be well addressed, if the Fermi level at the growth front can be tuned away from the valence band during the epitaxy of p-type (Mg-doped) AlGaN.

To overcome these fundamental challenges, we investigate a unique epitaxial growth process – metal-semiconductor junction assisted epitaxy – of ultrawide bandgap AlGaN. Illustrated in Fig. 3.1(c), the epitaxy of AlGaN is performed in metal (Ga) rich conditions by using plasma-assisted MBE. The excess Ga layer leads to the formation of a metal-semiconductor junction during the epitaxy of Mg-doped AlGaN, which pins the Fermi level away from the valence band at the growth front, illustrated in Fig. 3.1(d). In this unique epitaxy process, the Fermi level position is decoupled from Mg-dopant incorporation, *i.e.,* the surface band bending allows the formation of a nearly n-type growth front despite p-type dopant incorporation, which is in direct contrast to the fixed Fermi level position near the valence band edge during the conventional epitaxy of Mg-doped AlGaN. As such, the formation energy for substitutional Mg is dramatically

reduced, even when very large densities of Mg-dopant atoms are incorporated, which is accompanied by a significant suppression of the formation of compensating defects. Epitaxy of AlGaN under metal-rich conditions was reported previously. However, the role of Fermi-level tuning at the growth front and the resulting effect on the enhanced substitutional incorporation of Mg and suppressed compensating defect formation was not identified [54, 70, 175, 176]. Figure 3.1(e) illustrates the variation of the theoretically calculated substitutional formation energy, for Mg in GaN, AlN, and $Al_{0.5}Ga_{0.5}N$, with the energy separation between the Fermi level and valence band maximum. By increasing the separation between the Fermi level and valence band, the formation energy is reduced to only ~0.43 eV for metal-semiconductor junction assisted epitaxy of AlGaN, which is ~1.6 eV lower than that during growth using conventional epitaxy (further details on the simulations can be found in Appendix C). This powerful method simply relies on the spontaneous formation of a metal-semiconductor junction at the growth interface by excess Ga and does not involve any modification of the system under use. In this growth regime, the Al composition of AlGaN can be controllably varied by tuning the Al material flux while keeping the nitrogen flow rate constant. This is because the bond strength of Al-N is much stronger compared to that of Ga-N [177, 178] and, as a consequence, Al-N will preferably form while any excess Ga will accumulate on the surface to form the metal-semiconductor junction during epitaxy. Utilizing this technique, we have demonstrated that Mg incorporation in AlGaN can be enhanced by nearly one order of magnitude compared to the conventional growth process: Mg concentration ~$2\times10^{20}$ $cm^{-3}$ was measured in $Al_{0.75}Ga_{0.25}N$ for a moderate Mg flux of ~$7\times10^{-8}$ Torr. A significant reduction of carbon impurity incorporation was also confirmed through detailed secondary ion mass spectrometry (SIMS) measurements. Significantly, a free hole concentration of ~$4.5\times10^{17}$ $cm^{-3}$ was measured for $Al_{0.9}Ga_{0.1}N$, with resistivity values <5 Ω·cm, which is nearly three orders

of magnitude lower compared to previous reports [165]. Ultraviolet 280 nm light-emitting diodes fabricated using the two methods demonstrated significant improvements in the device characteristics and efficiency for the samples grown by metal-semiconductor junction assisted epitaxy, as compared to the sample grown using the conventional growth mode.

### 3.3 Epitaxial Growth of Mg-doped AlGaN

The samples used in this work were grown on ~1 μm AlN-on-sapphire substrates from DOWA Holdings Co. Ltd. using a plasma-assisted Veeco Gen 930 MBE system. The Mg-doped AlGaN epilayers were grown at a temperature ~700 °C (thermocouple reading), and the Al flux was varied for samples with different Al compositions. The nitrogen flow was 0.4 standard cubic centimeter per minute, with a forward plasma power of 350 W. For the samples that were grown using conventional epitaxy, the Ga flux was adjusted such that the growth was under slightly nitrogen-rich conditions. For the samples grown using metal-semiconductor junction assisted epitaxy, the growth occurred under conditions of excess Ga. In such a growth regime the Al composition of AlGaN can be controllably varied by tuning the Al material flux while keeping the nitrogen flow rate constant. This is because the bond strength of Al-N is much stronger compared to that of Ga-N [162] and, as a consequence, Al-N will preferably form while any excess Ga will accumulate on the surface to form the metal-semiconductor junction during epitaxy. The RHEED pattern was closely monitored during epitaxy to determine the growth condition. A relatively dim and streaky RHEED pattern indicated that the growth was under metal-rich conditions, whereas a brighter pattern with segmented streaks suggests the growth is in slightly N-rich conditions.

Growth was initiated with an undoped AlN buffer layer, followed by ~30 nm undoped AlGaN layer before the growth of the Mg-doped AlGaN layer. The thickness of the AlGaN layers for Hall measurement was approximately 430 nm. For the samples grown for Hall measurements, the growth is terminated with a ~2 nm p-GaN capping layer, which was subsequently etched in the fabrication process for Hall measurements.

For the samples on which SIMS was performed, the grown structure consisted of several AlGaN layers grown with different Mg fluxes, with undoped layers in between. The Mg flux used in the different layers of the samples on which SIMS was performed was measured at different temperatures before every growth, the BFM equipped in the MBE system.

The LED heterostructure consists of a 250 nm thick Si-doped $Al_{0.7}Ga_{0.3}N$ layer, multiple $Al_{0.45}Ga_{0.55}N/Al_{0.7}Ga_{0.3}N$ quantum wells, 60 nm thick Mg-doped AlGaN layer, and 3 nm p-GaN contact layer. The first 30 nm Mg-doped AlGaN layer was graded from an Al composition ~70% to 50% to make use of polarization induced doping to maximize hole injection into the active region, followed by a 30 nm thick Mg-doped $Al_{0.5}Ga_{0.5}N$. An AlGaN electron blocking layer was also incorporated to reduce electron overflow. The device active region was calibrated for emission at ~280 nm.

## 3.4 Effect of Growth Method on Mg Incorporation

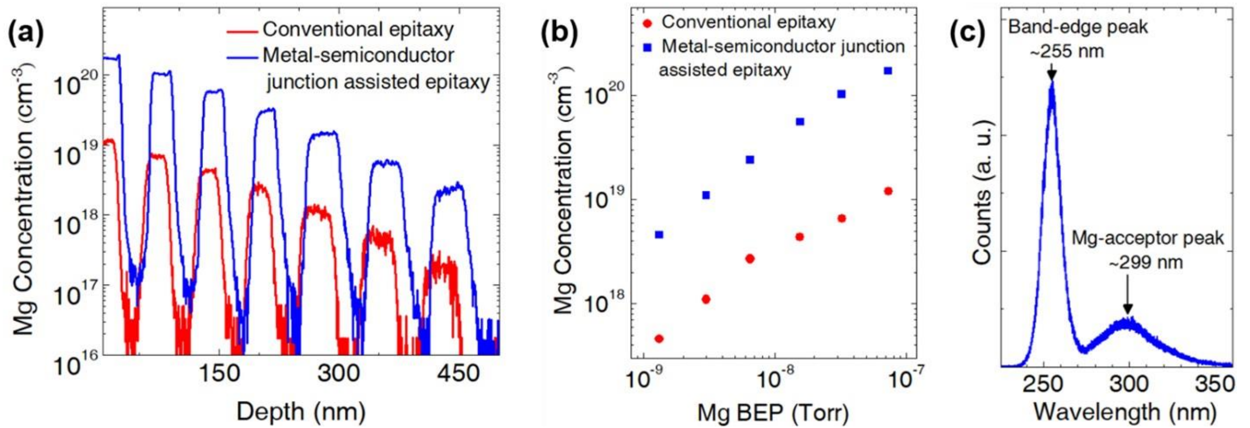


*Figure 3.2:(a) Mg atom concentration versus depth obtained from SIMS measurements on Mg-doped $Al_{0.75}Ga_{0.25}N$ grown using metal-semiconductor junction assisted epitaxy and conventional epitaxy. (b) Mg concentration versus the Mg flux for Mg-doped $Al_{0.75}Ga_{0.25}N$ grown using metal-semiconductor junction assisted epitaxy and conventional epitaxy. (c) Photoluminescence spectra of a Mg-doped $Al_{0.75}Ga_{0.25}N$ sample grown using metal-semiconductor junction assisted epitaxy with band-edge peak and Mg-acceptor peak shown with arrows.*

Two samples with nearly identical Al composition of ~75% were grown, with sample A grown under Ga-rich conditions, using metal-semiconductor junction assisted epitaxy, to ensure complete coverage of the substrate surface with metallic Ga during growth, while Sample B was grown under nearly stoichiometric conditions using the conventional growth mode but with otherwise identical conditions, *e.g.,* the same growth rate and same Mg fluxes, for corresponding layers. Subsequently, Mg concentrations were obtained using SIMS measurements. Figure 3.2(a) shows the Mg atom concentration profile for the two samples, wherein the different Mg-doped AlGaN layers are separated by undoped layers. It is seen that, with the use of metal-semiconductor junction assisted epitaxy, Mg concentrations are significantly higher than those grown using the conventional growth method. Variations of the Mg incorporation vs. Mg flux, measured as beam equivalent pressure (BEP) for the two samples are further plotted in Fig. 3.2(b). For both samples, Mg concentration increases with Mg BEP. However, the Mg atom density is over an order of

magnitude higher for Sample A grown with metal-semiconductor junction assisted epitaxy, as compared to Sample B using the conventional process. The maximum Mg incorporation achieved for Sample A was ~$2\times10^{20}$ Mg atoms $cm^{-3}$, without showing any sign of saturation. The significantly enhanced Mg incorporation is attributed to the reduced formation energy for Al(Ga)-substitutional Mg incorporation [51, 154, 174] when the Fermi level is pinned away from the valence band edge by utilizing the metal-semiconductor junction at the growth front. The C-impurity concentration was significantly reduced compared to MOCVD. For the sample grown using metal-semiconductor junction assisted epitaxy, the carbon concentration is limited by the measurement background of SIMS (~$1\times10^{16}$ $cm^{-3}$). For comparison, carbon concentrations ~$5\times10^{16}$ $cm^{-3}$ to $2\times10^{18}$ $cm^{-3}$ have been commonly measured in Al-rich AlGaN grown by MOCVD [179]. The pinning of Fermi level at the growth front through metal-semiconductor junction assisted epitaxy also leads to a significant decrease in the formation of point defects, which explains the observation that undoped (Al)GaN layers grown under Ga-rich conditions showed approximately three orders of magnitude higher resistivity compared to films grown under conventional conditions [70].

We further studied the photoluminescence properties of the sample grown using metal-semiconductor junction assisted epitaxy. A typical photoluminescence spectrum for a Mg-doped $Al_{0.75}Ga_{0.25}N$ sample is shown in Fig. 3.2(c). A strong peak near the band-edge at ~255 nm (4.86 eV) was measured, accompanied with the Mg-acceptor related transition at ~298 nm (4.16 eV). It has been previously reported that this emission originates from a donor-acceptor pair transition in Mg-doped AlGaN epilayers [54]. The broad linewidth of the Mg-acceptor related transition and its partial overlap with the band-edge luminescence emission indicates a very large spread of the

Mg-acceptor energy levels, extending nearly to the valence band edge of AlGaN. Evidently, the significantly enhanced Mg dopant incorporation can not only lead to the formation of an impurity band for hole hopping conduction [49, 170], but more importantly, results in substantially reduced activation energies for a portion of Mg-dopants, thereby enabling the presence of large hole carrier concentrations at room temperature in AlGaN, that were not possible otherwise [180].

## 3.5 Low-Resistivity p-type AlGaN Layers

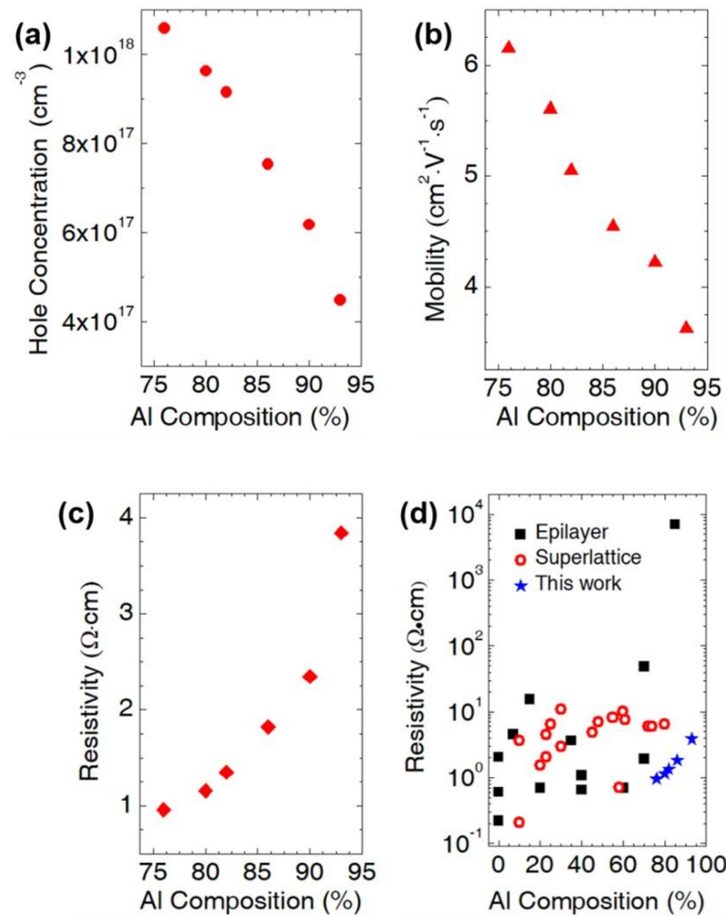


*Figure 3.3: Room-temperature Hall measurement data for Mg-doped AlGaN epilayers plotted against Al composition, showing (a) free hole concentration, (b) hole mobility, (c) resistivity and (d) resistivities of Mg-doped AlGaN layers obtained from literature and this work.*

By employing metal-semiconductor junction assisted epitaxy, a series of Mg-doped samples with Al compositions varying from ~75% up to ~90% were grown. Atomic force microscopy measurements indicated a smooth surface with roughness below 1 nm for all the samples. To fabricate the samples for Hall measurements, metal contacts consisting of Ni (20 nm)/Al (100 nm)/Au (20 nm) were defined using photolithography and deposited by e-beam evaporation, followed by annealing at 500 °C for 5 minutes in the presence of air. The thin p-GaN contact layer was subsequently isolated and removed using plasma etching. Hall measurements were performed on the samples, using the van der Pauw method, to determine the hole concentration, hole mobility and resistivity of the AlGaN layers for temperatures ranging from room temperature to 500 °C.

The room temperature hole concentration is observed to monotonically decrease with increasing Al content, illustrated in Fig. 3.3(a). Figure 3.3(b) shows variations of hole mobility with the Al composition. The decrease in hole concentration and mobility with increasing Al composition can be explained by a reduction in Mg incorporation for alloys with a higher Al mole fraction due to the lower solubility of Mg and the increased formation enthalpy for Al-substitutional Mg. Even for the incorporated Mg atoms, the increase in the activation energy of the Mg-acceptor with increasing Al content further shrinks the free hole concentration. These factors result in an increase in the resistivity for Mg-doped AlGaN layers with increased Al composition, shown in Fig. 3.3(c). However even for $Al_{0.9}Ga_{0.1}N$, the measured resistivity remains below 5 $\Omega \cdot$cm. The resistivity values of some previously reported Mg-doped AlGaN layers [94] are plotted vs. Al compositions in Fig. 3.3(d), along with the resistivity of the AlGaN layers obtained in this work. It is seen that the resistivities of Mg-doped AlGaN grown using metal-

semiconductor junction assisted epitaxy is nearly one to three orders of magnitude lower compared to previously reported results.

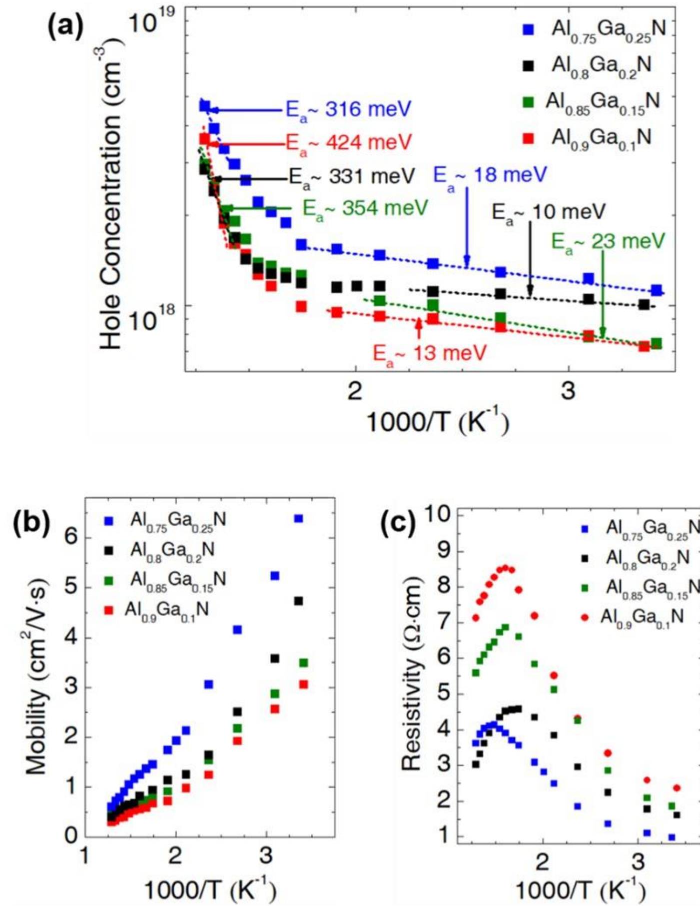


*Figure 3.4: Temperature dependent Hall measurement of Mg-doped AlGaN epilayers grown by metal-semiconductor junction assisted, with Al content between 75% and 90%, for (a) hole concentration, (b) hole mobility and (c) resistivity plotted against the inverse of temperature.*

The variations of the hole concentration vs. temperature for Mg-doped AlGaN samples with different Al compositions was also measured, illustrated in Figure 3.4(a). A low activation energy (~10-20 meV) at temperatures less than 600 K is seen in these samples, which is characteristic of hole hopping conduction in the impurity band and can also be partly explained that a portion of the Mg dopants have significantly reduced activation energy, evidenced by the photoluminescence

spectrum shown in Fig. 3.2(c). At higher temperatures, more Mg-dopants get activated, contributing to holes in the valence band. This leads to a sharp increase in hole concentration at elevated temperatures (>650 K), which is characterized by a large activation energy (~300-400 meV). Such activation energy values, however, are somewhat lower than those theoretically expected for AlGaN alloys with Al compositions ~75-90%. This can be explained by the presence of band-tailing effects and the significantly broadened acceptor energy level distribution, which effectively reduces the activation energy for a portion of Mg-acceptors. The measured hole mobility, shown in Fig. 3.4(b), has a monotonically decreasing trend with increasing temperature, as expected due to an increase in phonon scattering. The resistivity, shown in Fig. 3.4(c), is first observed to increase with temperature between 300 K and ~650 K due to the decrease in hole mobility and relatively small change in hole concentration. At higher temperatures, when the Mg acceptors get thermally activated, the dramatic rise in hole concentration results in the observed decrease in resistivity.

### 3.6 UV LED Fabrication and Measurements

The significantly reduced resistivity of Mg-doped AlGaN, enabled by the unique metal-semiconductor junction assisted epitaxy, is crucial to improve the efficiency of optoelectronic devices operating in the mid and deep UV wavelengths. AlGaN UV LEDs emitting at ~280 nm were grown using this approach and the device characteristics were compared with those of identical LEDs grown using conventional epitaxy.

The UV LED fabrication process involves the use of standard photolithography, dry etching and contact metallization techniques. The device mesa has an area 50 μm × 50 μm. A Ti (40 nm)/Al

(120 nm)/Ni (40 nm)/Au (50 nm) metal stack was deposited on n-AlGaN and annealed at 750 °C for 30 seconds in nitrogen ambient to form the n-metal contact. A Ni (20 nm)/Al (100 nm)/Au (20 nm) metal stack was deposited on p-AlGaN and annealed at 500 °C for 5 minutes in air to form p-metal contact.

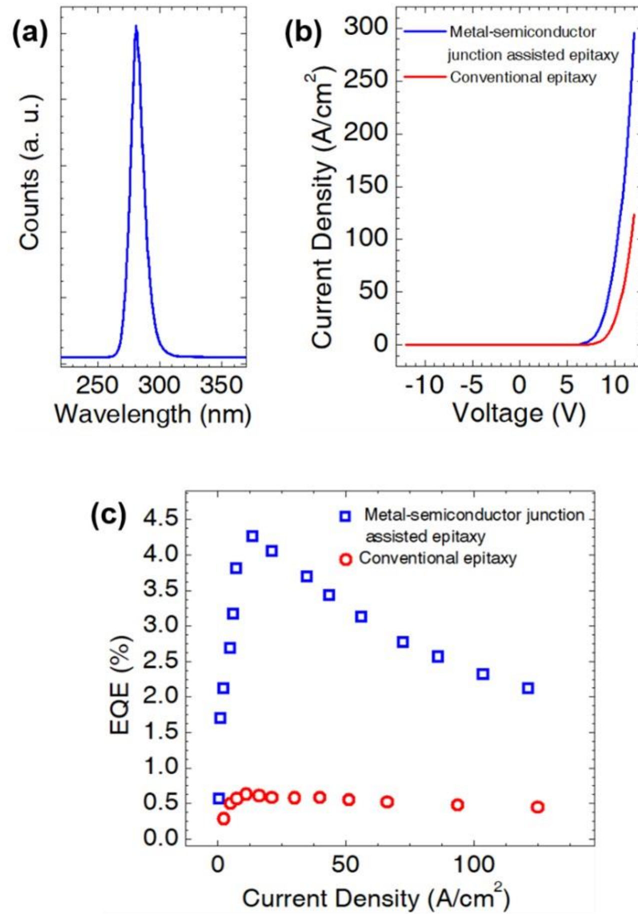


*Figure 3.5:(a) EL spectrum for an UV LED grown using metal-semiconductor junction assisted epitaxy. (b) I-V characteristics for LEDs grown using metal-semiconductor junction assisted epitaxy and conventional epitaxy. (c) EQE versus current density for these devices.*

A typical electroluminescence spectrum is shown in Fig. 3.5(a), with a narrow linewidth ~11 nm. The current-voltage characteristic is shown in Fig. 3.5(b), which exhibits a turn-on voltage of ~7 V for the LED grown using metal-semiconductor junction assisted epitaxy, while we see a turn-

on voltage ~9 V for the conventional epitaxy sample. The higher turn-on voltage is likely a result of the ineffective Mg-doping when using conventional epitaxy. The external quantum efficiency (EQE) was further measured directly on wafer, without any packaging, substrate removal, or cooling. Shown in Fig. 3.5(c), a maximum on-wafer EQE of ~4.3% was measured at room temperature, which is significantly better than the LED device grown using the conventional epitaxy process, which exhibits a maximum EQE of ~0.6%. This device performance is also better than other previously reported AlGaN UV LEDs grown by MBE around this wavelength [54, 68, 70, 99]. The improved device-characteristics seen in the samples grown using metal-semiconductor junction assisted epitaxy highlights the significance of efficient p-type conduction on device performance. It is also worth noting that the measured EQE can be significantly increased through proper packaging of devices to increase the light extraction efficiency, and by employing more comprehensive techniques to capture all the emitted light, such as the use of an integrating sphere.

## 3.7 Summary

In summary, it was demonstrated that by tuning the surface Fermi level using metal-semiconductor junction assisted epitaxy, efficient p-type conduction can be achieved for Al-rich AlGaN that was not previously possible. The presence of a metal-semiconductor interface at the growth front pins the Fermi level away from the valence band edge, which can significantly enhance Al(Ga)-substitutional Mg-dopant incorporation and further reduces the formation of compensating point defects, as demonstrated in this work, both theoretically and experimentally. It should also be noted that the presence of surface states, which are strongly affected by growth conditions as has been previously described for both polar [181] and non-polar [182] surfaces, may

further play a role in pinning the Fermi level away from the valence band, although the surface state density structure at the elevated temperatures required for crystal growth has remained unknown. As such, large concentrations of Mg-acceptors can be incorporated in Al-rich AlGaN, which enables the formation of a Mg impurity band. Al-rich AlGaN epilayers, with resistivity values below 1 Ω·cm for $Al_{0.75}Ga_{0.25}N$ and ~4 Ω·cm for $Al_{0.9}Ga_{0.1}N$ have been measured, which are essentially required for achieving high efficiency mid and deep UV optoelectronic devices. Deep UV LEDs grown using this method showed a great improvement in external quantum efficiency, and lower turn-on voltage, as compared to devices grown using conventional epitaxy. Such a unique technique can be further extended for the epitaxy/synthesis of a broad range of semiconductor nanostructures and heterostructures to achieve controlled dopant incorporation and to fundamentally improve their structural, electronic, and optical properties.

# Chapter 4. Effect of Electron Blocking Layer on AlGaN UV LED Efficiency

## 4.1 Author Contribution and Copyright Disclaimer

The contents of this chapter were published in the journal Optics Express in June 2019 [98], for which I retain the right to include it in this thesis/dissertation, provided it is not published commercially. The co-authors were Walter Shin, Xianhe Liu, and Zetian Mi from the University of Michigan. I designed, conducted and authored most of the work. X. L. contributed to the growth process. W. S. contributed to the sample characterization and fabrication. The work was supervised by Z. M., who contributed to the design of the experiments. This work was supported by the University of Michigan, College of Engineering.

## 4.2 Background

To date, AlGaN LEDs operating in the UV-B and UV-C bands still exhibit very low efficiency, primarily due to the presence of large densities of defects and dislocations in the device active region, poor current conduction, and inefficient light extraction [39, 40, 49, 69, 152, 183]. For example, it has remained difficult to achieve efficient p-type conduction in high Al content AlGaN, due to several issues associated with Mg-dopant, including extremely high activation energy (up to ~600 meV), poor solubility, and the tendency towards self-compensation through the formation of point defects [51, 154]. The ineffective Mg-doping leads to very low concentrations of free holes in Al-rich AlGaN [54, 91, 157]. On the other hand, electron concentrations in the range of ~$10^{18}$-$10^{19}$ $cm^{-3}$ can be readily achieved in n-type Al-rich AlGaN

using Si as a dopant [52, 53, 184]. This large disparity in the electron and hole concentrations, together with the difference in the carrier mobility (~25-50 $cm^2/V\cdot s$ [53, 185] and ~1-5 $cm^2/V\cdot s$ [94, 175] for electrons and holes in Al-rich AlGaN, respectively) leads to highly asymmetric charge carrier transport properties of n and p-type AlGaN cladding layers employed in a mid and deep UV LED structures. The resistivity of p-type (Mg-doped) AlGaN epilayers increases rapidly with increasing Al content, with values generally in the range of $10\sim10^4$ $\Omega\cdot cm$ for AlGaN layers with over 70% Al composition. The corresponding resistivity values reported for n-type (Si-doped) Al-rich AlGaN are nearly three to six orders of magnitude lower, for similar Al composition, in the range of 0.01-1 $\Omega\cdot cm$. Consequently, there is a significant electron overflow in the device active region, which leads to poor carrier injection efficiency under moderate current injection conditions. Such an issue becomes more severe for AlGaN LEDs operating at shorter wavelengths, due to the further reduced free hole concentration.

To prevent electron overflow, a high Al composition p-type (Mg-doped) AlGaN EBL has been commonly incorporated between the device active region and p-AlGaN layer [186-188]. Such a technique has shown to be highly effective to reduce electron overflow and to improve the efficiency of GaN-based visible LEDs [189-192]. To date, however, there have been few studies on the effectiveness of this technique on the performance of mid and deep UV AlGaN LEDs [95-97, 193, 194]. In wide bandgap AlGaN LEDs, the incorporation of a high Al composition AlGaN EBL can severely compromise hole injection into the device active region, due to the large valence band offset at the hetero-interface and the significantly reduced hole concentration with increasing Al composition. The resulting increase in device resistivity also leads to undesired heating effect and reduced wall-plug efficiency.

In an effort to minimize electron overflow without compromising hole injection into the device active region, we have studied the effect of various n-type EBLs, incorporated between the active region and the n-AlGaN cladding layer, on the performance of high Al-content AlGaN UV LEDs. The LED heterostructures were grown on sapphire wafer by plasma-assisted MBE and were designed to operate at ~280 nm. The n-type EBL consists of Si-doped AlN/AlGaN short period superlattices, which allows for effective cooling of "hot" electrons before their injection into the device active region and therefore can minimize electron overflow. The polarization enhanced doping through the use of the superlattice can simultaneously improve lateral conductivity and will mitigate current crowding effects [68, 143]. Efficient injection of holes into the device active region, on the other hand, can be achieved due to the absence of any potential barrier. Direct on wafer measurements showed a maximum EQE ~4.4%, which is significantly higher compared to that (~0.5-1%) of conventional mid-UV AlGaN LEDs grown by MBE [68, 84, 99]. The reduced barrier to hole injection also contributes to a lower turn-on voltage for the n-type EBL samples. The peak wall-plug efficiency is improved from ~0.5% to ~2.8%, when we switch from a p-type EBL to an n-type EBL.

## 4.3 Epitaxy of UV LED Structures

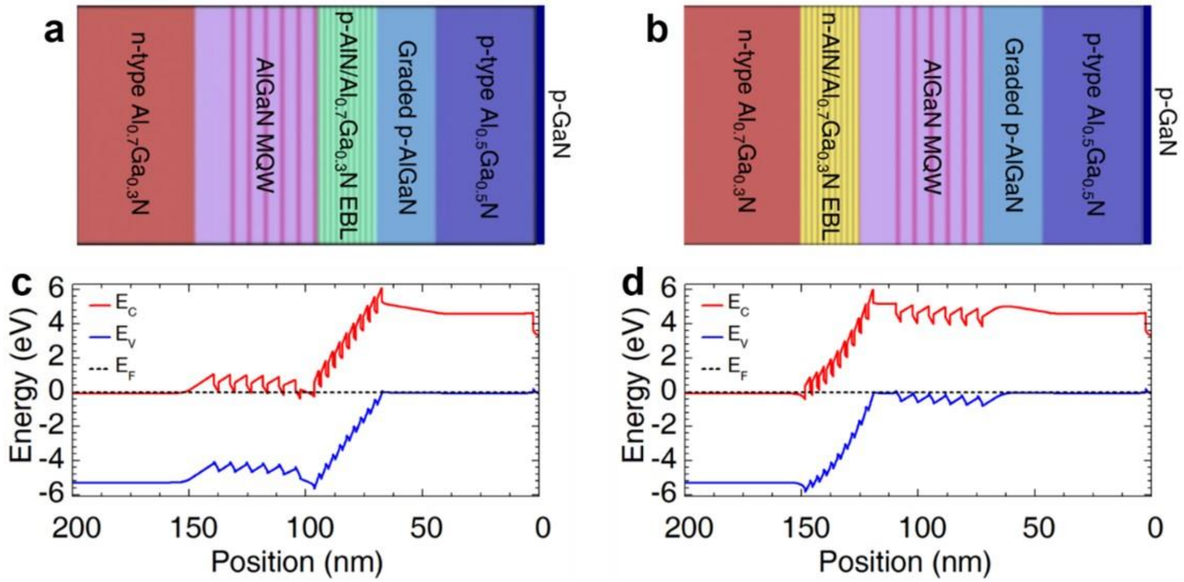


*Figure 4.1: Schematic illustration of AlGaN mid-UV LEDs with the incorporation of (a) a p-type AlN/AlGaN superlattice EBL and (b) an n-type AlN/AlGaN superlattice EBL. Equilibrium energy band diagram for the LED heterostructures with (c) a p-type AlN/AlGaN superlattice EBL and (d) an n-type AlN/AlGaN superlattice EBL.*

AlGaN mid-UV LED heterostructures were grown using a Veeco Gen 930 MBE system on AlN-on-sapphire templates from DOWA Holdings Co. Ltd. The growth parameters include a substrate temperature of 700 °C and a growth rate of ~150 nm/hr. The samples were grown under slightly metal (Ga) rich conditions to enhance Mg dopant incorporation. Figure 4.1(a) illustrates the schematic for the LED structure using a conventional p-type EBL (Mg-doped AlN/$Al_{0.7}Ga_{0.3}N$ superlattice). The LED heterostructure incorporating an n-type AlN/$Al_{0.7}Ga_{0.3}N$ superlattice EBL is shown in Fig. 4.1(b). All the growths were initiated with a ~50 nm undoped AlN buffer, followed by a 300 nm thick $n^+$-$Al_{0.7}Ga_{0.3}N$ contact layer. The active region consists of six periods of $Al_{0.45}Ga_{0.55}N$ (~2 nm)/$Al_{0.7}Ga_{0.3}N$ (~5 nm) quantum wells. The p-AlGaN cladding layer consists of Mg-doped AlGaN with Al content graded linearly from 70% to 50% in ~20 nm, followed by the growth of ~20 nm p-type $Al_{0.5}Ga_{0.5}N$ and 2 nm p-GaN contact layer. Further details about the

growth and composition control of the AlGaN epilayers can be found elsewhere [195]. The measured internal quantum efficiency of the quantum wells is ~30-50%, as has been detailed in a previous work [196]. SIMS measurements performed on the samples confirmed that differently doped layers were well formed with extremely abrupt interfaces. Hall measurements using an Ecopia HMS-3000 Hall measurement setup showed resistivity values of ~ 0.001 Ω·cm and ~ 0.7 Ω·cm for the n-type and p-type $Al_{0.7}Ga_{0.3}N$ layers, respectively.

*Table 4.1: AlGaN mid-UV LED samples with different EBL designs.*

| LED | EBL Design |
| --- | --- |
| A | 10× AlN:Mg (1.5 nm)/p-$Al_{0.7}Ga_{0.3}N$ (1 nm) |
| B | 10× AlN:Si (1.5 nm)/n-$Al_{0.7}Ga_{0.3}N$ (1 nm) |
| C | 20× AlN:Si (1.5 nm)/n-$Al_{0.7}Ga_{0.3}N$ (1 nm) |

Listed in Table 4.1, we have studied AlGaN mid-UV LEDs incorporating EBLs with different thicknesses and dopants. Three representative designs, referred to as A, B, and C, are described below. LED A has a p-type EBL which consists of ten periods of Mg-doped AlN (~1.5 nm)/$Al_{0.7}Ga_{0.3}N$ (~1 nm) superlattice placed between the active region and the p-AlGaN cladding layer. 1-D Poisson-Schrödinger equations, considering the effect of the strong spontaneous polarization present in these alloys, were used to generate the equilibrium band diagrams for the different structures [197]. From the equilibrium band diagram shown in Fig. 4.1(c), a significant barrier to hole injection is observed, which has a deleterious effect on the device performance, especially at low voltages. The designs of LEDs B and C are identical to that of LED A, except that the p-type EBL is replaced by an n-type EBL incorporated between the n-AlGaN cladding layer and the active region. The n-type EBLs in LEDs B and C consist of ten and twenty periods of Si-doped AlN (~1.5 nm)/$Al_{0.7}Ga_{0.3}N$ (~1 nm) superlattice, respectively. The equilibrium energy

band diagram for LED B is schematically shown in Fig. 4.1(d). It is observed that there is a reduced barrier for hole injection to the active region, while presenting a barrier to electron injection to minimize electron overflow. Similar effect is also seen from the energy band diagram of LED C with twenty periods of n-type $AlN/Al_{0.7}Ga_{0.3}N$ superlattice (not shown).

## 4.4 Fabrication and Characterization of Mid-UV LEDs

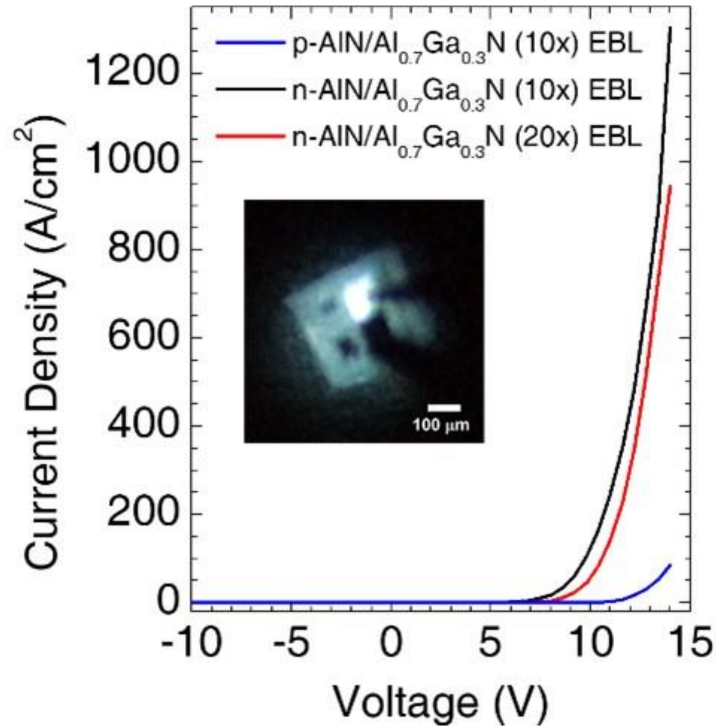


*Figure 4.2: I-V characteristics for AlGaN mid-UV LEDs measured at room temperature. Blue curve: LED A with 10× p-$AlN/Al_{0.7}Ga_{0.3}N$ superlattice EBL; Black curve: LED B with 10× n-$AlN/Al_{0.7}Ga_{0.3}N$ superlattice EBL; Red curve: LED C with 20× n-$AlN/Al_{0.7}Ga_{0.3}N$ superlattice EBL. The inset shows a top-emitting 100 μm × 100 μm device from sample B at a current density of ~50 $A/cm^2$.*

In the LED fabrication, Al (200 nm)/Au (100 nm) was first deposited as the p-metal contact, followed by inductively coupled plasma reactive ion etching (ICP-RIE) to define mesas and to expose the $n^+$-AlGaN contact layer. A Ti (40 nm)/Al (120 nm)/Ni (40 nm)/Au (50 nm) metal stack

was deposited to form n-metal contact. The device areal sizes varied from 40 μm × 40 μm to 100 μm × 100 μm. The measured current-voltage characteristics for LEDs A, B, and C are shown in Fig. 4.2. It is seen that the best current-voltage characteristics are obtained for LED B with the incorporation of ten periods of n-AlN/$Al_{0.7}Ga_{0.3}N$ superlattices, which has a turn-on voltage ~7 V. Significantly, current density over 1 kA/$cm^2$ was measured at a moderate voltage ~13.5 V [84, 99]. The incorporation of 20 periods of n-AlN/$Al_{0.7}Ga_{0.3}N$ superlattices (LED C), however, increases the turn-on voltage, due to the large resistivity of the EBL. In both samples B and C with n-type EBLs, the current-voltage characteristics are better than that of LED A, which has a p-type EBL. The reduced hole injection into the active region with the use of a p-type EBL may contribute to the increased turn-on voltage for LED A, which operates at ~12.5 V for a current density of 20 A/$cm^2$. We also performed studies on AlGaN LEDs with the incorporation of thirty period n-AlN/$Al_{0.7}Ga_{0.3}N$ superlattice EBL as well as a 25 nm thick n-AlN EBL, which showed worse current-voltage characteristics compared to LEDs B and C. In this study Al/Au was used as the p-metal contact layer to enhance the light reflection and emission from the backside of the wafer (sapphire) [198]. Better turn-on voltage is expected with the use of Ni/Au p-metal contact for these devices, which would enhance current injection from the p-contact.

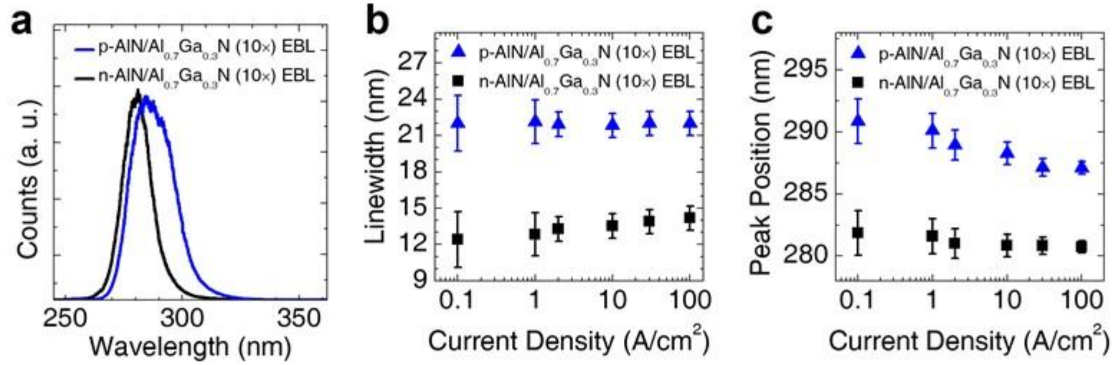


*Figure 4.3: (a) Normalized electroluminescence spectra measured at 100 A/cm$^2$ at room temperature for LED A (10× p-AlN/$Al_{0.7}Ga_{0.3}N$ superlattice EBL) and LED B (10× n-AlN/$Al_{0.7}Ga_{0.3}N$ superlattice EBL). (b) Spectral linewidths versus current density for LEDs A and B. (c) Peak wavelength versus current density for LEDs A and B. The measurement error bars are also shown in (b) and (c).*

To measure the EL spectra of the fabricated LEDs, a Keithley 2400 SMU was used to apply a CW bias, and the emission was collected using an optical fiber coupled to a high-resolution spectrometer and detected by a charge coupled device detector. The normalized electroluminescence spectra for LEDs A and B at a current density of 100 A/cm$^2$ are shown in Fig. 4.3(a). Variations of the spectral linewidth and peak emission wavelength with injection current are further shown in Figs. 4.3(b) and (c), respectively. The devices with the n-EBLs show a relatively narrow linewidth (~12 nm) and highly stable operation. Both the spectral linewidths and emission wavelengths exhibit a negligible dependence on the injection current. For comparison, the sample with p-type EBL (LED A) shows a broader electroluminescence spectrum (~22 nm) than that of the sample with n-type EBL (LED B), despite identical device active regions. The presence of a shoulder at ~292 nm, apart from the main peak at ~282 nm for the LED sample with p-type EBL is explained by the presence of significant electron overflow and the resulting parasitic emission from the p-AlGaN layer.

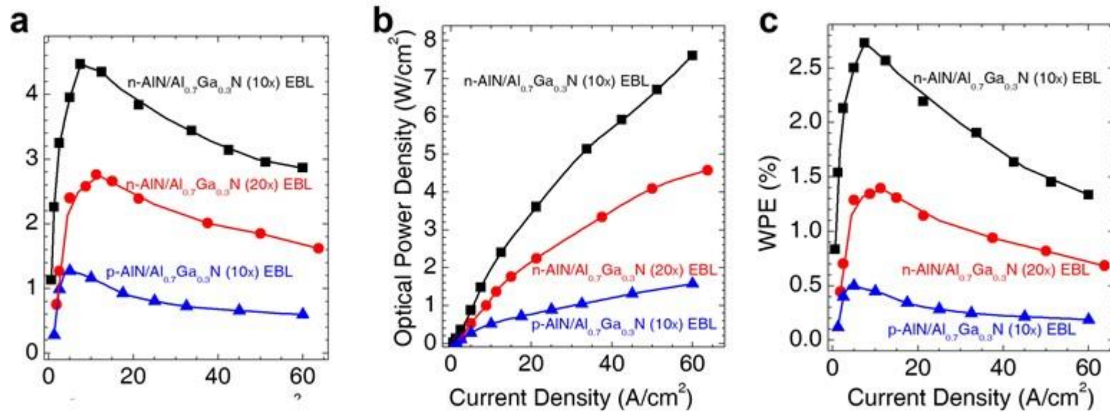


*Figure 4.4:(a) EQE (b) power density, and (c) WPE versus current density measured at room temperature for LED A (10× p-AlN/$Al_{0.7}Ga_{0.3}N$ superlattice EBL), LED B (10× n-AlN/$Al_{0.7}Ga_{0.3}N$ superlattice EBL), and LED C (20× n-AlN/$Al_{0.7}Ga_{0.3}N$ superlattice EBL).*

On-wafer EQE of unpackaged LED devices was measured at room temperature using a Newport 818-ST2-UV silicon photodiode detector connected to a Newport Model 1919-R power meter. To minimize heating effect, voltage pulses with a duty cycle of 1% and a period of 100 µs were supplied to the devices using an AV-1010B pulse generator. The measured EQE is expected to increase significantly if the devices were packaged to optimize light extraction. The EQE plotted against the current density is depicted in Fig. 4.4(a), for each of the LED samples. It is evident that the EQE is significantly higher for the samples grown with an n-type EBL instead of a p-type EBL. The maximum measured EQE is ~4.4% for LED B with ten periods of AlN/$Al_{0.7}Ga_{0.3}N$ superlattice n-EBL, while the EQE peaks at only ~1.3% for LED A with p-type EBL. This further indicates the detrimental impact of p-type EBL on hole injection. As the thickness of n-type EBL superlattice is increased to twenty periods in LED C, the peak EQE also decreases compared to LED B, as a result of less efficient electron injection to the active region. Similar measurements performed on LED samples grown with thirty periods of AlN/$Al_{0.7}Ga_{0.3}N$ superlattice and with a 25 nm AlN n-EBL (not shown) showed a further decrease in EQE, confirming the important role

of n-EBL on the device performance. For comparison, the EQE of previously reported LEDs operating in this wavelength range grown by MBE is generally limited to ~0.5-1% [68, 143, 175]. With the use of a polarization-engineered tunnel junction to enhance hole injection, an EQE ~2.8% was recently reported for an AlGaN LED operating at ~287 nm grown by MBE [99].

Variations of the output power vs. injection current were further studied. Shown in Fig. 4.4(b), LED B exhibits a power density ~7.6 W/cm$^2$ at 60 A/cm$^2$, which is almost a factor of five times higher than that measured for LED A, which has a p-EBL. We also observe a significant droop in the maximum EQE of the fabricated devices when operating at higher biases. This could be related to the presence of electron flow under high biasing voltage, heating effect and/or Auger recombination [199-203]. The wall-plug efficiency of these devices was also measured and plotted in Fig. 4.4(c). The maximum wall-plug efficiency of the device with ten periods of the n-AlN/AlGaN superlattice EBL (LED B) is ~2.8%, which is significantly higher than that (~0.5%) for the LED with p-EBL (LED A).

### 4.5 Summary

Improved performance was reported previously for InGaN based visible LEDs with the use of n-EBL, instead of p-EBL [191, 192, 199, 204]. However, the performance improvement is much more dramatic for AlGaN UV LEDs. In mid and deep UV AlGaN LEDs wherein poor p-type conduction is a primary limiting factor for the device performance, the replacement of the conventional p-type EBL by an optimally designed n-type AlN/AlGaN superlattice EBL can reduce electron overflow without compromising hole transport and injection into the device active

region, thereby better balancing the hole and electron injection to the device active region, while simultaneously increasing the lateral conductivity of electrons and allowing for better current spreading. The more balanced charge carrier transport allows for more efficient recombination in the device active region, thereby improving device performance. Such a unique design is expected to further improve the device performance for LEDs operating at 200-265 nm, wherein p-type doping is further hindered due to the even higher Al content required for these shorter wavelengths.

# Chapter 5. High Efficiency AlGaN/GaN/AlGaN Tunnel Junction UV LEDs

## 5.1 Author Contribution and Copyright Disclaimer

The contents of this chapter were published in the journal Photonics Research in February 2020 [104], for which I retain the right to include it in this thesis/dissertation, provided it is not published commercially. The co-authors were Walter Shin, Jiseok Gim, Robert Hovden and Zetian Mi from the University of Michigan. I designed, conducted and authored most of the work. W. S. contributed to the sample characterization and fabrication. J.G. and R. H. collected the HAADF-STEM images presented. The work was supervised by Z. M., who contributed to the design of the experiments. This work was supported by the Army Research Office under the grant W911NF19P0025 and the University of Michigan, College of Engineering.

## 5.2 Overview

According to the World Health Organization, health-care associated infections (HCAIs) [205] and water-borne illnesses [206] are responsible for thousands of fatalities and billions of dollars in costs each year. Sterilization of medical equipment and water supplies is now frequently utilized to minimize the possibility of infections by neutralizing pathogens, and for this purpose conventional mercury UV lamps have been widely used. Semiconductor optoelectronic devices offer an alternative that is non-toxic, more compact, and more flexible in applications. The AlGaN alloy system is uniquely suited for this purpose as the alloys are direct bandgap semiconductors spanning from ~200 nm to ~365 nm in wavelengths. To date, AlGaN LEDs operating in the UV-

C band (200-280 nm), which is of prime importance for sterilization, exhibit low efficiency, which has been attributed to the poor light extraction associated with transverse magnetic (TM)-polarized light emission [85, 207-209], low luminescence efficiency due to the presence of large densities of defects [42, 210], and inefficient p-type doping [51, 90, 156]. These issues become more severe for LEDs operating at shorter wavelengths which require a higher Al content in the device active region. In this regard, intensive studies have been performed to improve the light extraction efficiency by engineering the energy band structure [211, 212] and by utilizing nanostructures [44, 109, 213, 214]. Various techniques, including epitaxy on nano-patterned substrates and high temperature annealing have also been developed to reduce the formation of defects [215-218]. Recently, EQE over 20% was reported for AlGaN LEDs operating at 275 nm, which, however, had a low WPE of 5.7% [38]. To our knowledge, the best reported EQE for AlGaN LEDs operating at ~265 nm, an important wavelength for water purification and sterilization [219], is ~6.3% for packaged devices grown using MOCVD [152, 220]. Direct on-wafer measurements, however, typically result in lower efficiencies due to reduced light extraction/collection and severe self-heating of the devices, with the best peak EQE of only ~2% at ~265 nm [221, 222]. The maximum wall-plug efficiency of these devices is often much lower, which is fundamentally limited by the large resistance and poor hole injection efficiency, due to the high resistivity of p-type AlGaN. Moreover, the poor p-type conduction, together with the highly asymmetric hole and electron injection efficiencies, can lead to parasitic carrier recombination outside the active region [193, 223], which further exacerbates the heating of the devices and can have a detrimental impact on device performance [224-227]. While using p-GaN as the contact layer may partly alleviate the issue of hole injection to the active region, it has an adverse impact on the light extraction efficiency, due to the significant UV light absorption by GaN [228].

A promising technique to improve hole injection is through the use of a tunnel junction structure, wherein holes are injected into the valence band of the p-type layer by the interband tunneling of electrons to the conduction band of an n-type layer. Using the tunnel junction structure, the high resistance p-AlGaN layer can be replaced by a relatively low resistance n-AlGaN contact layer, which further allows the use of a reflective Al ohmic contact to enhance the light extraction for backside emitting devices [198, 229, 230]. Homojunction tunnel diodes in the III-nitrides have been previously demonstrated using highly doped GaN [22, 231, 232], however the doping required for efficient interband tunneling of carriers becomes extremely difficult to attain in AlGaN alloys due to their higher bandgaps and less efficient p-type doping. Such critical challenges can be addressed, to a certain extent, through polarization engineering by incorporating a thin layer of different composition between the n and p-type layers [23, 25, 233, 234]. Due to the strong spontaneous and piezoelectric polarization, the sheet charges at the hetero-interfaces help to better align the conduction band of the n-type layer with the valence band of the p-type layer, while reducing the width of the depletion region. This results in a dramatic increase in the probability of electron tunneling. Such a technique has been employed in visible LEDs [24] and lasers [235], and has also been demonstrated using an InGaN-based tunnel junction for UV LEDs grown using MBE [100, 229, 230] and GaN-based tunnel junction for UV LEDs grown using MOCVD [236].

In this chapter, we demonstrate the use of a GaN polarization engineered tunnel junction with a p-AlGaN/GaN/n-AlGaN structure, to realize high efficiency AlGaN LEDs operating at 265 nm. A series of samples with different GaN widths, and thicknesses of the top n-AlGaN contact

layer were grown and fabricated, and their effect on device performance was thoroughly studied. Through detailed optimization, we demonstrate LEDs having emission wavelengths ~265 nm with a maximum EQE of 11%. The peak WPE was measured to be 7.6%. It is also observed that these devices exhibit severe efficiency droop at relatively low current densities. The underlying causes have been discussed. This work provides new insights on the performance improvement of AlGaN deep UV LEDs.

## 5.3 Epitaxial Growth of LEDs

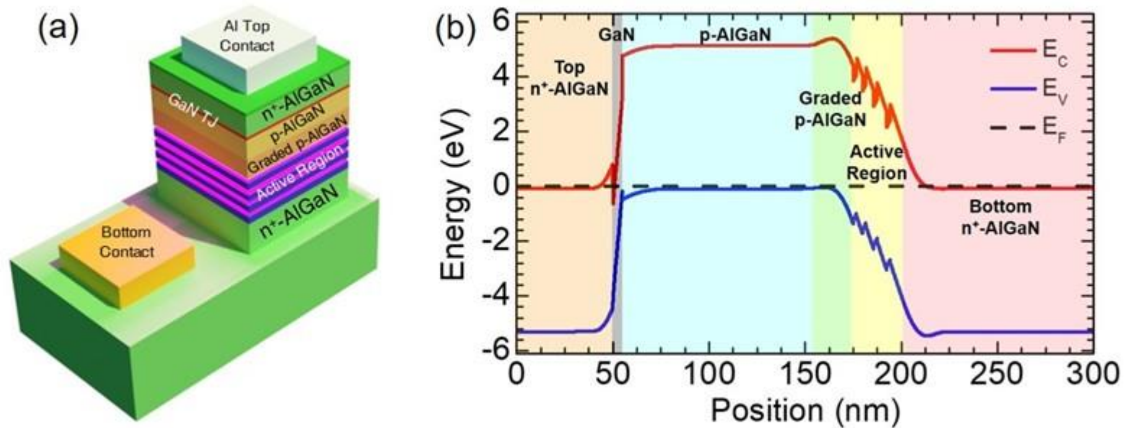


*Figure 5.1:(a) Schematic illustration of the tunnel junction LED structures. (b) Simulated equilibrium band diagram for a representative LED using a 5 nm GaN layer. The different layers used in the structure are labelled and shown with different colors.*

The tunnel junction LED structures were grown in a Veeco Gen 930 PA-MBE system on 1 µm thick AlN-on-sapphire substrates from DOWA Holdings Co. Ltd. A nitrogen flow rate of 0.6 SCCM, with an RF power of 350W was used throughout the growth. The growth rate is ~160 nm/hr for the AlGaN epilayers. The growth was conducted using metal-semiconductor junction assisted epitaxy to enhance Mg-dopant incorporation and to reduce defect formation [94]. A schematic of the LED structures is shown in Fig. 5.1(a). The growth was initiated with a ~50 nm

thick AlN layer, followed by the subsequent AlGaN growth. The initial ~500 nm thick $Al_{0.65}Ga_{0.35}N$ layer was Si-doped to form the bottom n-contact. The Al composition of the AlGaN was graded up from 65% to 85% in a thickness of ~20 nm immediately before the active region. The active region consisted of four AlGaN quantum wells with compositions ~60% designed for peak emission at ~265 nm. The AlGaN barriers, with higher Al compositions, were grown with decreasing thicknesses, from ~5 nm to ~3 nm closer to the Mg-doped AlGaN. A graded Mg-doped AlGaN layer, with a thickness of ~20 nm and Al compositions varying from 80% to 65%, followed the last quantum well. The grading down of the Al composition of the AlGaN provides polarization-induced doping which enhances the hole concentration [21]. A ~100 nm thick p-$Al_{0.65}Ga_{0.35}N$ was then grown, followed by the GaN layer. Compared to the previously reported InGaN-based tunnel junction UV LEDs grown by MBE [100, 229, 230, 237], there was no growth interruption for the tunnel junction as the substrate temperature was kept the same as that for the GaN and AlGaN layers. Following the growth of the tunnel junction, the top $n^+$-$Al_{0.65}Ga_{0.35}N$ contact layer was grown. Different design parameters, including the thicknesses of the GaN layer and the top $n^+$-AlGaN contact layer, are listed in Table 5.1. A one-dimensional Poisson-Schrödinger solver was used to simulate the band diagram of a representative structure having 5 nm GaN width as shown in Fig. 5.1(b).

*Table 5.1: List of tunnel junction LED structures.*

| **Sample** | **GaN Thickness** | **Top $n^+$-AlGaN Thickness** |
|---|---|---|
| A | 2.5 nm | 50 nm |
| B | 2.5 nm | 150 nm |
| C | 5 nm | 150 nm |
| D | 10 nm | 150 nm |
| E | 5 nm | 480 nm |

## 5.4 Structural Characterization of the LED Structure

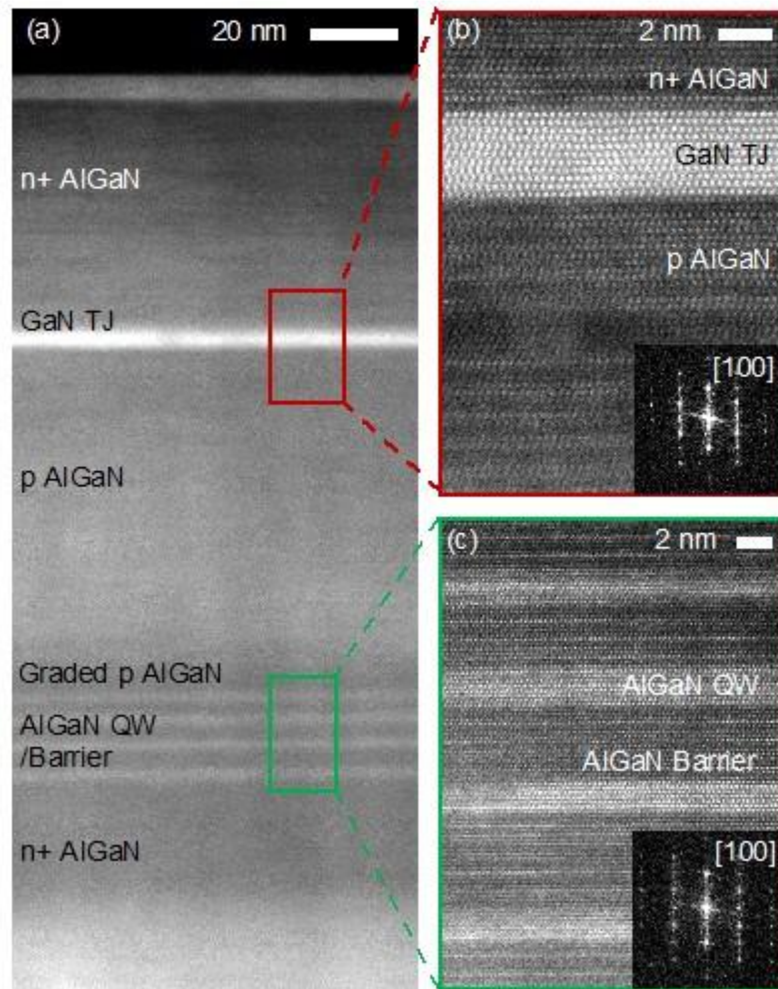


*Figure 5.2:(a) HAADF-STEM overview of cross-sectional AlGaN multilayers shows the complete device structure. (b) High-resolution HAADF-STEM of the p-AlGaN/GaN/n-AlGaN tunnel junction shows crystalline epitaxial growth with sharp interfaces for enhanced hole injection by tunneling. (c) Atomic-resolution HAADF-STEM of $Al_{0.6}Ga_{0.4}N$ quantum wells coupled to $Al_{0.85}Ga_{0.15}N$ barriers with sharp epitaxial interfaces for carrier confinement.*

HAADF-STEM on a representative sample confirms the AlGaN multilayer structure with p-AlGaN/GaN/n-AlGaN tunnel junction and AlGaN quantum well layers, shown in Fig. 5.2(a). The GaN layer (~5 nm) is epitaxially grown between the top $n^+$-AlGaN contact and p-AlGaN layer with sharp interfaces, as can be seen from Fig. 5.2(b). The ratio of HAADF STEM intensity estimates ~64% $\pm$ 6% less Ga in the p-AlGaN layers compared to the Ga concentration in the GaN

layer. The high relative Ga content in the tunnel junction is expected to increase the efficiency of charge carrier injection by tunneling. High-resolution cross-sectional STEM, shown in Fig. 5.2(c), also confirms the epitaxial growth of four AlGaN quantum wells (~ 2 nm) with ~27% $\pm$ 3.5% higher content of Ga relative to adjacent AlGaN barriers (ranging from ~ 5 nm to ~ 3 nm) that confine charge carriers. Fast Fourier transforms (FFT) of the atomic resolution HAADF STEM images confirms the (100) lattice plane of AlGaN multilayers with an orientation that indicates preferred growth along the [001] c-axis direction.

## 5.5 Tunnel Junction Design Optimization

All the 265 nm LED structures were fabricated using the same process to maximize emission from the backside of the wafer. A $BCl_3/Cl_2$ plasma was first used to dry etch the samples down to the bottom n-contact layer, with device mesas having an areal size of 40 μm × 40 μm. This was followed by the deposition of an $HfO_2/SiO_2$ dielectric distributed Bragg reflector (DBR) to increase light reflection towards the backside of the wafer, and also serve as a surface passivation layer. The thicknesses of $HfO_2$ and $SiO_2$ layers are ~30 nm and ~45 nm, respectively, which were calculated based on the measured refractive indices of the dielectric layers and an $Al_{0.65}Ga_{0.35}N$ epilayer, to maximize reflectivity around 265 nm. Openings were then etched into the passivation layer for the deposition of metal contacts. A reflective top contact of Al (250 nm)/Au (50 nm) was then deposited [198, 230], followed by a Ti (40 nm)/Al (120 nm)/Ni (40 nm)/Au (50 nm) metal stack for the bottom n-contact. The metal contacts were annealed at 700 °C for 30 seconds in nitrogen ambient.

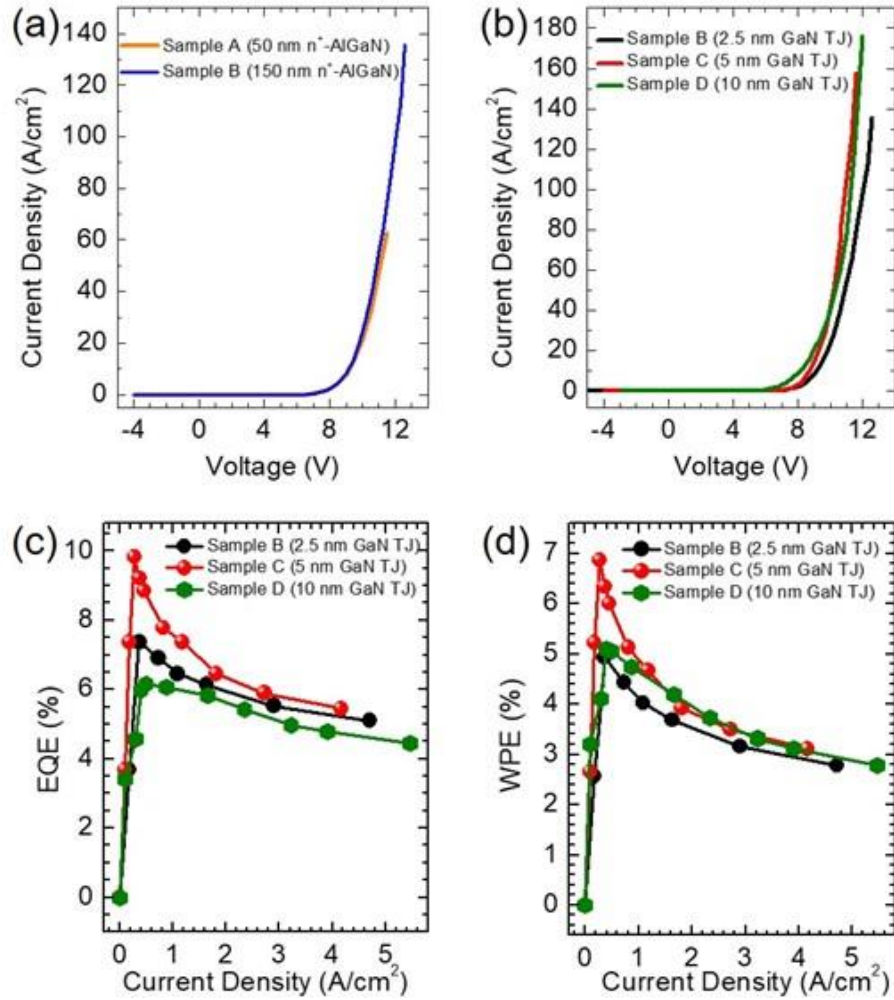


*Figure 5.3:(a) I-V characteristics of tunnel junction LED samples A and B, with 2.5 nm GaN layer width and different thicknesses, 50 nm and 150 nm respectively, of top $n^+$-AlGaN contact layer. (b) I-V characteristics of samples B, C and D grown with the same thickness of top $n^+$-AlGaN but different GaN layer widths of 2.5 nm, 5 nm and 10 nm, respectively. Variations of (c) EQE and (d) WPE with injected current density, for samples B, C and D.*

Measurements were performed using an AV-1010B pulse generator, with a 1% duty cycle and a 10 kHz repetition rate to minimize heating effect. A calibrated Newport 818-ST2-UV silicon photodetector with a Newport Model 1919-R power meter was used to measure the device output power. Shown in Fig. 5.3(a) are the current-voltage characteristics for samples A and B, which have a 2.5 nm thick GaN layer between the highly doped AlGaN layers, but with different

thicknesses of the top $n^+$-AlGaN contact layer. It is seen that the devices exhibit similar I-V characteristics under relatively low current densities. Higher current densities, however, can only be measured in Sample B, which has a thicker (~150 nm) top $n^+$-AlGaN contact layer. Slightly higher efficiency was also measured for Sample B, compared to Sample A. We have subsequently studied the effect of different thicknesses of the GaN layer within the tunnel junction on the device efficiency, while keeping the top $n^+$-AlGaN contact layer thickness at 150 nm. The GaN layer thicknesses were varied from 2.5 nm (Sample B), 5 nm (Sample C) to 10 nm (Sample D). I-V characteristics of these devices were measured and shown in Fig. 5.3(b). It is seen that Samples C and D have slightly better turn-on voltage, compared to Sample B. The small difference between the turn-on voltages of the different structures indicates that tunneling through the tunnel junction might be dominated by trap-assisted tunneling [238, 239]. Studies on AlGaN/GaN based double barrier resonant tunnel diodes have suggested that trapped charges at the hetero-interface are responsible for the observed electrical characteristics [240]. It has also been shown previously that a high concentration of impurity atoms at the tunnel junction interface can improve the turn-on voltage of the tunnel junction by providing states enabling trap-assisted tunneling [241-243]. The reduced turn-on voltage through trap-assisted tunneling improves the wall-plug efficiency of the tunnel junction LEDs by facilitating carrier transport even at low biases. The measured EQE and WPE are further shown in Fig. 5.3(c) and Fig. 5.3(d), respectively. A maximum EQE 9.8% was measured for Sample C, whereas maximum EQE 7.4% and 6.2% were measured for Samples B and D respectively, suggesting that a GaN layer thickness ~5 nm is optimum for the presented tunnel junction structures. This could be due to the degraded material quality with the incorporation of a thicker GaN layer, whereas a thinner GaN layer may not provide sufficiently strong polarization. Moreover, a thicker GaN layer also increases the absorption of UV light

emission from the device active region. A thick GaN layer would also present an obstacle to carrier transport due to the increased distance that electrons would need to tunnel across. A peak WPE of 6.9% was measured for Sample C, shown in Fig. 5.3(d).

It is interesting to note that all the devices showed a strong droop even at relatively low current injection of ~0.5-1 A/cm$^2$, suggesting that the cause of the droop is independent of the tunnel junction designs. Efficiency droop has been commonly measured for InGaN-based blue and green LEDs at current densities ~5-10 A/cm$^2$ [244, 245]. The underlying causes for the efficiency droop, including carrier delocalization, Shockley-Read-Hall (SRH) recombination, Auger recombination and also device heating, have been intensively studied [202, 245, 246]. At low current densities of ~1 A/cm$^2$, device heating and Auger recombination are not expected to be significant. As studied previously, the operation of GaN-based LEDs may deviate from low level injection conditions even under relatively low current densities, due to the asymmetric charge carrier transport [223, 247, 248]. Due to the large activation energy for Mg dopant in Al-rich AlGaN, p-type conduction is primarily mediated by hole hopping in the Mg impurity band at room temperature, which has low mobility [94, 180]. For Al-rich AlGaN the electron mobility is typically on the order of 20-50 cm$^2$·V$^{-1}$·s$^{-1}$ [185], whereas the hole mobility is ~1-5 cm$^2$·V$^{-1}$·s$^{-1}$ [49], or lower, while the corresponding maximum electron and hole concentrations are ~10$^{19}$ cm$^{-3}$ and ~10$^{17}$-10$^{18}$ cm$^{-3}$, respectively. The resulting conductivity of the n and p-AlGaN layers is nearly three orders of magnitude different. As a consequence, even at a small current density of 1 A/cm$^2$, the device operates in a regime that severely deviates from the low carrier injection condition. The resulting electric field in the p-AlGaN layer, even at a seemingly small current density, affects the transport of holes more severely than that of electrons, due to the large difference in their mobility values.

This leads to a significant increase in charge carrier recombination outside of the device active region, i.e., electron overflow to the p-AlGaN layer, at a small injection current. A similar effect has also been measured in AlGaN nanowire UV-C LEDs [247]. Further, it should also be noted that as the epitaxial growth of the entire LED structure was performed under slightly Ga-rich conditions, it is expected that the distribution of Ga may not be uniform in the epilayers [68, 222, 249, 250]. It has been shown that these Ga-rich regions act as highly efficient radiative recombination sites due to their ability to locally confine excitons. However, as the injected current into the device increases, carrier delocalization will occur allowing carriers to recombine at non-radiative recombination centers, also resulting in a decrease of device efficiency.

## 5.6 Characterization of Optimized Tunnel Junction Device

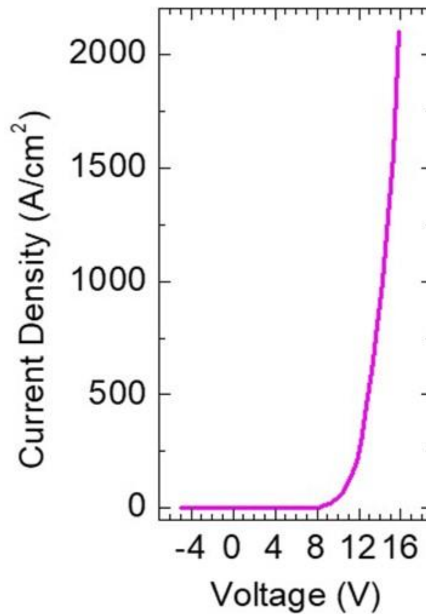


*Figure 5.4: I-V characteristics of an optimized tunnel junction LED from sample E with a GaN layer thickness of 5 nm and top $n^+$-AlGaN contact layer thickness ~480 nm.*

Based on the studies above, a 265 nm deep UV-LED structure with a 5 nm thick GaN layer in the p-AlGaN/GaN/n-AlGaN tunnel junction and ~480 nm thick top n-AlGaN contact layer (Sample E) was grown and fabricated. The measured current-voltage characteristics are shown in Fig. 5.4. A large current density of ~2,000 A/cm$^2$ was measured at 16 V, which is significantly better than that measured in Samples A-D as well as tunnel junction UV-C LEDs reported previously having emission at a similar wavelength [230, 236]. The high current density measured for this sample suggests that optimization of the p-AlGaN/GaN/n-AlGaN tunnel junction by adjusting the width of the GaN layer together with a relatively thick n-AlGaN top contact layer, can significantly enhance the current injection and stability of deep UV LEDs.

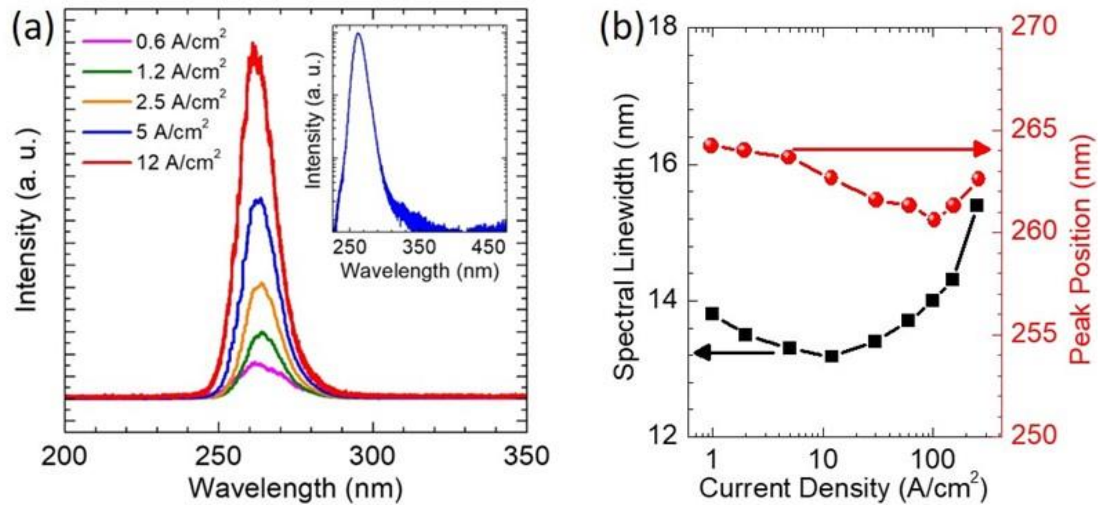


*Figure 5.5 (a) Electroluminescence spectra measured at different injection currents for a representative tunnel junction LED. The inset shows an electroluminescence spectrum measured at 25 A/cm$^2$ current density with the intensity in log scale. (b) Variations of peak position (red circles) and spectral linewidth (black squares) vs. injected current density.*

Shown in Fig. 5.5(a) are the electroluminescence spectra of an LED from Sample E measured at different current densities. The spectra were measured using CW bias supplied by a Keithley 2400 SMU, collected using an optical fiber coupled to a high-resolution spectrometer and

detected by a charge coupled device. Variations of the peak position and spectral linewidth with current density are shown in Fig. 5.5(b). It is seen that the device first exhibits a small blueshift from ~264 nm to ~260 nm with increasing current density, followed by a redshift at relatively high injection conditions. The blueshift can be explained by the quantum-confined Stark effect. The polarization field in AlGaN quantum wells is estimated to be ~370 kV/cm based on the shift experimentally observed, assuming that an injected current density of ~100 A/cm$^2$ completely flattens the bands in the quantum well, while not significantly affecting the emission wavelengths due to heating. This is substantially less than the predicted theoretical value of 1.5-2.5 MV/cm [26, 251], indicating the compensation of the sheet charge by impurities or defects, and some degree of relaxation in the AlGaN layers. The red shift at higher operating currents is likely due to heating effect. Such a red-shift has also been reported previously for both AlGaN [224] and InGaN [252] LEDs. The spectral linewidths stay nearly constant at ~13.5 nm at low current densities and broadens to ~15.5 nm at relatively high injection conditions. It is also noticed that no significant defect-related emission was measured in the UV-C LEDs, shown in the inset of Fig. 5.5(a).

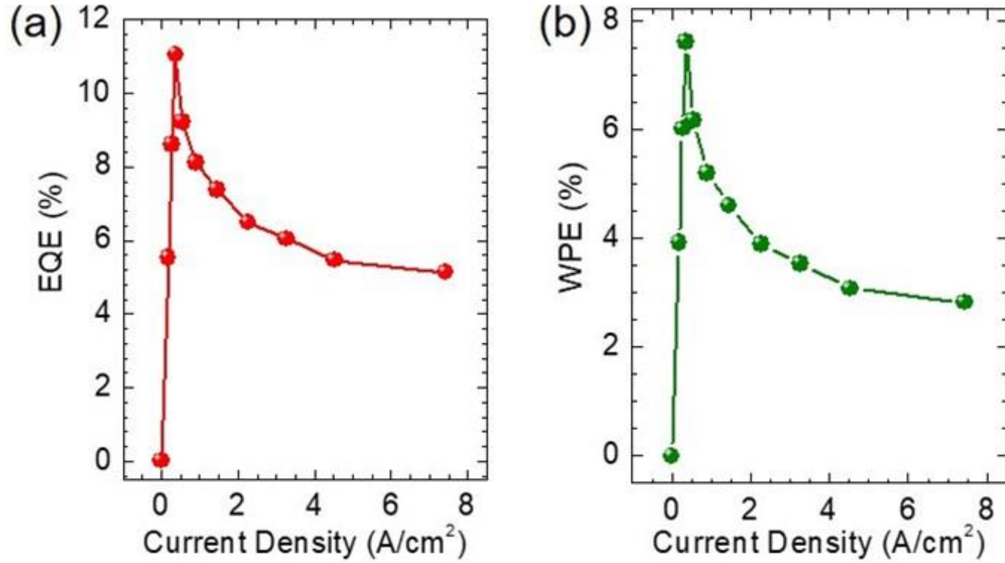


*Figure 5.6:(a) Variations of (b) EQE and (c) WPE with injected current density for an LED from sample E.*

The measured EQE and WPE of the LED from Sample E are shown in Figs. 5.6(a) and (b), respectively. A maximum EQE of 11% and WPE 7.6% was measured. The EQE measured here is higher than comparable UV LEDs having emission at this wavelength [152, 220-222, 230, 236], although still below the highest reported for LEDs at 275 nm [38], however the tunnel junction devices studied here have a higher WPE due to the more efficient carrier injection from such a structure, which also results in significantly lower turn-on voltages. It is also noticed that despite the optimization in the tunnel junction structure design, efficiency droop is present at low current injection. The external quantum efficiency of such a diode was fitted using the standard ABC model [253, 254]. From the fitted curve (not shown), A, B and C parameter values of $1.6 \times 10^7$ $s^{-1}$, $1.1 \times 10^{-9}$ $cm^3$ $s^{-1}$ and $7.4 \times 10^{-27}$ $cm^6$ $s^{-1}$ were derived. The estimated C value of $7.4 \times 10^{-27}$ $cm^6$ $s^{-1}$ is around three orders of magnitude higher than the previously reported Auger coefficient of $\sim 10^{-30}$ $cm^6$ $s^{-1}$ for AlGaN quantum well heterostructures [203], which, together with the presence of efficiency droop at very low current densities (~ 1 A/cm$^2$), strongly suggests that other carrier

loss mechanisms, such as electron overflow, other than Auger recombination is the main cause for the efficiency droop of deep UV LEDs [223, 247].

## 5.7 Summary

In summary, we have studied the design, epitaxy, fabrication and performance characteristics of p-AlGaN/GaN/n-AlGaN tunnel injected deep UV LEDs operating at ~265 nm. Significantly improved current-voltage characteristics and efficiency was measured with the incorporation of GaN layer thickness ~5 nm. The optimized AlGaN deep UV LED exhibited a maximum EQE and WPE of 11% and 7.6%, respectively. The device performance, however, suffers from efficiency droop even at relatively low current densities ~1 A/cm$^2$. The underlying cause is not likely due to Auger recombination, but instead could be related to electron overflow due to the small hole mobility associated with hole hopping conduction in the Mg impurity band of Al-rich AlGaN. To achieve high efficiency and high-power UV-C LEDs, it is therefore important to improve the hole mobility and p-type conduction of AlGaN by improving the epitaxy conditions, heterostructure design, and/or developing new p-type wide bandgap semiconductors.

# Chapter 6. An AlGaN Tunnel Junction Light Emitting Diode Operating at 255 nm

## 6.1 Author Contribution and Copyright Disclaimer

The contents of this chapter were published in the journal Applied Physics Letters in December 2020 [103], for which I retain the right to include it in this thesis/dissertation, provided it is not published commercially. The co-authors were Jiseok Gim, Robert Hovden and Zetian Mi from the University of Michigan. I designed, conducted and authored most of the work. J.G. and R. H. collected the HAADF-STEM images presented. The work was supervised by Z. M., who contributed to the design of the experiments. This work was supported by the Blue Sky research program in the College of Engineering at the University of Michigan and National Science Foundation (Grant DMR-1807984). The temperature-dependent measurements were performed in a cryostat which Prof. Elaheh Ahmadi from the Electrical Engineering and Computer Science Department allowed us to use.

## 6.2 Overview

Light within the UV-C wavelength range (< 280 nm) inactivates pathogens and can be used for the prevention of spoilage of food [255] as well as for healthcare applications [256]. Such critical applications have taken on an even more pressing need as UV-C light can effectively contain the spread of infectious diseases, making it a vital tool against the next global pandemic. Currently mercury and xenon lamps are primarily used for these applications. AlGaN based deep UV optoelectronic devices, however, are revolutionizing the industry, enabling much broader

applications due to the absence of toxic materials, tunable emission wavelengths, significantly reduced power consumption, and relative ease of installation and use. To date, emission in the 260-280 nm range is commonly used for this purpose. Recent work has shown that emission at even shorter wavelengths (higher energies), from 255 nm to 220 nm, can be more effective at sterilization [257], while the reduced photon penetration depth in skin can avoid the deleterious effects of human exposure to UV light [258]. At present, EQE over 20% has been measured for UV LEDs with emission at 275 nm [38], and ~10% for LEDs at ~265 nm [104]. For LEDs emitting at ~255 nm, EQE in the range of 1-3% has been commonly reported [216, 259-262]. With proper device packaging, the highest reported EQE is only around 4.5% [76], with very limited WPE, less than 4%, primarily due to the difficulty in p-type doping and the resulting of poor hole transport [51, 156]. III-nitrides have highly asymmetric doping [263]: the hole mobilities and concentrations of AlGaN are typically over one to several orders of magnitude lower than those for electrons [54, 94]. The vast imbalance in the electron and hole injection to the active region has several detrimental impacts on device performance, including significantly reduced carrier injection efficiency, severe electron overflow, and parasitic recombination outside the active region [223, 247, 248]. Recent studies further suggests that electron overflow, among other factors such as Joule heating [227], Auger recombination [201, 203, 264-266] and carrier delocalization [267, 268], is a primary cause for the efficiency droop observed in UV LEDs [226, 247].

Tunnel junction structures [99, 101, 104, 230, 236, 269-271] have been investigated as an alternative to resistive p-AlGaN contact layers and absorptive p-GaN contact layers [228] in UV LEDs. The reduced resistivity of the n-AlGaN contact layer helps to increase carrier injection to the active region and improve current spreading, leading to UV-C LEDs operating at 265 nm with

EQE >10% [104]. Previous work has investigated the critical effect of the thickness of the tunnel junction [104, 236] and doping of the p-AlGaN layers on device characteristics [100]. Earlier studies on nitride tunnel junction structures have also shown that the transport of carriers across the tunnel junction is primarily determined by trap-assisted tunneling [238, 242, 243, 272], indicating the crucial role of incorporating defects around tunnel junction to maximize hole injection. To date, however, there have been no demonstrations of tunnel junction UV LEDs operating at wavelengths below 260 nm with an EQE of more than 0.1% [230, 269, 271]. MBE offers distinct advantages over MOCVD for the growth of tunnel junction deep UV LEDs, due to the much more efficient incorporation of Mg-dopant incorporation in wide bandgap AlGaN [94, 108, 273]. Moreover, by varying the growth conditions, nanoscale clusters can be formed in Al-rich AlGaN [67-70, 110, 249], which can provide strong carrier confinement and therefore effectively reduce nonradiative recombination as well as quantum-confined Stark effect (QCSE) [68, 249, 274], resulting in high efficiency deep UV emission.

In this chapter, we report on a detailed study of the epitaxy and performance characteristics of tunnel junction AlGaN deep UV LEDs operating at ~255 nm. The device heterostructure was grown under slightly Ga-rich conditions by MBE to promote the formation of nanoscale clusters in the active region [69, 275-277]. The device exhibits highly stable emission at ~255 nm, with virtually no change in the peak emission for injection current density up to 200 A/cm$^2$, which is attributed to the radiative emission originating from highly localized carriers in Ga-rich regions formed in the active region. With the incorporation of an AlGaN/GaN tunnel junction, we have demonstrated 255 nm deep UV LEDs with a maximum EQE of 7.2% and WPE of 4%, which are nearly one to two orders of magnitude higher than those reported previously for tunnel junction

LEDs operating at this wavelength [230, 269, 270]. Detailed temperature-dependent measurements further suggest several critical factors that limit the device performance, including charge carrier (hole) transport, electron overflow, and Joule heating. This work provides a promising path for achieving high efficiency far UV-C LEDs that were previously challenging.

### 6.3 Device Structure Epitaxy and Structural Characterization

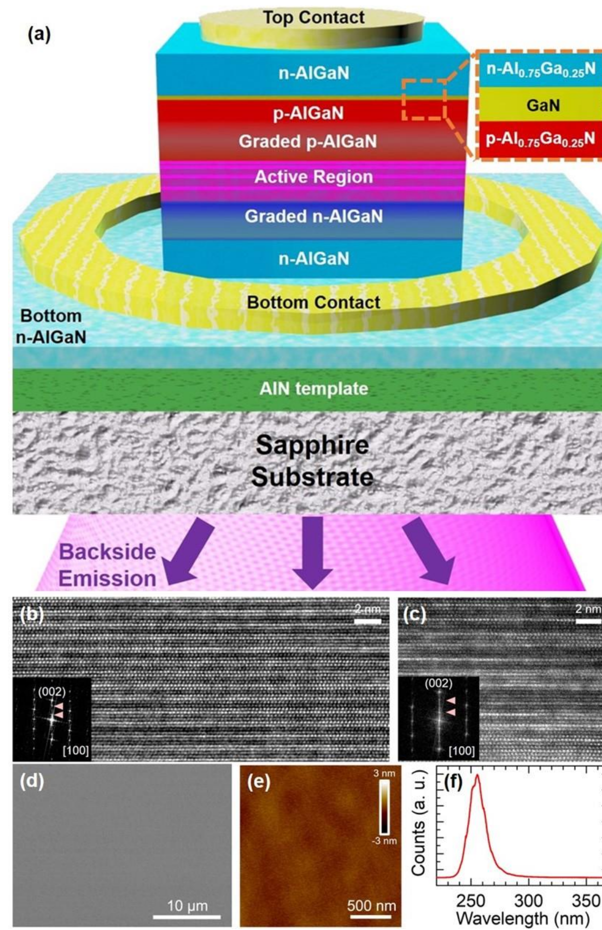


*Figure 6.1:(a) Schematic tunnel junction deep UV LED. The tunnel junction is shown in the marked region. (b, c) Atomic scale HAADF-STEM images of an $Al_{0.75}Ga_{0.25}N$ layer showing the presence of nanoscale Ga-rich layers due to compositional variation. The brighter regions correspond to higher Ga content. FFT shows the superlattice peak (red arrows) associated with atomic ordering in wurtzite AlGaN along c-plane direction. (d) SEM image of the sample surface after epitaxial growth showing a smooth surface over a wide area. (e) High-resolution AFM scan of the sample surface after epitaxial growth. (f) Photoluminescence spectrum of the sample measured using a 193 nm laser for excitation at room temperature.*

Shown in Fig. 6.1(a) is the schematic of the AlGaN tunnel junction deep UV LED, which was grown using a Veeco Gen930 MBE system equipped with a radio frequency plasma-assisted nitrogen source. The device heterostructures were grown on AlN-on-sapphire templates from DOWA Holdings Co. Ltd. A nitrogen flow rate of 0.6 sccm and an RF power of 350 W were used throughout the growth, resulting in a growth rate of 160 nm/hr. First, a 500 nm thick bottom n-$Al_{0.75}Ga_{0.25}N$ contact layer was grown with a Si atom concentration ~$3 \times 10^{19}$ $cm^{-3}$. During this growth, several steps of *in situ* annealing at elevated temperatures were performed, which can significantly improve the structural and optical properties as shown by recent studies [71, 73, 74]. The n-AlGaN was then graded up from 75% Al composition to 90% over ~25 nm. Subsequently, the active region was grown, which consists of four AlGaN QWs emitting at 255 nm, with the barrier width decreasing from 6 nm to 3.5 nm. Simulations have shown that the reduced barrier thickness closer to the p-doped side of LEDs can help improve device performance by increasing hole injection into the quantum wells, thereby leading to more even charge carrier distribution in the active region [278, 279]. Following the active region, a p-doped AlGaN EBL was grown, with Al composition graded down from 90% to 75% over 20 nm. The graded down AlGaN layer results in an enhanced p-type doping due to the strong spontaneous and piezoelectric polarization of AlGaN [21], which can maximize the injection of holes. Prior to the tunnel junction, a 25 nm highly doped p-$Al_{0.75}Ga_{0.25}N$ layer was grown, followed by a 5 nm GaN layer. The Mg atom concentration in the p-doped layers is estimated to be ~$5 \times 10^{19}$ $cm^{-3}$. Finally, a 150 nm thick heavily doped n-$Al_{0.75}Ga_{0.25}N$ top contact layer was grown, with an annealing step included after the first 100 nm of growth. The incorporation of a thin GaN layer sandwiched between the p-AlGaN and n-AlGaN top contact layers can significantly reduce the depletion width and enhance

tunneling probability by taking advantage of the large polarization charges generated at the interfaces [102, 280]. The growth was carried out under slightly Ga-rich conditions, which has been previously shown to enhance dopant incorporation [54, 70, 94] and increase the internal quantum efficiency of AlGaN heterostructures [68, 69, 249]. The enhanced luminescence efficiency using this technique has been suggested to be a consequence of compositional inhomogeneities present within the AlGaN [249]. Atomic-resolution HAADF-STEM shows the ordering of Ga-rich atomic layers in the $Al_{0.75}Ga_{0.25}N$ layer; it indicates the presence of compositional non-uniformity within the layer and is consistent with previous reports [196, 249] (Fig. 6.1 b, c). Low frequency background was removed to reduce contrast loss to thickness variation. Fast Fourier transform (FFT) patterns of the HAADF-STEM images exhibit ordering of Ga-rich layer along [001] direction; the peaks are forbidden in electron diffraction pattern of wurtzite hexagonal symmetry. HAADF-STEM was collected using a Cs aberration-corrected JEOL 3100R05 microscope (300 keV, 22 mrad) with a detector angle from 74 to 200 mrad. While the Ga-rich growth conditions have distinct advantages, prolonged growth in this regime can lead to the formation of crystalline defects due to the presence of gallium droplets on the sample surface. To eliminate the excess Ga at the growth interface, the aforementioned annealing steps were incorporated within the growth, wherein the sample temperature was raised by 50 ˚C above the growth temperature, while keeping the plasma and source shutters closed. The RHEED screen was monitored to ensure that the dim, streaky RHEED pattern during growth gave way to a brighter, streaky pattern which signifies the desorption of excess metal at the growth interface [275, 281]. A SEM image of the sample surface after cleaning following epitaxial growth is shown in Fig. 6.1(d). The SEM does not show the presence of any droplets or defects on the sample surface even over large regions, showing the advantages of the annealing process. A high-

resolution AFM scan of the surface is shown in Fig. 6.1(e), depicting a very smooth surface with RMS roughness below 0.5 nm. The PL of the sample measured using a 193 nm ArF excimer laser, shown in Fig. 6.1(f), displays an emission with peak at 255 nm. The full-width half maximum is around 20 nm, which is a result of emission not only from the active region, but also from the graded layers surrounding the active region, as well as luminescence from the Mg-acceptor related transitions in the p-doped layers.

## 6.4 LED Fabrication and Characterization

The devices were fabricated using standard photolithography, etching, and contact metallization techniques. First, argon ion beam milling was used to define the device mesas, with area 30 μm × 30 μm. The regions surrounding the devices were etched down to the bottom n-AlGaN layer. This was followed by the deposition of a 300 nm thick $SiO_2$ passivation layer. Vias were then etched into the $SiO_2$ to allow for the deposition of Ti/Al/Ni/Au contacts to the top and bottom n-AlGaN layers. The contacts were then annealed at 700 ˚C in a nitrogen ambient for 30 seconds. Finally, a thick reflective Al/Au contact pad was deposited over the devices to maximize light reflection towards the backside of the substrate, where a detector was placed for power measurements.

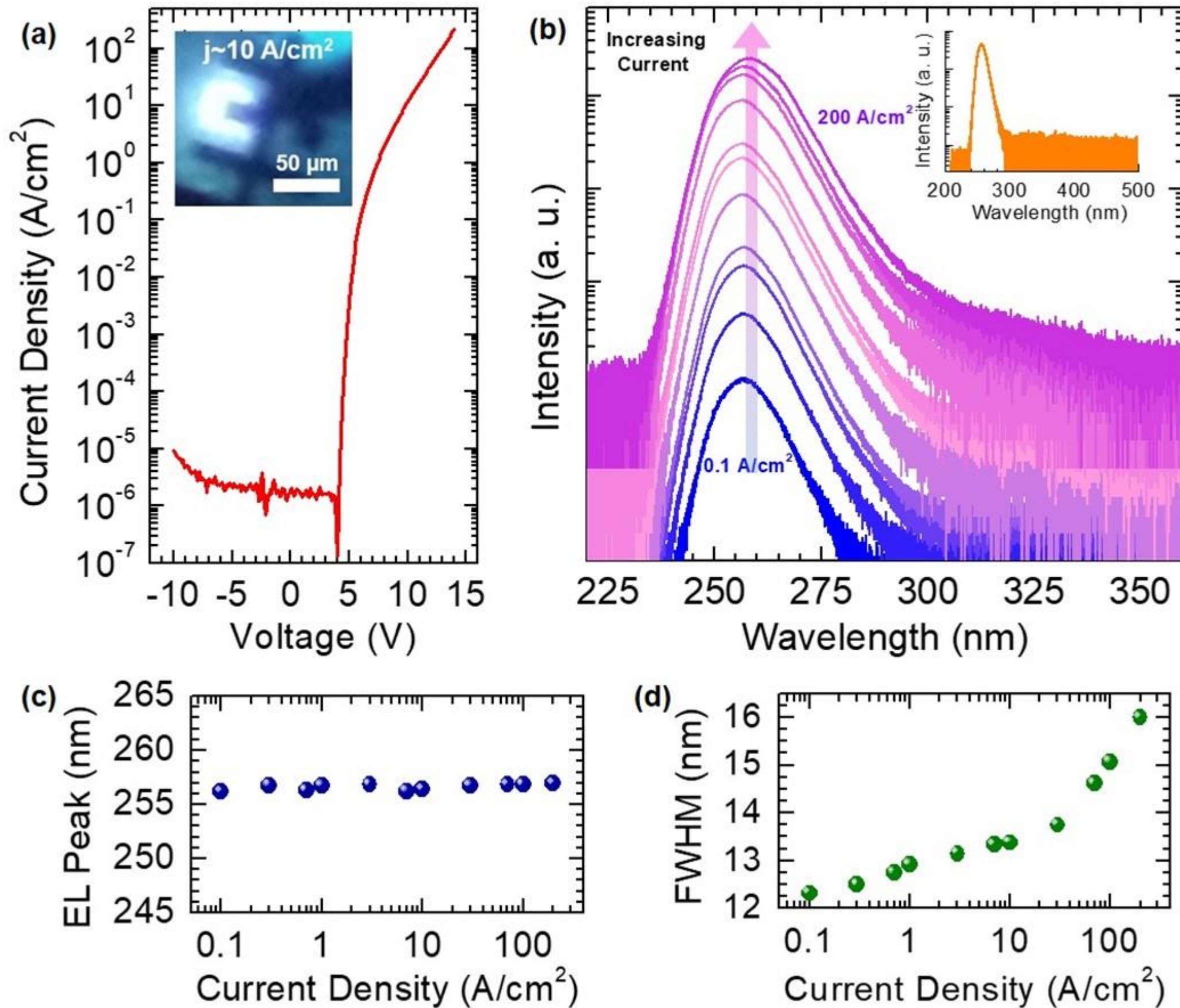


*Figure 6.2:(a) J-V characteristic of the tunnel junction deep UV LED. The inset shows an LED under a CW bias injection current of ~10 A/cm$^2$. (b) RT EL spectra measured at different injection currents. Inset: EL spectrum at an injection current of 10 A/cm$^2$ measured from 200 nm to 500 nm, showing the absence of defect-related emission. (c) Plot of the peak positions of the EL spectra at different injected current densities. (d) Variation of the FWHM extracted from the EL spectra recorded at different injected current densities.*

The devices were first measured in continuous-wave (CW) operation conditions using a Keithley 2400 SMU. The J-V characteristics of a representative device are shown in Fig. 6.2(a). The device exhibits a sharp turn-on voltage, with negligible reverse leakage current. It is noticed that the device has much improved current rectification, compared to previously reported tunnel junction devices emitting at similar wavelengths [230], due to the reduced leakage current in the

present devices. An image of a device operating at a current density of ~10 A/cm$^2$ is shown in the inset, demonstrating extremely bright luminescence. The electroluminescence from the device was collected using an optical fiber and analyzed through a spectrometer. The electroluminescence emission spectra measured at different injection currents are shown in Fig. 6.2(b). The inset is a scan over a wider range, confirming the absence of any defect-related emission at longer wavelengths that were often observed in previous studies [269, 271]. The position of the electroluminescence peak is plotted against injection current in Fig. 6.2(c), showing that the emission peak position is highly stable with virtually no variation for injected current densities up to 200 A/cm$^2$, which is in direct contrast to the expected peak variation due to QCSE in AlGaN quantum wells. This can be explained by the strong charge carrier confinement in the Ga-rich nanoclusters in AlGaN quantum wells grown under slightly Ga-rich conditions by MBE. From Fig. 6.2(d), an increase in the FWHM is seen with increasing injection current. While the increase in FWHM is gradual up to ~10 A/cm$^2$, at higher current injection the FWHM starts to rapidly increase. This broadening of the linewidth occurs primarily on the longer wavelength side of the emission peak, which can be explained by luminescence from recombination of carriers within the graded p-doped region of the device.

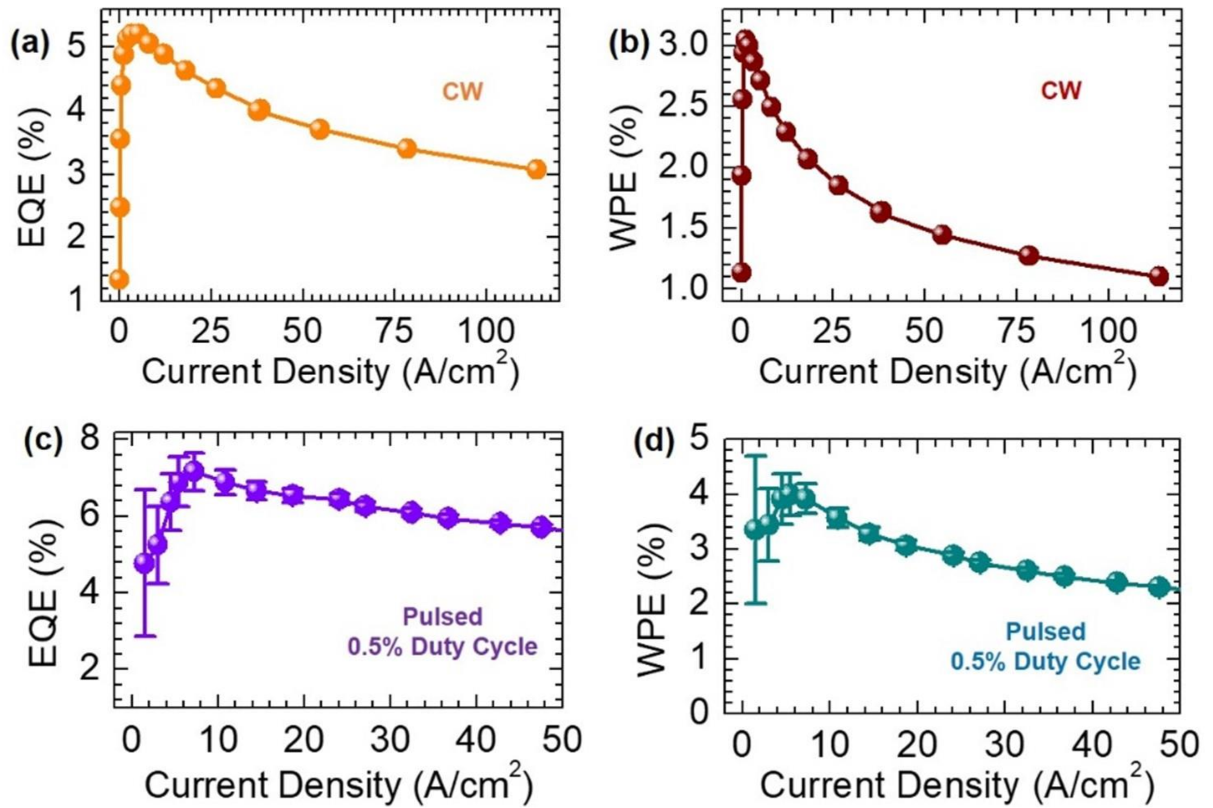


*Figure 6.3:(a) EQE and (b) WPE of the tunnel junction deep UV LED vs. current density measured under CW bias at room temperature. (c) EQE and (d) WPE of the tunnel junction deep UV LED measured using pulsed bias with a 0.5% duty cycle. Error bars are provided.*

To determine the efficiency of the device, the emitted light from the back of the sample was collected with a Newport 818-ST2-UV photodetector with a calibrated Newport Model 1919-R power meter, while the devices were probed using CW bias. As the light was only collected from the back side of the substrate, there are some losses from emission on the top and sides of the devices which were not included. Figures 6.3(a) and (b) show the variation of EQE and WPE, respectively, with injected current density. The maximum EQE and WPE measured are 5.2% and 3%, respectively. These values are nearly one to two orders of magnitude higher than previously reported tunnel junction devices operating at such short wavelengths [230]. The light extraction

from the presented devices can be increased with proper packaging, which will further improve the efficiency.

It is also noticed that the device exhibits severe efficiency droop with further increasing current. As the samples were fabricated on sapphire substrates, heating is expected to be an issue. To mitigate the heating effect, the device efficiencies were measured under pulsed conditions, shown in Fig. 6.3(c) and (d). An AV-1010B pulse generator was used to bias the samples with a 0.5% duty cycle. A peak EQE of 7.2% and WPE of 4% were measured, respectively. Despite the improved efficiency with reduced heating effect, the onset of efficiency droop is measured at a similar level of injection current as that under CW biasing conditions, suggesting that Joule heating may not be the primary cause for the efficiency droop. Recent studies have suggested that the primary cause for efficiency droop of deep UV LEDs is directly related to electron overflow [223, 247, 248, 282]. In this study, it is observed that there is a direct correlation between the onset current density of efficiency droop with the rapid broadening of the FWHM, shown in Fig. 6.2(d), because of luminescence from recombination of overflowed electrons within the p-doped regions of the device. This observation is consistent with the hypothesis that the overflow of electrons from the active region is the primary cause of the efficiency droop, due to the highly asymmetric electron and hole transport of AlGaN.

## 6.5 Role of Temperature on LED Performance

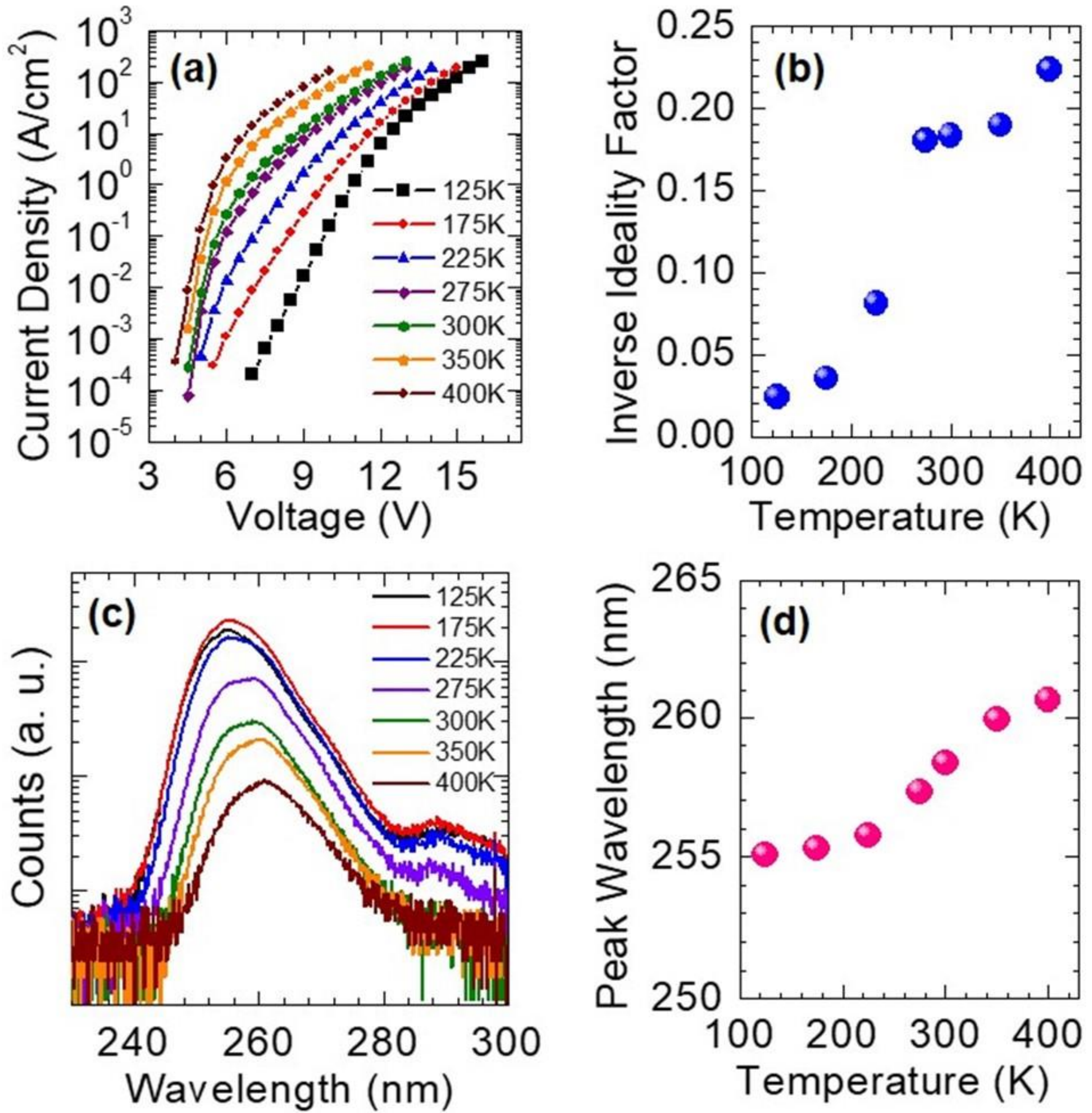


*Figure 6.4:(a) J-V characteristics at different temperatures for a tunnel junction deep UV LED. (b) Inverse of the ideality factor extracted from the J-V curves plotted against temperature. (c) EL spectra for a device at different temperatures, under the same injection current. (d) Variation of the peak emission wavelength with temperature.*

The device performance, including the J-V and EL emission, was further measured in the temperature range of 100 to 400 K under CW biasing conditions. Shown in Fig. 6.4(a) are the

current-voltage characteristics measured at different temperatures. The measured current at similar bias shows a significant increase with temperature. The device remains operational even at low temperatures, despite the high Mg acceptor ionization energy, which can be explained by the involvement of tunneling transport of holes in the depletion region [49, 94, 273, 283]. Recent studies suggest that the characteristic tunneling energy for hole transport is directly related to the Mg acceptor activation energy of Al(Ga)N and can be significantly reduced with enhanced Mg dopant incorporation, due to the Mg acceptor level dispersion at very high doping concentrations [54, 273]. At room temperature, the ideality factor is derived to be ~5.8, which is comparable to other III-nitride LEDs [283-285], in spite of the large bandgap and the presence of a tunnel junction. The inverse of the ideality factor is plotted against temperature in Fig. 6.4(b). A continuous decrease in the ideality factor is measured for the device as temperature is increased, which can be explained by the growing dominance of diffusion current in the depletion region with increasing temperature, due to the more efficient hole current injection. The electroluminescence spectra were also measured at different temperatures at a similar current density around 50 A/cm$^2$, shown in Fig. 6.4(c). The peak position is plotted in Fig. 6.4(d), and an expected blue shift is observed with decreasing temperature. The S-shaped temperature dependence of the curve is consistent with the presence of significant alloy disorder and nanoclusters [286, 287] as a result of the Ga-rich nanoclusters present in the active region (Fig. 6.1(b)). A small peak at ~290 nm is also observed. This can be explained by the increased internal quantum efficiency at low temperatures of the luminescence from overflowed carriers recombining within the p-doped region. At higher temperatures, this peak is too weak to detect. This observation confirms that the UV LEDs have severe electron overflow. Moreover, a sharp decrease in electroluminescence intensity was observed in the range of 225 K to 400 K, which illustrates the significance of carrier delocalization

and thermal effects in inhibiting efficient radiative recombination. The decrease in electroluminescence at temperatures above room temperature exemplifies the importance in conducting heat away from the active region when devices are operated at high current densities for high-power applications.

## 6.6 Summary

In conclusion, we have demonstrated high performance tunnel junction deep UV LEDs by using plasma-assisted MBE. The device operates at ~255 nm with a maximum EQE of 7.2% and WPE of 4%, which are nearly one to two orders of magnitude higher than previously reported tunnel junction devices operating at this wavelength [230, 269]. The devices exhibit highly stable emission, with nearly constant emission peak with increasing current, due to the strong charge carrier confinement related to the presence of Ga-rich nanoclusters. However, the device suffered from efficiency droop at relatively low current densities. Detailed temperature-dependent measurements suggest that the presence of severe efficiency droop of deep UV LEDs is largely due to electron overflow. Furthermore, temperature-dependent measurements have shown the impact of thermal effects on the electrical and emission properties of the device. The device performance can be further improved with proper packaging and thermal management.

# Chapter 7. Electron Overflow of AlGaN Deep Ultraviolet Light Emitting Diodes

## 7.1 Author Contribution and Copyright Disclaimer

At the time of writing, the work in this chapter is part of a manuscript that has been accepted for publication by the journal Applied Physics Letters in June 2021 (DOI: 10.1063/5.0055326). I retain the right to include it in this thesis/dissertation, provided it is not published commercially. The co-authors were Jiseok Gim, Robert Hovden and Zetian Mi from the University of Michigan. I designed, conducted and authored most of the work. J. G. and R. H. collected the HAADF-STEM images presented. The work was supervised by Z. M., who contributed to the design of the experiments. This work was supported by the Blue Sky research program in the College of Engineering at the University of Michigan and National Science Foundation (Grant DMR-1807984).

## 7.2 Introduction

UV-C semiconductor LEDs are gaining much attention due to their ability to kill pathogens, which is essential for water purification, food preservation, and surface sterilization [255, 256]. Their ease of use, small size, and low power requirements, compared to conventional mercury and xenon lamps, will enable much broader and widespread application in combating, or even possibly preventing another global pandemic. While conventional UV-C devices have been focused on 260-270 nm wavelength range [256], recent studies suggested that even shorter wavelengths, i.e., ~200-220 nm in the far UV-C, are not only more effective at sterilization but can significantly limit the

dangers of human exposure to UV radiation due to the shorter penetration depth of higher energy photons in skin [288]. To date, however, such devices exhibit extremely low efficiency, due to the low IQE, insufficient light extraction, and the difficulty in p-doping of ultrawide bandgap AlGaN materials [289-291]. In this regard, tunnel junction-based devices have garnered significant attention, offering a route that can alleviate some of the critical issues associated with the low hole injection by providing a conductive, transparent n-doped layer for enhanced carrier (hole) injection, current spreading, and light extraction [99, 100, 104, 230, 236, 270, 292]. Large electric fields within the tunnel junction layer can be created through polarization engineering, enabling relatively narrow depletion widths despite the wide bandgap AlGaN materials [25, 26, 99, 100, 102-104, 230, 236, 270, 271]. To realize far UV-C LEDs, however, the Al composition of AlGaN needs to tuned to be >75%, which causes serious issues for p-type as well as n-type doping [52, 293, 294]. These factors not only drastically reduce the probability of the inter-band tunneling of charge carriers across the tunnel junction but also lead to extremely poor charge carrier (particularly hole) injection. Consequently, the best reported EQE values is well below 0.1% for AlGaN tunnel junction LEDs operating below 250 nm [270, 292].

Recently, significant advances have been made in the MBE of AlGaN and their device applications. With the use of MBE, relatively efficient p-type conduction of Al-rich AlGaN has been achieved through *in situ* surface Fermi level control under slightly Ga-rich epitaxy conditions [49, 94]. This growth process also leads to the formation of Ga-rich clusters in AlGaN layers [68-70, 103, 143, 196, 249], which provide highly localized sites for efficient radiative recombination, thereby overcoming the efficiency limitation placed by dislocations [40]. To date, however, there are few studies of tunnel junction AlGaN deep UV LEDs towards far UV-C emission [269].

Moreover, the currently reported tunnel junction AlGaN deep UV LEDs generally display a pronounced efficiency droop, even for operation at very low current densities, which limits their high-power applications. Efficiency droop is a well-studied phenomenon in InGaN-based optoelectronic devices, with the underlying causes including Auger recombination [201, 203, 264-266], electron overflow [226, 247, 295], defect-related mechanisms, carrier delocalization [267, 268], and a combination of these factors [282]. However, the underlying cause for the severe efficiency droop of AlGaN deep UV LEDs has remained largely unexplored.

In this chapter, we report on a detailed study of the design, epitaxy, and performance characteristics of AlGaN tunnel junction deep UV LEDs. By incorporating a Mg-doped, polarization engineered electron blocking layer, a maximum external quantum efficiency and wall-plug efficiency of 0.35% and 0.21%, respectively, were measured for devices operating at ~245 nm, which are over one order of magnitude higher than previously reported tunnel junction devices at this wavelength [270, 292]. Severe efficiency droop, however, was measured at very low current densities (~0.25 A/cm$^2$), which, together with the transverse magnetic (TM) polarized emission, are identified to be the primary limiting factors for the performance of AlGaN deep UV LEDs. Detailed electrical and optical analysis further suggests that the observed efficiency droop is largely due to an electrical effect, instead of an optical phenomenon. This study provides new insights on how to further improve the efficiency of UV-C and far UV-C LEDs that are relevant for a broad range of applications including water and air purification and sterilization.

## 7.3 Tunnel Junction UV LEDs Structure and Growth

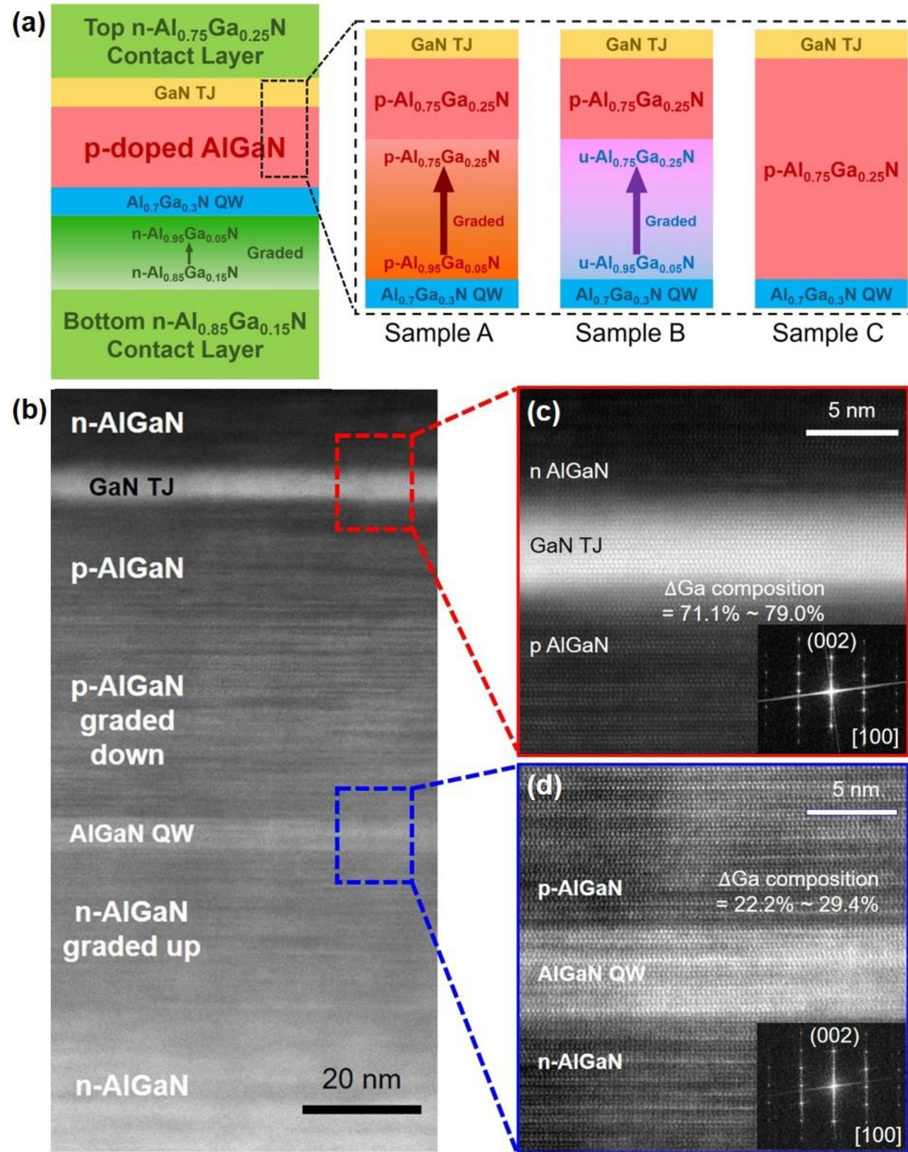


*Figure 7.1: (a) Schematic of the different tunnel junction UV LED device structures fabricated. (b) HAADF-STEM image of the complete device structure of Sample A. (c) Atomic-scale HAADF-STEM image of the tunnel junction region. FFT shows the superlattice peak associated with atomic ordering in wurtzite Al(Ga)N along c-plane direction. (d) Atomic-scale HAADF-STEM image of the active region. FFT shows the superlattice peak associated with atomic ordering in wurtzite AlGaN along c-plane direction.*

AlGaN LED heterostructures were grown on commercial AlN-on-sapphire substrates using a Veeco Gen 930 plasma-assisted MBE system. The epitaxy was performed under slightly

Ga-rich conditions at a substrate temperature ~750 ˚C. Three different tunnel junction LED designs, samples A-C, schematically shown in Fig. 7.1(a), were studied. All the structures consist of an initial bottom n-AlGaN contact layer with a thickness of 500 nm. Immediately preceding the active region, the Al composition of the n-AlGaN layer was graded up from ~85% to ~95%. The active region consisted of a single 6 nm thick AlGaN quantum well emitting at ~245 nm. The use of a single quantum well minimizes the issue of non-uniform carrier injection in the quantum well active region. To pinpoint the effect of electron overflow, the design of the p-doped region was varied between samples A-C. Sample A included a 25 nm Mg-doped AlGaN electron blocking layer immediately following the active region, which was graded from an Al composition ~95% to ~75%. Sample B is identical to sample A, except the AlGaN electron blocking layer is undoped, relying solely on polarization-induced doping for generation of charge carriers (holes)[100]. Previous studies have shown that the scheme of compositional grading can enhance the effective p-type doping of AlGaN layers [21, 280]. Sample C is identical to sample A except that the compositionally graded AlGaN:Mg electron blocking layer is replaced with a uniform $Al_{0.75}Ga_{0.25}N$:Mg layer of the same thickness. Following the AlGaN electron blocking layer, a 25 nm thick p-$Al_{0.75}Ga_{0.25}N$ layer was grown for all three samples. Subsequently, a 5 nm thick GaN layer was grown over the p-doped layer, followed by an n-doped $Al_{0.75}Ga_{0.25}N$ layer, collectively forming the tunnel junction. The thickness of the n-$Al_{0.75}Ga_{0.25}N$ layer is 150 nm to allow adequate current spreading.

Structural properties of Sample A were studied by using a JEOL 3100R05 microscope with Cs aberration corrected STEM (300 keV, 22 mrad) and a ADF detector with 120 mm camera lengths and a detector angle of 59 (inner) – 354 mrad (outer). The high-angle annular dark-field

scanning transmission electron microscopy (HAADF-STEM) confirms the cross-sectional device heterostructure for Sample A (Fig. 7.1(b)). Atomic-resolution cross-sectional STEM in Fig. 7.1(c) reveals the GaN layer (~5 nm) epitaxially grown between the top $n^+$-AlGaN and p-AlGaN layer. The ratio of HAADF STEM intensity estimates ~75.0% ± 4.0% less Ga in the p-AlGaN layers compared with the Ga concentration in the GaN layer. Figure 7.1(d) also shows the epitaxial growth of AlGaN quantum well (~6 nm) with ~25.8% ± 3.6% higher content of Ga relative to adjacent AlGaN barriers in the graded active region. The brighter atomic layers in the active region corresponding to the Ga-rich layers reveals significant compositional non-uniformity in the epilayers due to the use of slight metal-rich epitaxy conditions. Fast Fourier transform (FFT) patterns of the HAADF-STEM images also exhibit ordering of Ga-rich layer along [001] direction, which are forbidden in electron diffraction pattern of wurtzite hexagonal symmetry. The formation of extensive nanoscale AlGaN clusters can provide three-dimensional quantum-confinement of charge carriers, which was shown to dominate the EL of MBE-grown AlGaN UV LEDs[103] and is the principle mechanism for the enhanced internal quantum efficiency for AlGaN grown by PA-MBE[70, 144, 249, 296, 297].

## 7.4 LED Fabrication and Comparison

For the UV LED fabrication, firstly ion milling was used to etch down to the bottom n-AlGaN layer to make the device mesas. 300 nm of $SiO_2$ was then deposited using PECVD for insulation. Reactive ion etching, with high selectivity between AlGaN of $SiO_2$ , was used to etch vias in the insulation layer for the deposition of metal contacts. A Ti/Al/Ni/Au metal stack was deposited onto the exposed top and bottom n-AlGaN for the device contacts. Annealing of the

contacts was performed in a nitrogen ambient at 700 ˚C for 30 seconds. Al/Au metal contact pads were deposited over the annealed device contacts for probing.

The electrical properties of the devices were measured under continuous-wave (CW) biasing conditions using a Keithley 2400 SMU. The J-V characteristics of representative devices are shown in Fig. 7.2(a). Sample B, which relies solely on polarization doping, is observed to be leaky, while samples A and C show excellent rectifying characteristics. This indicates that a proper p-n junction was not formed in sample B. Sample A exhibits a higher turn-on voltage as compared to sample C; however the turn-on is significantly sharper for sample A. High electron overflow can result in an earlier, but more gradual turn-on voltage for LEDs, indicating that electron overflow is better controlled in sample A, due to the polarization engineered electron blocking layer [100]. Samples A and C show very similar characteristics at high forward bias, indicating that they have similar device resistances. The ideality factor calculated for samples A-C are 7.74, 18.15 and 12.48, respectively. The relatively high ideality factors is a consequence of the presence of a tunnel junction in the devices, as well as the hole transport being dominated by tunneling within an impurity band [48, 94, 298]. However, since all three devices have identical tunnel junction design, the significant differences in the measured ideality factors may be a result of other factors. Higher ideality factors have been associated with insufficient doping, higher layer resistances and increased electron overflow [283, 299]. From these measurements we conclude that the polarization-engineered AlGaN:Mg electron blocking layer plays a crucial role in charge carrier transport, and its presence is beneficial to improved current-voltage characteristics.

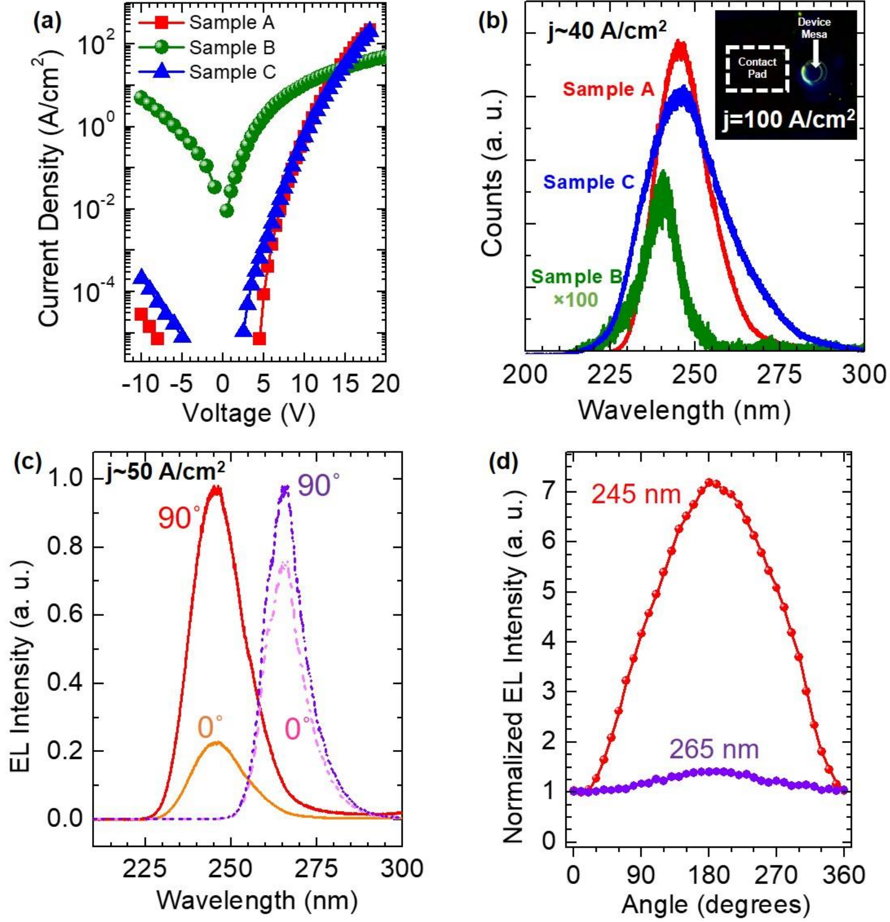


*Figure 7.2: (a) J-V characteristics of the different tunnel junction UV LED device structures. (b) Room-temperature electroluminescence spectra measured for the different devices under current injection densities ~40 A/cm$^2$. The electroluminescence of sample B has been magnified by a factor of 100. The inset shows a device from sample A under an injection current of ~100 A/cm$^2$. (c) Electroluminescence spectra measured at polarization angles of 0˚ and 90˚ for sample A (245 nm), shown as straight lines, and an identical device with emission at 265 nm, shown as dashed lines. (d) Variation of electroluminescence intensity with polarization angle measured for sample A (245 nm) in red, and an identical device with emission at 265 nm, in purple.*

We further measured the EL spectra, shown in Fig. 7.2(b), under similar current injections around 40 A/cm$^2$ for all three samples. The peak of the EL spectrum is measured at ~245 nm for all the samples. Samples A and C exhibit relatively bright luminescence, however the luminescence from Sample B is significantly weaker. The full-width half maximum (FWHM) is measured to be ~15 nm for sample A, which is comparable to previously reported LEDs grown by

MBE [99, 103, 104, 230]. Sample B has a similar FWHM, although it also exhibits a shoulder at shorter wavelengths close to 235 nm, suggesting that there is significant recombination of charge carriers within the higher Al content layers of the device. Sample C has a significantly broader emission peak with FWHM over 25 nm. The wide emission peak is a strong indication of more severe electron overflow in this device. Further, sample C also shows a relatively long tail as compared to the other devices, which can be explained by emission from the Mg acceptor related transition of the p-doped $Al_{0.75}Ga_{0.25}N$ [94]. The inset of Fig. 7.2(b) shows a device from Sample A under an injection current of 100 $A/cm^2$. It is seen that there is a significant amount of light being emitted from the edges of the device mesa, despite the metal contact completely covering the top of the device.

We studied the emission polarization properties of sample A as well as an LED with an identical structure but having emission at 265 nm. The samples were placed under a constant CW bias corresponding to an injected current density ~50 $A/cm^2$. A Glan-Taylor calcite polarizer with a high-precision rotation mount system was placed on the sample top surface to resolve the emission. Figure 7.2(c) plots the EL spectra for the two devices at polarization angles of 0˚ and 90˚. A much larger change in intensity was seen for the 245 nm LED as compared to the 265 nm device, suggesting a significantly larger degree of polarization. This is consistent with previous studies that report the light emission becoming more TM polarized for higher Al compositions [300]. The variation of the EL intensity, normalized to the minimum value for each device, with polarization angle for the two devices is shown in Fig. 7.2(d). The degree of polarization was measured to be -0.602 and -0.078 for the 245 nm and 265 nm LEDs, respectively, which confirms a major shift towards emission that is dominantly TM-polarized with decreasing wavelengths. It

is therefore expected that the device efficiency can be significantly enhanced by engineering the polarization of the light emission to be more TE-like [46, 209, 301], by utilizing nanostructures [44, 83, 84, 111, 153], and/or by removing the substrate [78, 302, 303].

The output power was measured from the bottom of the sapphire substrate using a Newport 818-ST2-UV photodetector with a Newport Model 1919-R power meter. The devices were probed under CW biasing conditions. Figures 7.3(a) and (b) show the variation of EQE and WPE, respectively, with current density for samples A and C. The maximum EQE and WPE were measured for sample A, attaining 0.35% and 0.21% respectively, at a current density of 0.25 A/cm$^2$. The peak EQE and WPE of sample A is over 50% higher than that of sample C. In fact, the measured efficiency values are more than one order of magnitude higher than previously reported tunnel junction devices at these wavelengths [230, 270, 271]. Sample B exhibited extremely low efficiencies (~0.001%), due to the leaky I-V, which are not shown here. Given that both samples A and C have identical active region and tunnel junction designs, the improved performance of sample A can be well explained by the incorporation of a polarization engineered p-AlGaN EBL layer, which can help reduce electron overflow and enhance the device efficiency. This observation is also consistent with the enhanced electron overflow of sample C derived from electrical analysis, as described above. The underlying cause for the severe electron overflow is due the highly asymmetric electron and hole transport properties of Al-rich AlGaN [103, 104, 270], which fundamentally limits the maximum achievable efficiency of deep UV LEDs.

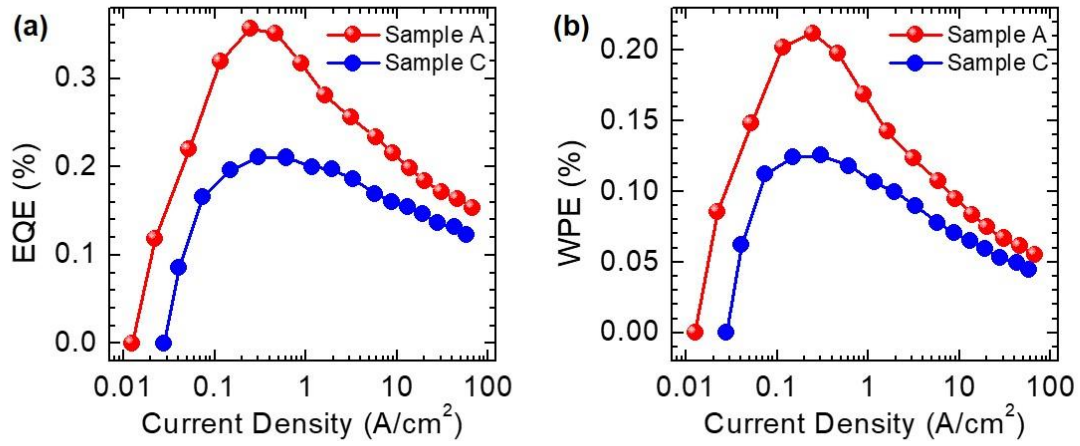


*Figure 7.3:(a) EQE vs. current density of Sample A and C, measured using CW bias. (b) WPE vs. current density of Sample A and C, measured using CW bias.*

## 7.5 Optical Measurements of Active Region

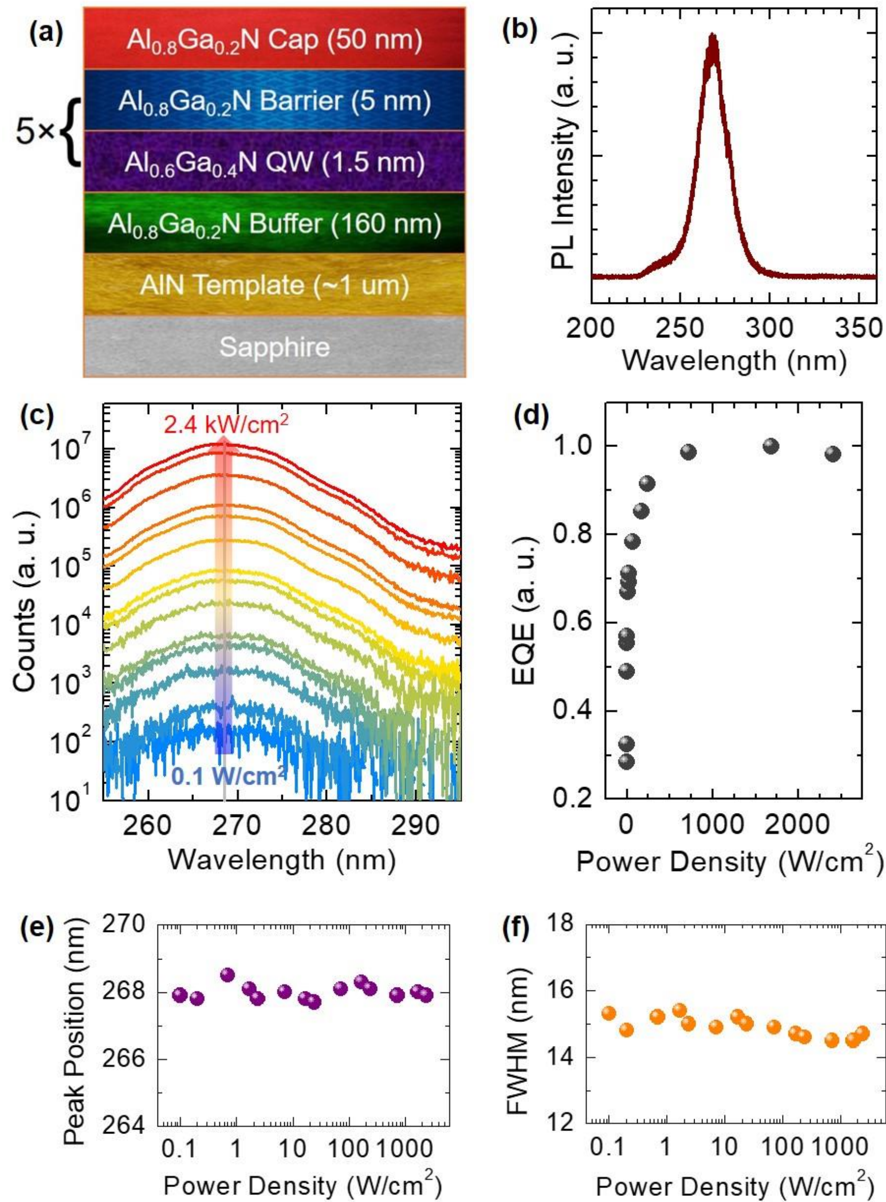


*Figure 7.4:(a) Structure of the sample used for optical measurements. (b) Room-temperature photoluminescence spectra for the structure measured using 193 nm excitation. (c) Intensity-dependent photoluminescence spectra measured for the sample using quasi-resonant excitation of the active region. (d) Relative EQE measured for optical emission at different excitation powers. (e) Variation of peak position with excitation power density. (f) Plot of measured full-width half maximum for the emission peak at different excitation power densities.*

It is also noticed that similar efficiency droop phenomena have been measured in AlGaN LEDs operating at 255-280 nm wavelengths [103, 104, 270]. To further confirm if the observed efficiency droop is due to an electrical effect, we studied the optical properties of the AlGaN quantum well active region (~265 nm), schematically shown in Fig. 7.4(a), to determine if it plays a significant role in the efficiency droop process. Figure 7.4(b) shows the PL spectrum measured by exciting the sample using a 193 nm Coherent Excistar XS500 laser. It shows the presence of two peaks, one located at ~240 nm originating from the high Al-content barrier layers, and another at ~268 nm, originating from the quantum wells. To study only the luminescence from the quantum wells, and avoid the effects of carrier transport between the wells and barriers, the sample was resonantly excited using a frequency-tripled Ti:sapphire laser (~ 245 nm) with an 80 MHz repetition rate and 100 fs pulse width. The excitation power was varied over several orders of magnitude and the PL spectra are shown in Fig. 7.4(c). The relative EQE is shown in Fig. 7.4(d), exhibiting no significant droop up to an excitation power of 2.4 $kW/cm^2$, which corresponds to an estimated carrier density ~$2 \times 10^{18}$ $cm^{-3}$ [203, 304, 305]. A negligible change in peak position was seen over this wide excitation range, shown in Fig. 7.4(e), suggesting that the emission is a result of the radiative recombination of highly confined and localized carriers. The linewidth of the emission, plotted against excitation power in Fig. 7.4(f), remains almost constant throughout the excitation range, showing negligible quantum-confined Stark effect.

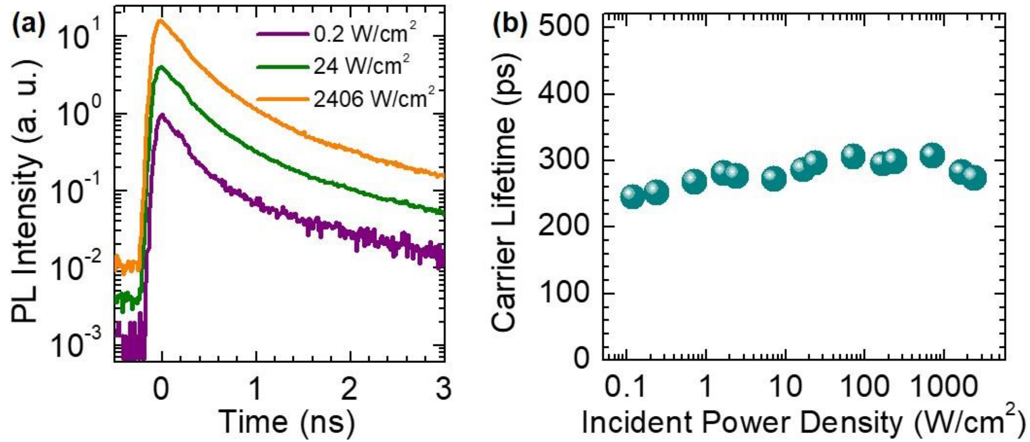


*Figure 7.5:(a) Time-resolved photoluminescence decays at different excitation powers collected for the sample used in optical measurements. (b) Plot of extracted carrier lifetime vs. excitation power density.*

TRPL transients were also collected at different optical excitation powers using a thermoelectrically cooled fast hybrid photomultiplier tube. Some representative transients are shown in Fig. 7.5(a), which exhibit an almost negligible change in their decay over the excitation range. Figure 7.5(b) plots the extracted carrier lifetimes by using the stretched-exponential model [196, 306]. The nearly invariant carrier lifetime (~0.3 ns) shows that the carrier recombination dynamics do not change significantly over the excitation range, suggesting that higher order carrier loss processes, e.g., Auger recombination, is not significant in the measured excitation power range. Auger recombination would cause an increase in non-radiative emission and a decrease in carrier lifetime when the excitation power is increased [203, 304, 305]. The carrier lifetimes measured were comparable to previously reported high quality AlGaN epilayers grown by MBE [307]. It is also noteworthy that the extracted carrier lifetimes are significantly lower than those measured for AlGaN quantum wells grown by metal-organic chemical vapor deposition (MOCVD) [203], which can be explained by the strong quantum-confinement of charge carriers in the quantum dot-like nanoclusters for samples grown by plasma-assisted MBE. Furthermore,

no evidence of droop is observed in the optical measurements up to an estimated carrier density ~$2 \times 10^{18}$ $cm^{-3}$. For comparison, previously reported blue-emitting InGaN quantum wells [305] also did not display any efficiency droop up to carrier densities ~$5 \times 10^{18}$ $cm^{-3}$, which approximately corresponds to injection current densities 5-15 $A/cm^2$. Given the shorter carrier lifetime measured in the presented AlGaN active region, this carrier density corresponds to a higher current density than that observed in InGaN LEDs for the onset of efficiency droop [196, 305, 308, 309]. Therefore, it is reasonable to conclude the measured efficiency droop in electroluminescence at ~0.25 $A/cm^2$ is not an optical phenomenon, but instead related to an electrical origin, i.e., electron overflow.

## 7.6 Summary

In conclusion, we have demonstrated AlGaN deep UV tunnel junction LEDs operating at ~245 nm, which exhibit significantly improved efficiency compared to previous reports. Severe efficiency droop was measured at low current densities. Detailed electrical and optical studies suggest that the efficiency droop is directly related to electron overflow, instead of an optical phenomenon. Moreover, the MBE grown AlGaN deep UV LED active region is characterized with the presence of nanoscale clusters. The resulting strong three-dimensional confinement of charge carriers can significantly reduce quantum-confined Stark effect, leading to highly stable and efficient emission. Our studies further suggest that AlGaN deep UV LEDs with efficiency comparable to InGaN blue-emitting quantum wells can be potentially achieved, if issues related to electron overflow and TM polarized emission are effectively addressed.

# Chapter 8. Summary and Future Work

## 8.1 Summary

The work presented in thesis addresses the physics, materials, and device engineering challenges for achieving high efficiency mid and deep UV AlGaN UV LEDs, which are the only alternative technology to replace conventional mercury/xenon lamps for water/air purification.

Chapter 3 discusses the technique of metal-semiconductor junction-assisted epitaxy that was used to grow p-type Mg-doped AlGaN with a high hole concentration and low hole resistivity, even for AlGaN compositions approaching 90% Al. UV LEDs grown using this method showed considerably improved performance as compared to LEDs grown using conventional epitaxy.

Then in Chapter 4, to address the electron overflow of carriers out of the active region, due to the significantly higher carrier concentrations and mobilities in n-type AlGaN as compared to p-type AlGaN, different configurations of the electron blocking layer were investigated in UV LEDs operating at ~280 nm. It was shown that an n-type EBL provides significantly more benefits than the standard p-type EBL especially for UV LEDs. An n-type EBL can block the flow of electrons to the device action region while not impeding the hole injection. Simultaneously the incorporation of a superlattice n-EBL can further improve the lateral conductivity of electrons due to the polarization-induced doping at the interfaces of the different layers of the superlattice.

In Chapter 5, we introduced a tunnel junction structure for devices with emission at ~265 nm. For these high Al compositions, hole injection into the p-type region is a severe bottleneck to device efficiency, and a tunnel junction can help mitigate this issue. Different designs of the tunnel junction were grown, fabricated and measured to optimize device performance. Significantly improved current-voltage characteristics and efficiency was measured with the incorporation of GaN layer thickness ~5 nm. The optimized AlGaN deep UV LED exhibited a maximum EQE and WPE of 11% and 7.6%, respectively.

Chapter 6 presents a detailed investigation of the electrical and optical properties of a high-efficiency tunnel junction UV LED with emission at 255 nm. A maximum EQE of 7.2% and WPE of 4% were measured for the devices, which are higher than previously reported tunnel junction devices operating at this wavelength. The devices exhibited a nearly constant emission peak over a wide current range, due to the strong charge carrier confinement in the Ga-rich nanoclusters present in the AlGaN layers. Detailed temperature-dependent measurements suggest that the presence of severe efficiency droop of deep UV LEDs is largely due to electron overflow. Temperature-dependent measurements also elucidate the impact of thermal effects on the electrical and emission properties of the device.

Chapter 7 consists of an investigation into the role of the electron blocking layer and polarization-induced doping on the performance of 245 nm tunnel junction UV LEDs. Optimized devices with a graded Mg-doped AlGaN EBL showed improved performance with a maximum EQE of 0.25% and WPE of 0.13%. The optical properties of the AlGaN active region confirmed that the emission observed originates in Ga-rich clusters present in these materials. Based on our

results, electron overflow has a major impact on limiting device performance, which emphasizes the importance of improving the p-type doping in AlGaN to have better performance UV LEDs.

## 8.2 Future Work

### *8.2.1 Using Nanostructures for AlGaN Devices*

Throughout this thesis epilayers were used. However, nanostructures such as nanowires and nanowalls provide several advantages over epilayers. These nanoscale structures have an almost defect-free structure [105, 106] and their growth results in enhanced incorporation of dopants [107, 108]. These structures also have a larger surface area available for emission, resulting in an enhanced extraction of generated photons [109]. Furthermore, selective area growth (SAG) provides a method of growing nanostructures only in designated regions of a wafer, enabling the growth of photonic crystal arrays as well [44, 82, 83, 111]. These arrays of nanostructures can enhance light extraction, make the emitted light directional, and guide light modes of a laser. The growth mechanism of nanowires enables the growth of high-quality III-nitrides on amorphous substrates as well [310, 311].

AlGaN-based nanostructure devices have been previously demonstrated [67, 86, 107, 180, 214, 269, 270, 273, 312], however despite their promise, the efficiency remains low as compared to planar devices. Significant progress can be made in this field if the issues of carrier leakage and surface recombination are mitigated. Furthermore, N-polar AlGaN nanostructure devices can be grown and fabricated. These devices show the potential to further improve device performance by improving carrier injection. They have been demonstrated to suppress the droop in nitride LEDs, even at high operating currents [313-317].

We have performed some preliminary selective area growths of InGaN and AlGaN on N-polar GaN substrates. These substrates were grown directly on sapphire by Dr. Ping Wang in a Veeco GENxplor PA-MBE system. Following the substrate growth, the wafer was unloaded, diced and then patterned using electron beam lithography to define arrays of openings in a Ti layer on the surface. The nanowire growth was then performed in a Gen930 MBE system. An SEM image of the nanowires is shown in Fig. 8.1(a). These nanowire arrays were then fabricated into devices.

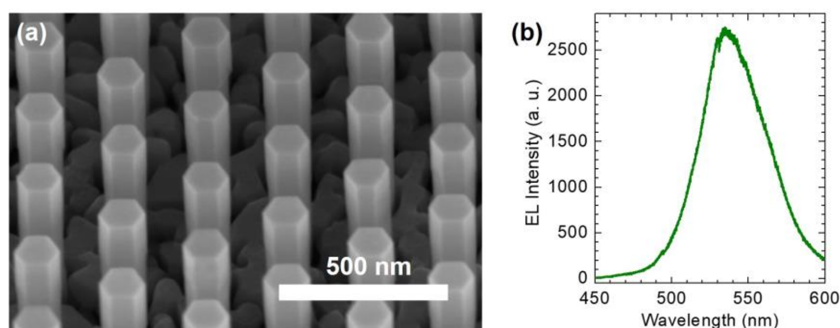


*Figure 8.1: (a) SEM image of an N-polar nanowire array. (b) EL spectra of a green-emitting N-polar nanowire LED.*

The fabricated devices show strong luminescence, as shown in Fig. 8.1(b). The devices also demonstrated excellent J-V characteristics and relatively high efficiencies for micron-scale devices, which shows their potential to realize efficient microLEDs. Optimization of the pattern design, nanowire epitaxy, and fabrication procedure are in progress to further improve the performance of these devices.

Based on the promising results obtained in InGaN N-polar LEDs, we have also started establishing the growth conditions for AlGaN structures emitting in the UV. Shown in Fig. 8.2(a)

is an SEM image of an N-polar AlGaN/GaN nanowire. The structure consisted of an initial 300 nm GaN layer followed by a 100 nm thick AlGaN layer with ~5% Al composition. We observe a good selectivity and nanowire morphology. The PL spectrum shown in Fig. 8.2(b) confirms the presence of AlGaN with a peak located at ~350 nm. The future steps in this project would be further optimizing the emission wavelength, intensity and morphology of the AlGaN nanowires, followed by the growth and fabrication of devices.

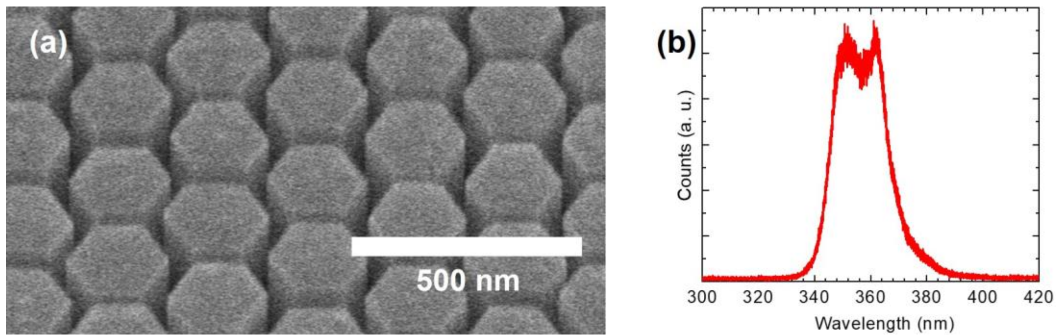


*Figure 8.2:(a) SEM image of N-polar AlGaN nanowires grown by SAG. (b) PL spectrum of AlGaN nanowire array.*

### *8.2.2 Extending Tunnel-Junction UV LEDs to Shorter Wavelengths*

This thesis has already demonstrated tunnel junction based AlGaN UV LEDs down to 245 nm. However, shorter wavelengths close to 220 nm are more desirable from the perspective of sterilization and safety. Therefore, further work needs to be done on increasing the efficiencies of tunnel junction devices at even shorter wavelengths. We have also used a structure that is based on the optimizations for a device with AlGaN layers around the tunnel junction with compositions close to 60% Al [104]. However, the optimized thickness of the middle GaN layer is highly sensitive to Al composition due to the strong spontaneous polarization of AlN. This would mean that its thickness can be further optimized for higher Al compositions. Furthermore, as defect-

assisted tunneling might already be playing an important role in the tunneling of carriers [238, 241, 243], this effect could be deliberately enhanced by introducing dopants such as Mg within this layer.

### *8.2.3 Substrate Removal*

Substrate removal has emerged as a technique for dramatically increasing the light extracted from LEDs, while also enabling the integration of nitride semiconductor devices with other substrates [78]. Our group has previously investigated the growth of AlGaN LEDs on graphene-on-AlN templates. The presence of the graphene layer could aid the peel-off of the epitaxially grown layers, which can then be transferred onto other substrates and fabricated [302, 318, 319]. A schematic of possible lift-off processes involving a stressor layer (such as thick Ni) or laser lift-off a shown in Figs. 8.3(a) and (b), respectively. Figure 8.3(c) shows a schematic of the transfer process of the epitaxial layers onto another substrate following lift-off, and the final fabricated device. The removal of the substrate will aid light extraction, and by transferring the epitaxial LED layers onto a reflective metal substrate, the LEE will be further improved, while the metal can also act as a contact and heat sink, aiding the high-power operation of these devices.

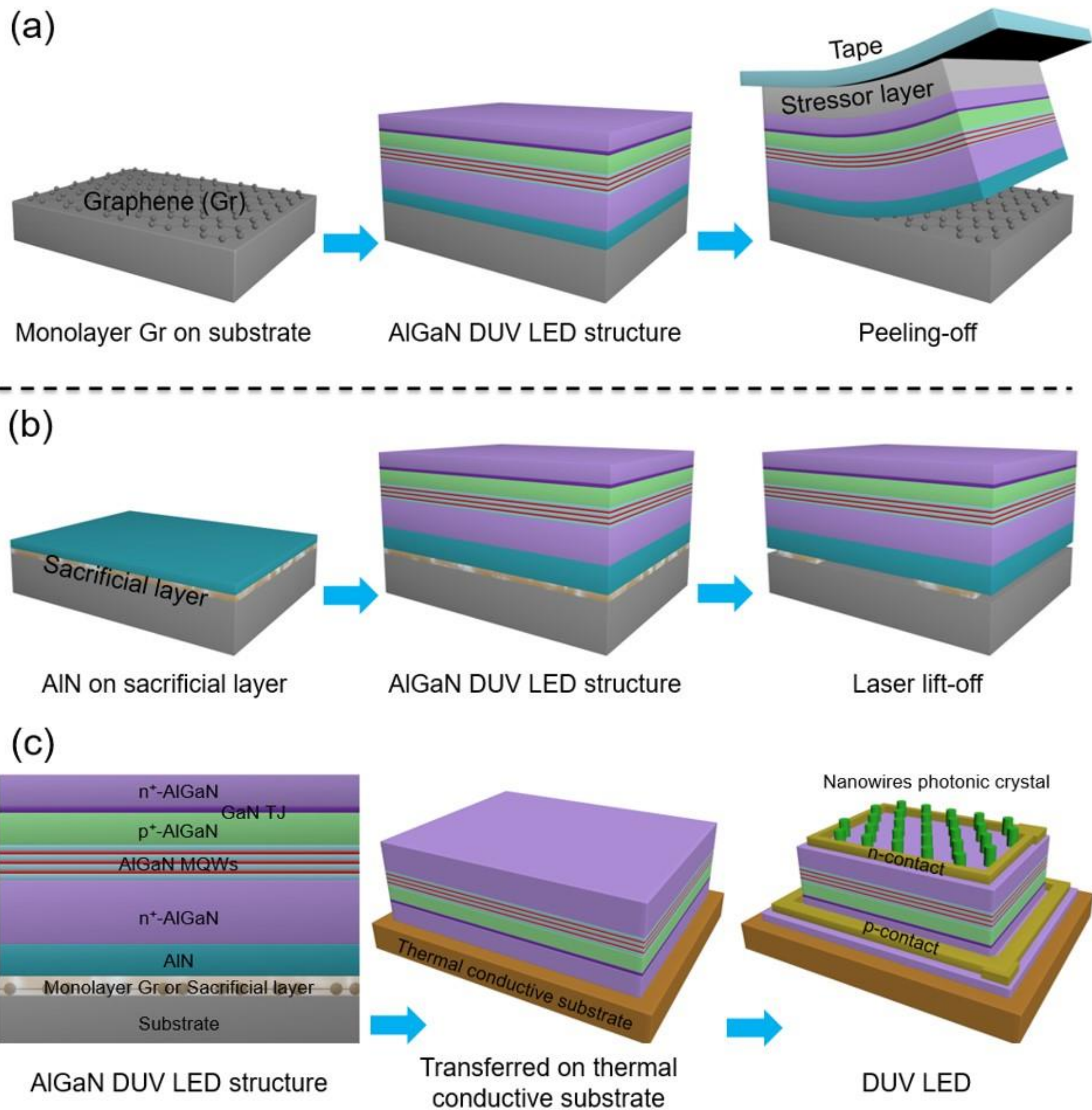


*Figure 8.3: Schematics of (a) the growth and peeling-off process of AlGaN DUV LED structure on graphene. (b) The growth and laser lift-off process of AlGaN DUV LED structure on sacrificial layer/sapphire. (c) The device fabrication process of transferred AlGaN DUV LED.*

### *8.2.4 P-doping using Beryllium as Dopant*

While magnesium is the standard acceptor dopant for the III-nitrides, there has been previous work on the investigation of other dopants as well [154, 320-323]. Recent work has shown that beryllium (Be) can be used as an acceptor dopant in AlN, with a predicted activation

energy of ~340 meV [324, 325], as compared to 600 meV for Mg. The much-reduced activation energies would result in orders of magnitude higher hole concentration at room temperature, possibly solving the critical challenge of p-type doping in AlN.

### *8.2.5 Understanding the Carrier Dynamics in AlGaN UV Devices*

In this thesis we have shown how the presence of Ga-rich nanoclusters in AlGaN layers, which were grown by MBE under slightly Ga-rich conditions, largely determine the optical emission properties of the material. However, further investigation is needed of the carrier dynamics for capture, escape and recombination of carriers in these clusters [326]. The effects of the non-uniform injection of electrons and holes may be mitigated by optimizing the carrier capture in the highly localized nanoclusters.

### *8.2.6 Development of UV-C Laser Diodes Using MBE*

Recently, AlGaN quantum well edge-emitting UV-C wavelength laser diodes have been demonstrated [36]. These devices were grown on single crystal AlN substrates to minimize defects, however for practical use they are prohibitively expensive. Due to the severe heating caused by the large threshold current of these devices, they could only be operated for very short pulses. Growing such short-wavelength lasers on sapphire substrates would be a remarkable achievement.

With the use of AlGaN nanowire arrays, low threshold surface emitting laser diodes have been demonstrated previously [67, 83, 84, 111, 153]. For a two-dimensional AlGaN photonic crystal array, at the band-edge the group velocity of light becomes zero, and a two-dimensional cavity mode is formed in the photonic crystal. The photonic crystal itself serves as a diffraction

grating, and the output beam is emitted from the surface. This allows for lasing even at relatively low injection currents, which is critical for high Al content UV devices where it is quite difficult to obtain high carrier concentrations. To achieve AlGaN UV laser diodes with high performance, we aim to develop AlGaN nanowire photonic crystal surface emitting laser diodes.

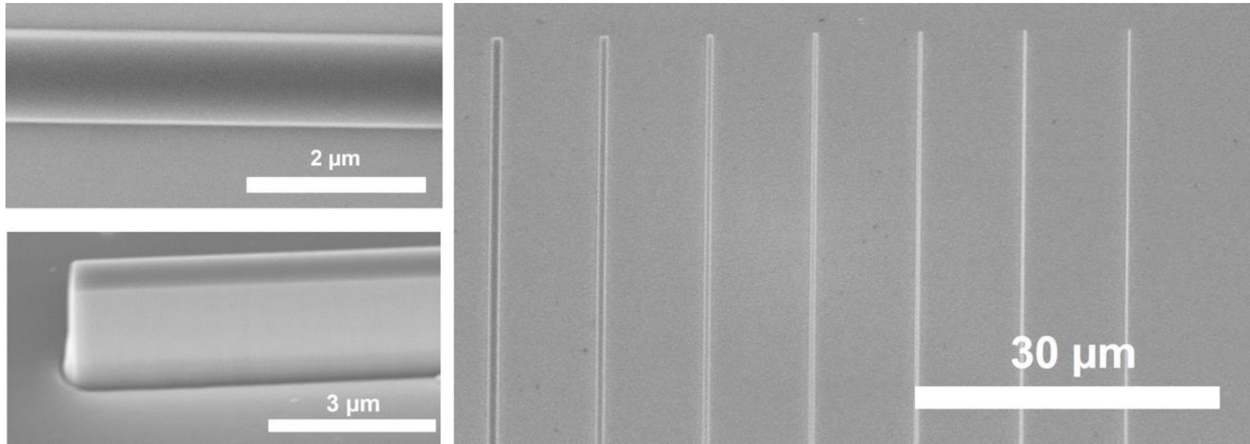


*Figure 8.4: SEM images of etched GaN ridges.*

Apart from growing photonic crystals for guiding the light modes, ridge waveguide lasers are also a possibility. A novel approach for growing bottom-up ridge lasers is through the growth of a nano-wall, where the ridge is predefined, either by etching the substrate or through a mask as in SAG. For this purpose, long ridges with extremely smooth sidewalls are crucial and they must be patterned precisely. The initial design and preparation of ridge patterns on a GaN substrate is shown in Fig. 8.4. The future directions of this project involve the optimization of the growth of AlGaN on the patterned ridges, followed by the fabrication of devices.

# Appendices

# Appendix A Substrate Preparation for MBE Growth

The wafers used in this thesis were purchased from DOWA Holdings Co., Ltd. They were 2 inch in diameter, with 1 μm of AlN grown on it. The backside of the wafers was then coated using sputtering with 2 μm of molybdenum by Thinfilms, Inc. After receiving the wafers, they were then diced into 1 cm × 1 cm pieces. A solvent clean is then performed on the samples. They are cleaned in acetone and methanol for 5 minutes each, followed by rinsing the pieces in deionized water 5 times.

The pieces are then mounted onto a 3-inch Si carrier wafer using indium mounting. The backside Mo on the pieces is completely covered in indium for this process to enable proper adhesion onto the carrier wafer at the temperatures required for growth. Multiple pieces can be mounted on the same carrier wafer to increase the yield from a single growth. Once the pieces are loaded onto the carrier, they are ready to be loaded into the MBE system.

Initially the samples are loaded into the intro chamber where they are degassed at 200 ˚C for 90 minutes. They are then degassed in the prep chamber at 500 ˚C for 60 minutes. They are then loaded into the growth chamber for growth.

# Appendix B Fabrication Procedure for AlGaN Epilayer LEDs

## 1. Sample cleaning

After growth the backside of the sample would be covered in In due to the mounting process, so the sample needs to be cleaned prior to processing. The Mo layer on the back of the wafer also needs to be removed for backside emitting devices.

a. HCl clean until all the indium is etched away from the backside.
b. Leave the sample in Aluminum Etchant Type A till all the Mo is etched away.
c. Solvent clean using acetone and methanol.
d. Rinse the sample using DI water

## 2. Mesa etching

The first step in the device fabrication involves defining the device mesas. The rest of the wafer is etched down to the bottom n-AlGaN contact layer. This process is performed using either ion milling or reactive ion etching (specified in text). Figure B.1 shows a schematic of the process.

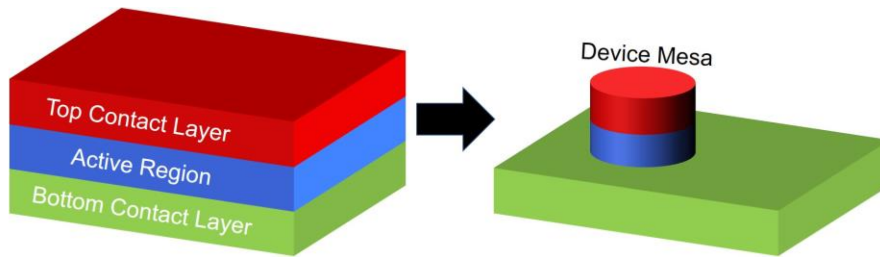


*Figure B.1: Etching to form device mesa.*

a. Spin coat SPR 220 3.0 at 4000 RPM for 30 seconds. Pre-bake it at 115 ˚C for 60 seconds.
b. Expose using the MJB-3 contact aligner for 8 seconds. The exposure mask defines the device mesas.
c. Develop the photoresist using AZ 726 for 45 seconds using a single puddle.
d. Verify that the dimensions of the photoresist covering the device mesas are accurate using an optical microscope.
e. Mount the samples onto a suitable carrier wafer using low temperature crystal bond.
f. Etch down to the bottom n-AlGaN contact layer using the Nanoquest Ion Mill if using ion milling, or Oxford ICP RIE if using reaction ion etching. The ion mill also has the added capability of SIMS which allows for tracking the layer that is being etched.
g. Following the etching, clean the photoresist using remover PG.
h. Verify that the etch depth is accurate using Dektak Profilometer.

**3. Deposition of insulation layer**

Once the mesas are defined, the sample is coated using 300 nm of PECVD $SiO_2$. This ensures that the top and bottom layer contacts will be insulated from each other. An image of the process is shown in Fig. B. 2.

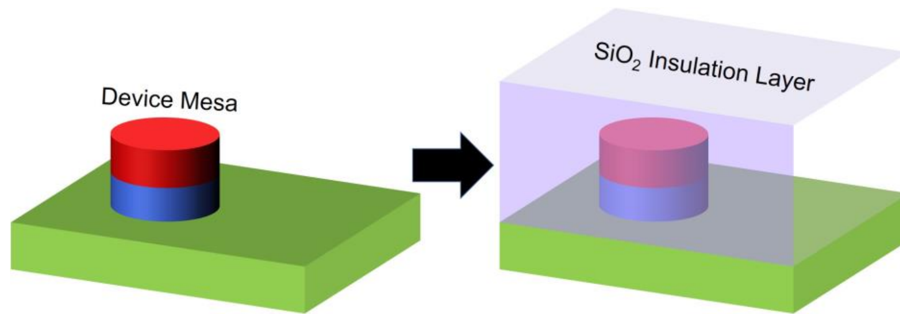


*Figure B.2: Schematic of the sample after deposition of insulation layer.*

a. Solvent clean the sample using the procedure described in steps c) and d) from Section 1 on sample cleaning.
b. Load the sample into the Plasmatherm 790 and deposit 300 nm of $SiO_2$ at 350 ˚C.

**4. Etching of vias and contact deposition**

Next, vias are etched into the insulation layer, where the device mesas are, and where the contacts to the bottom layer are to be placed. Following the etching of the vias, contacts can be deposited for both the bottom and top layers. An image of the process is shown in Fig. B. 3.

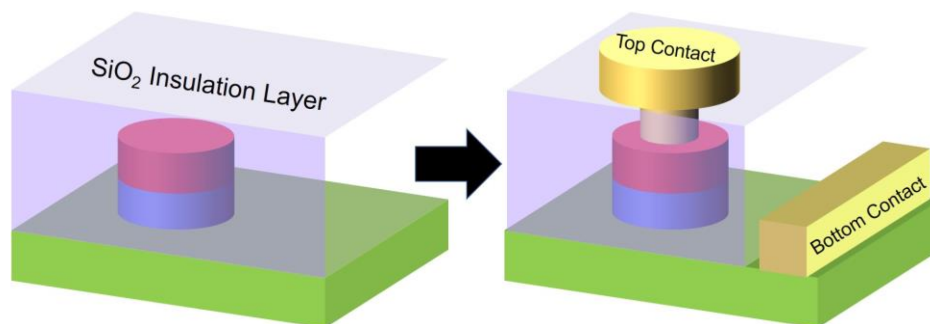


*Figure B.3: Etching of vias and contact deposition.*

a. Solvent clean the sample using the procedure described in steps c) and d) from Section 1 on sample cleaning.
b. Spin coat SPR 220 3.0 at 4000 RPM for 30 seconds. Pre-bake it at 115 ˚C for 60 seconds.
c. Expose using the MJB-3 contact aligner for 8 seconds. The exposure mask defines the regions where vias will be etched into the insulation layer.
d. Develop the photoresist using AZ 726 for 45 seconds using a single puddle.
e. Verify that the dimensions and alignment of the vias are accurate using an optical microscope.
f. Mount the samples onto a suitable carrier wafer using low temperature crystal bond.
g. Etch the insulation layer in the via regions using the LAM 9400.
h. Following the etching, clean the photoresist using remover PG.
i. Spin coat SPR 220 3.0 at 4000 RPM for 30 seconds. Pre-bake it at 115 ˚C for 60 seconds.
j. Expose using the MJB-3 contact aligner for 8 seconds. The exposure mask defines the regions where the metal contacts will be deposited.
k. Develop the photoresist using AZ 726 for 45 seconds using a single puddle.
l. Verify that the dimensions and alignment of the device contacts are correct.
m. For the bottom n-contact, Ti (40 nm)/Al (120 nm)/Ni (40 nm)/Au (100 nm) is deposited as the metal stack using e-beam evaporation.
n. Perform lift-off following the deposition using remover PG.
o. The metal contacts are then annealed at 700 ˚C in nitrogen for 30 seconds.
p. Steps i-l are then repeated for the top contact.
q. For the top contact, if the device has a p-contact layer, Ni (20 nm)/Au (100 nm) is used as the metal contact, and if the device is a tunnel junction with an n-type top contact layer, Ti (40 nm)/Al (120 nm)/Ni (40 nm)/Au (100 nm) is deposited as the metal stack.

r. Perform lift-off following the deposition using remover PG.

s. The metal contacts are then annealed at 500 ˚C in air for 60 seconds if the device uses a Ni/Au top contact, and it is annealed at 700 ˚C in nitrogen for 30 seconds if it has a Ti/Al/Ni/Au top contact.

t. The wafer is finally diced into dies for measurement.

## Appendix C Supporting Information for Chapter 3

### Section 1: Theoretical Calculations

Density functional theory calculations were performed with HSE06 hybrid functional [327] and projected augmented wave method [328, 329], as implemented in Vienna *Ab initio* Simulation Package (VASP) [330]. GW-compatible pseudopotentials were used, where Mg 3s, Al 3s3p, Ga 4s4p, and N 2p states were treated as valence electrons. The fraction of non-local Hartree-Fock exchange in the hybrid functional is 0.30 for GaN and $Al_{0.5}Ga_{0.5}N$, and 0.33 for AlN, giving their band gap values of 3.51 eV, 4.65 eV, and 6.20 eV respectively, in close agreement with the experiments [331-333]. Defect calculations were performed for GaN, $Al_{0.5}Ga_{0.5}N$ and AlN using 96-atom orthorhombic supercells [323] with 2×2×2 Gamma-center k-point grid and a plane wave energy cut-off of 500 eV. Special quasi-random supercell (SQS) of $Al_{0.5}Ga_{0.5}N$ were generated by Alloy Theoretic Automated Toolkit (ATAT) [334]. All structures were relaxed until the force on ions is less than 0.02 eV $Å^{-1}$, with spin-polarization included for un-paired electrons. Corrections to the charged defects were employed, based on Freysoldt scheme [335], which eliminates the electrostatic interactions between image charges in the supercell approach.

For first principles calculations on the thermodynamics of Al(Ga) substitutional Mg-dopant incorporation, we calculated the formation energy using [336]:

$$E^f\left(Mg_X^f\right) = E_t\left(Mg_X^q\right) - E_t(Al_x Ga_{1-x} N) + (E_t(X) + \mu_X) - \left(E_t(Mg) + \mu_{Mg}\right) + q(E_F + E_{VBM}) + E_{corr} \quad \textit{(Equation C.1)}$$

where $E_t(Mg_X^q)$ is the total energy of the defective supercell containing one Al(Ga)-substitutional Mg in charge state $q$ and $E_t(Al_x Ga_{1-x} N)$ is the total energy of the perfect host supercell. $E_t(X)$ and $E_t(Mg)$ are the total energy of Al(Ga)N and Mg in their bulk forms. $\mu_X$ and $\mu_{Mg}$ are the chemical potentials of Al(Ga)N and Mg referenced to their elemental phase. $E_F$ is the energy of the Fermi level in AlGaN referenced to its bulk valence band maximum. $E_{corr}$ is the correction energy for the charged defects. For the atomic chemical potentials, we assumed thermodynamic equilibrium of $Al_{0.5}Ga_{0.5}N$, and suppressed the formation of $Mg_3N_2$.

$$0.5\mu_{Al} + 0.5\mu_{Ga} + \mu_N = \Delta H(Al_{0.5}Ga_{0.5}N) = -2.09\ eV \quad \textit{(Equation C.2)}$$

$$3\mu_{Mg} + 2\mu_N < \Delta H(Mg_3N_2) = -4.02\ eV \quad \textit{(Equation C.3)}$$

where $\Delta H(X)$ denotes the formation enthalpy of compound X. Since out AlGaN films were grown using metal-semiconductor junction assisted epitaxy, the calculations assume metal-rich, N-poor growth conditions.

Unlike their binary counterparts, AlGaN alloys can host substitutional Mg on either the Ga or Al sites, $Mg_{Ga}^0$ and $Mg_{Al}^0$ respectively. To determine which sites are more energetically favorable for Mg to occupy, we calculated the formation energy of Mg-dopants in 5 random Ga sites and 1 Al site in the $Al_{0.5}Ga_{0.5}N$ supercell, and their values are summarized in Table C.1. While the activation energies of Mg acceptors on different substitutional sites vary only by approximately

0.1 eV, the formation energy of $Mg_{Ga}^{0}$ (2.00 eV) is almost 2 eV lower than $Mg_{Al}^{0}$ (3.94 eV) under Ga(Al)-rich conditions, indicating that Mg dopants prefer to substituting Ga rather than Al sites. This emphasizes the difficulty of incorporating high Mg concentrations in Al rich AlGaN.

*Table C.1: Formation energy and activation energy of neutral Mg dopants on different substitutional sites on $Al_{0.5}Ga_{0.5}N$ under metal-rich conditions.*

| **Site No.** | 1 | 2 | 3 | 4 | 5 | 6 |
|---|---|---|---|---|---|---|
| **Defect** | $Mg_{Ga}^{0}$ | $Mg_{Ga}^{0}$ | $Mg_{Ga}^{0}$ | $Mg_{Ga}^{0}$ | $Mg_{Ga}^{0}$ | $Mg_{Al}^{0}$ |
| **Formation Energy (eV)** | 1.996 | 1.937 | 1.999 | 1.963 | 1.899 | 3.944 |
| **Activation Energy (eV)** | 0.639 | 0.636 | 0.601 | 0.724 | 0.668 | 0.589 |

During the MBE growth process of AlGaN layers the growth temperature of the substrate was 700 °C. At this growth temperature, the bandgap of AlGaN can be calculated using the Varshni equation, and using typical parameters for $Al_{0.7}Ga_{0.3}N$ [5, 337, 338] the bandgap is calculated to be 4.65 eV. The electron affinity is calculated as 1.65 eV. For a liquid Ga metal layer, a work function of 4.2 eV is assumed, and assuming a free hole concentration of $10^{18}$ $cm^{-3}$ in the p-type AlGaN, the band structure at the growth interface is calculated as shown in Fig. C.1(a) and (b) for the conventional and metal-semiconductor junction assisted epitaxy, respectively. During metal-semiconductor junction assisted epitaxy, the presence of the Ga layer on the surface creates a separation between the Fermi level and the valence band of ~2.2 eV at the growth front while it is only ~0.12 eV for conventional epitaxy.

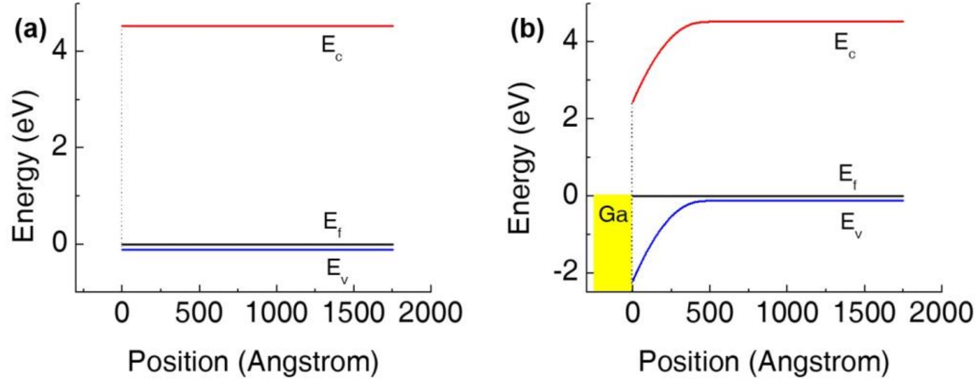


*Figure C.1: Band structure at the growth interface during the growth of Mg-doped AlGaN by (a) conventional epitaxy and (b) metal-semiconductor junction assisted epitaxy.*

For growth using metal-semiconductor junction assisted epitaxy, where the Fermi level is pinned away from the valence band, the formation energy is only 0.43 eV. Using the formula [174] $n_{Mg} = n_{sites} \cdot \exp(-\frac{E^f(Mg_{Ga}^{-1})}{k_B T})$ and setting the growth temperature to 700 °C, we calculated an estimated Mg concentration in the $Al_{0.5}Ga_{0.5}N$ to be $1.4\times10^{20}$ cm$^{-3}$, if we assume the number of Ga sites $n_{sites}$ in $Al_{0.5}Ga_{0.5}N$ to be $2.26\times10^{22}$ cm$^{-3}$.

**Section 2: RHEED Pattern during Epitaxy**

The RHEED patterns were monitored during the epitaxy of the layers to determine the growth conditions *in situ*. A dim, streaky RHEED pattern indicates a smooth, metal-rich growth surface, which was maintained throughout the growth. Growth using conventional epitaxy doesn't have a Ga metal layer on the surface, and the RHEED is typically characterized by the presence of clear segments, signifying a rough surface morphology. Figures C.2(a) and (b) show SEM images of samples grown using conventional and metal-semiconductor junction assisted epitaxy,

respectively, while Figs. C.2(c) and (d) show the corresponding RHEED patterns for these growths.

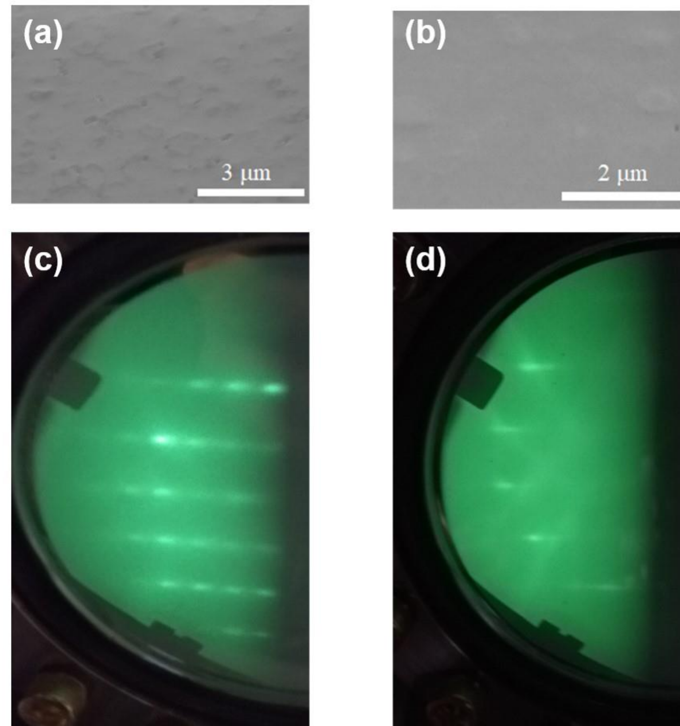


*Figure C.2: SEM images of the sample surface of p-AlGaN grown using (a) conventional epitaxy and (b) metal-semiconductor junction assisted epitaxy. RHEED patterns for (c) conventional epitaxy and (d) metal-semiconductor junction assisted epitaxy.*

The surface of the sample grown under the conventional growth mode is relatively rough and it exhibits higher resistivity, compared to the Mg-doped AlGaN grown by metal-semiconductor junction assisted epitaxy. It is important to mention that the amount of Ga coverage should be properly optimized to achieve the best results as an excess amount of Ga during the growth degraded the p-type conduction in the samples.

## Section 3: Mg Incorporation in AlGaN Epilayers

Incorporated Mg concentration vs. Mg flux for samples grown with three different Al compositions are shown in Fig. C.3. These samples were grown using metal-semiconductor junction assisted epitaxy to maximize Mg incorporation. For the same Mg flux used, a significant decrease in the Mg incorporation is observed with increasing Al composition of the alloy.

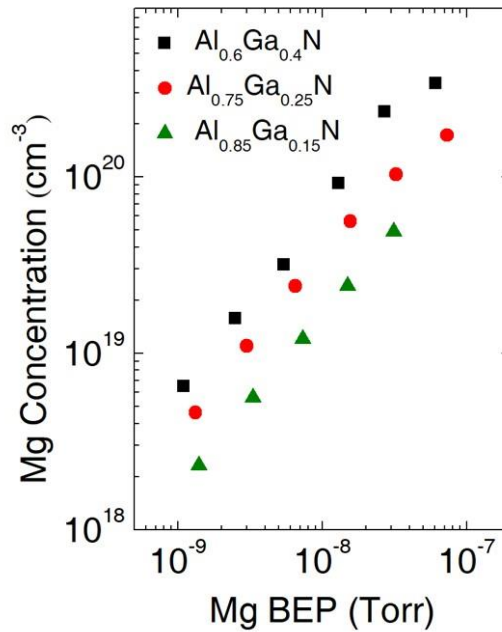


*Figure C.3:Mg atom concentration plotted against Mg flux for samples grown using metal-semiconductor junction assisted epitaxy with different Al compositions.*

## Bibliography


1. https://www.nterilizer.com/index.php/products/uv-sterilizing-technology.
2. http://hyperphysics.phy-astr.gsu.edu/hbase/Electronic/leds.html.
3. S. Karpov, Optical and Quantum Electronics **47** (6), 1293-1303 (2015).
4. https://www.ecse.rpi.edu/~schubert/Light-Emitting-Diodes-dot-org.
5. I. Vurgaftman and J. n. Meyer, Journal of Applied Physics **94** (6), 3675-3696 (2003).
6. F. Bernardini, V. Fiorentini and D. Vanderbilt, Physical Review B **56** (16), R10024 (1997).
7. B. Arnaudov, T. Paskova, P. Paskov, B. Magnusson, E. Valcheva, B. Monemar, H. Lu, W. Schaff, H. Amano and I. Akasaki, Physical Review B **69** (11), 115216 (2004).
8. Y. Taniyasu and M. Kasu, NTT Tech. Rev **8** (8), 1-5 (2010).
9. O. Ambacher, J. Majewski, C. Miskys, A. Link, M. Hermann, M. Eickhoff, M. Stutzmann, F. Bernardini, V. Fiorentini and V. Tilak, Journal of physics: condensed matter **14** (13), 3399 (2002).
10. J. Lähnemann, O. Brandt, U. Jahn, C. Pfüller, C. Roder, P. Dogan, F. Grosse, A. Belabbes, F. Bechstedt and A. Trampert, Physical Review B **86** (8), 081302 (2012).
11. O. Ambacher, J. Smart, J. Shealy, N. Weimann, K. Chu, M. Murphy, W. Schaff, L. Eastman, R. Dimitrov and L. Wittmer, Journal of applied physics **85** (6), 3222-3233 (1999).
12. Y.-F. Wu, A. Saxler, M. Moore, R. Smith, S. Sheppard, P. Chavarkar, T. Wisleder, U. Mishra and P. Parikh, IEEE Electron Device Letters **25** (3), 117-119 (2004).
13. https://mwe.ee.ethz.ch/research/HEMT/GaNHEMTs.html.
14. S.-H. Park and S.-L. Chuang, Applied Physics Letters **76** (15), 1981-1983 (2000).
15. T. Takeuchi, H. Amano and I. Akasaki, Japanese Journal of Applied Physics **39** (2R), 413 (2000).
16. U. T. Schwarz, H. Braun, K. Kojima, Y. Kawakami, S. Nagahama and T. Mukai, Applied Physics Letters **91** (12), 123503 (2007).
17. J.-H. Ryou, P. D. Yoder, J. Liu, Z. Lochner, H. Kim, S. Choi, H. J. Kim and R. D. Dupuis, IEEE Journal of Selected Topics in Quantum Electronics **15** (4), 1080-1091 (2009).
18. J. S. Im, H. Kollmer, J. Off, A. Sohmer, F. Scholz and A. Hangleiter, Physical Review B **57** (16), R9435 (1998).
19. T. Takeuchi, C. Wetzel, S. Yamaguchi, H. Sakai, H. Amano, I. Akasaki, Y. Kaneko, S. Nakagawa, Y. Yamaoka and N. Yamada, Applied physics letters **73** (12), 1691-1693 (1998).
20. H. Zhao, G. Liu, J. Zhang, J. D. Poplawsky, V. Dierolf and N. Tansu, Optics express **19** (104), A991-A1007 (2011).
21. J. Simon, V. Protasenko, C. Lian, H. Xing and D. Jena, Science **327** (5961), 60-64 (2010).
22. S.-R. Jeon, Y.-H. Song, H.-J. Jang, G. M. Yang, S. W. Hwang and S. J. Son, Applied Physics Letters **78** (21), 3265-3267 (2001).
23. M. Diagne, Y. He, H. Zhou, E. Makarona, A. Nurmikko, J. Han, K. Waldrip, J. Figiel, T. Takeuchi and M. Krames, Applied Physics Letters **79** (22), 3720-3722 (2001).

24. M. J. Grundmann and U. K. Mishra, physica status solidi (c) **4** (7), 2830-2833 (2007).
25. S. Krishnamoorthy, D. N. Nath, F. Akyol, P. S. Park, M. Esposto and S. Rajan, Applied Physics Letters **97** (20), 203502 (2010).
26. J. Simon, Z. Zhang, K. Goodman, H. Xing, T. Kosel, P. Fay and D. Jena, Physical Review Letters **103** (2), 026801 (2009).
27. M. F. Schubert, Physical Review B **81** (3), 035303 (2010).
28. D. Stevenson, W. Rhines and H. Maruska, (Google Patents, 1974).
29. S. Nakamura, T. Mukai and M. Senoh, Applied Physics Letters **64** (13), 1687-1689 (1994).
30. T. D. Moustakas, (Google Patents, 1997).
31. https://www.nobelprize.org/prizes/physics/2014/press-release/.
32. S. Nakamura, T. Mukai and M. Senoh, Japanese Journal of Applied Physics **30** (12A), L1998 (1991).
33. S. Nakamura, M. Senoh and T. Mukai, Japanese Journal of Applied Physics **32** (1A), L8 (1993).
34. C. A. Hurni, A. David, M. J. Cich, R. I. Aldaz, B. Ellis, K. Huang, A. Tyagi, R. A. DeLille, M. D. Craven and F. M. Steranka, Applied Physics Letters **106** (3), 031101 (2015).
35. K. Sato, S. Yasue, K. Yamada, S. Tanaka, T. Omori, S. Ishizuka, S. Teramura, Y. Ogino, S. Iwayama and H. Miyake, Applied Physics Express **13** (3), 031004 (2020).
36. Z. Zhang, M. Kushimoto, T. Sakai, N. Sugiyama, L. J. Schowalter, C. Sasaoka and H. Amano, Applied Physics Express **12** (12), 124003 (2019).
37. K. Ding, V. Avrutin, Ü. Özgür and H. Morkoç, Crystals **7** (10), 300 (2017).
38. T. Takano, T. Mino, J. Sakai, N. Noguchi, K. Tsubaki and H. Hirayama, Applied Physics Express **10** (3), 031002 (2017).
39. M.-H. Chang, D. Das, P. Varde and M. Pecht, Microelectronics Reliability **52** (5), 762-782 (2012).
40. J. Speck and S. Rosner, Physica B: Condensed Matter **273**, 24-32 (1999).
41. D. Li, K. Jiang, X. Sun and C. Guo, Advances in Optics and Photonics **10** (1), 43-110 (2018).
42. K. Ban, J.-i. Yamamoto, K. Takeda, K. Ide, M. Iwaya, T. Takeuchi, S. Kamiyama, I. Akasaki and H. Amano, Applied physics express **4** (5), 052101 (2011).
43. J. Zhang, H. Zhao and N. Tansu, Applied Physics Letters **97** (11), 111105 (2010).
44. X. Liu, K. Mashooq, T. Szkopek and Z. Mi, IEEE Photonics Journal **10** (4), 1-11 (2018).
45. L. Feng, N. Zhang, J. Wang and J. Li, Results in Physics **15**, 102632 (2019).
46. T. Kolbe, A. Knauer, C. Chua, Z. Yang, V. Kueller, S. Einfeldt, P. Vogt, N. M. Johnson, M. Weyers and M. Kneissl, Applied Physics Letters **99** (26), 261105 (2011).
47. K. Nam, M. Nakarmi, J. Li, J. Lin and H. Jiang, Applied physics letters **83** (5), 878-880 (2003).
48. T. Kinoshita, T. Obata, H. Yanagi and S.-i. Inoue, Applied Physics Letters **102** (1), 012105 (2013).
49. X. Liu, A. Pandey, D. A. Laleyan, K. Mashooq, E. T. Reid, W. J. Shin and Z. Mi, Semiconductor Science and Technology **33** (8), 085005 (2018).
50. C.-Z. Zhao, T. Wei, L.-Y. Chen, S.-S. Wang and J. Wang, Superlattices and Microstructures **109**, 758-762 (2017).
51. C. Stampfl and C. Van de Walle, Physical Review B **65** (15), 155212 (2002).

52. Y. Taniyasu, M. Kasu and N. Kobayashi, Applied physics letters **81** (7), 1255-1257 (2002).
53. T. Al Tahtamouni, A. Sedhain, J. Lin and H. Jiang, Applied Physics Letters **92** (9), 092105 (2008).
54. Y.-H. Liang and E. Towe, Applied Physics Reviews **5** (1), 011107 (2018).
55. Q. Dai, Q. Shan, J. Wang, S. Chhajed, J. Cho, E. F. Schubert, M. H. Crawford, D. D. Koleske, M.-H. Kim and Y. Park, Applied Physics Letters **97** (13), 133507 (2010).
56. J. Yan, J. Wang, Y. Zhang, P. Cong, L. Sun, Y. Tian, C. Zhao and J. Li, Journal of Crystal Growth **414**, 254-257 (2015).
57. H. Hirayama, T. Yatabe, N. Noguchi, T. Ohashi and N. Kamata, physica status solidi c **5** (9), 2969-2971 (2008).
58. R. Jain, W. Sun, J. Yang, M. Shatalov, X. Hu, A. Sattu, A. Lunev, J. Deng, I. Shturm and Y. Bilenko, Applied Physics Letters **93** (5), 051113 (2008).
59. V. Kueller, A. Knauer, F. Brunner, U. Zeimer, H. Rodriguez, M. Kneissl and M. Weyers, Journal of Crystal Growth **315** (1), 200-203 (2011).
60. M. Imura, K. Nakano, G. Narita, N. Fujimoto, N. Okada, K. Balakrishnan, M. Iwaya, S. Kamiyama, H. Amano and I. Akasaki, Journal of crystal growth **298**, 257-260 (2007).
61. S. Heikman, S. Keller, S. Newman, Y. Wu, C. Moe, B. Moran, M. Schmidt, U. K. Mishra, J. S. Speck and S. P. DenBaars, Japanese journal of applied physics **44** (3L), L405 (2005).
62. O. Kovalenkov, V. Soukhoveev, V. Ivantsov, A. Usikov and V. Dmitriev, Journal of crystal growth **281** (1), 87-92 (2005).
63. M. Strassburg, J. Senawiratne, N. Dietz, U. Haboeck, A. Hoffmann, V. Noveski, R. Dalmau, R. Schlesser and Z. Sitar, Journal of Applied Physics **96** (10), 5870-5876 (2004).
64. https://www.ledsmagazine.com/manufacturing-services-testing/research-development/article/16695192/patterned-substrates-enhance-led-light-extraction-magazine.
65. K. Nakano, M. Imura, G. Narita, T. Kitano, Y. Hirose, N. Fujimoto, N. Okada, T. Kawashima, K. Iida and K. Balakrishnan, physica status solidi (a) **203** (7), 1632-1635 (2006).
66. https://www.hexatechinc.com/documents/HexaTech-AlN-30-Datasheet-PD-AlN-30-R004.pdf.
67. S. Zhao, S. Woo, M. Bugnet, X. Liu, J. Kang, G. Botton and Z. Mi, Nano letters **15** (12), 7801-7807 (2015).
68. Y. Liao, C. Thomidis, C.-k. Kao and T. D. Moustakas, Applied Physics Letters **98** (8), 081110 (2011).
69. T. D. Moustakas, MRS Communications **6** (3), 247-269 (2016).
70. T. D. Moustakas and A. Bhattacharyya, physica status solidi c **9** (3-4), 580-583 (2012).
71. D. A. Laleyan, N. Fernández-Delgado, E. T. Reid, P. Wang, A. Pandey, G. A. Botton and Z. Mi, Applied Physics Letters **116** (15), 152102 (2020).
72. S. Xiao, R. Suzuki, H. Miyake, S. Harada and T. Ujihara, Journal of Crystal Growth **502**, 41-44 (2018).
73. H. Miyake, C.-H. Lin, K. Tokoro and K. Hiramatsu, Journal of Crystal Growth **456**, 155-159 (2016).
74. N. Susilo, S. Hagedorn, D. Jaeger, H. Miyake, U. Zeimer, C. Reich, B. Neuschulz, L. Sulmoni, M. Guttmann and F. Mehnke, Applied Physics Letters **112** (4), 041110 (2018).
75. M. Kim, T. Fujita, S. Fukahori, T. Inazu, C. Pernot, Y. Nagasawa, A. Hirano, M. Ippommatsu, M. Iwaya and T. Takeuchi, Applied physics express **4** (9), 092102 (2011).

76. M. Ichikawa, A. Fujioka, T. Kosugi, S. Endo, H. Sagawa, H. Tamaki, T. Mukai, M. Uomoto and T. Shimatsu, Applied Physics Express **9** (7), 072101 (2016).
77. M. Shatalov, W. Sun, A. Lunev, X. Hu, A. Dobrinsky, Y. Bilenko, J. Yang, M. Shur, R. Gaska and C. Moe, Applied Physics Express **5** (8), 082101 (2012).
78. W. Guo, R. Kirste, I. Bryan, Z. Bryan, L. Hussey, P. Reddy, J. Tweedie, R. Collazo and Z. Sitar, Applied Physics Letters **106** (8), 082110 (2015).
79. Z. Li, L. Liu, Y. Huang, Q. Sun, M. Feng, Y. Zhou, H. Zhao and H. Yang, Applied Physics Express **10** (7), 072101 (2017).
80. Y. Zhang, S. Gautier, C.-Y. Cho, E. Cicek, Z. Vashaei, R. McClintock, C. Bayram, Y. Bai and M. Razeghi, Applied Physics Letters **102** (1), 011106 (2013).
81. Y. Kashima, N. Maeda, E. Matsuura, M. Jo, T. Iwai, T. Morita, M. Kokubo, T. Tashiro, R. Kamimura and Y. Osada, Applied Physics Express **11** (1), 012101 (2017).
82. W. Shin, A. Pandey, X. Liu, Y. Sun and Z. Mi, Optics express **27** (26), 38413-38420 (2019).
83. X. Liu, K. Mashooq, D. A. Laleyan, E. T. Reid and Z. Mi, Photonics Research **7** (6), B12-B23 (2019).
84. X. Liu, B. H. Le, S. Y. Woo, S. Zhao, A. Pofelski, G. A. Botton and Z. Mi, Optics express **25** (24), 30494-30502 (2017).
85. P. Zhao, L. Han, M. R. McGoogan and H. Zhao, Optical Materials Express **2** (10), 1397-1406 (2012).
86. S. Zhao, M. Djavid and Z. J. N. l. Mi, **15** (10), 7006-7009 (2015).
87. https://www.shinetsusilicone-global.com/products/usage/led/index.shtml.
88. M. Asad, R. Wang, Y.-H. Ra, P. Gavirneni, Z. Mi and W. S. Wong, npj Flexible Electronics **3** (1), 1-6 (2019).
89. M. Nakarmi, K. Kim, J. Li, J. Lin and H. Jiang, Applied physics letters **82** (18), 3041-3043 (2003).
90. Y. Taniyasu, M. Kasu and T. Makimoto, Nature **441** (7091), 325 (2006).
91. Y. Chen, H. Wu, E. Han, G. Yue, Z. Chen, Z. Wu, G. Wang and H. Jiang, Applied Physics Letters **106** (16), 162102 (2015).
92. W. Luo, B. Liu, Z. Li, L. Li, Q. Yang, L. Pan, C. Li, D. Zhang, X. Dong and D. Peng, Applied Physics Letters **113** (7), 072107 (2018).
93. S. Li, M. Ware, J. Wu, P. Minor, Z. Wang, Z. Wu, Y. Jiang and G. J. Salamo, Applied Physics Letters **101** (12), 122103 (2012).
94. A. Pandey, X. Liu, Z. Deng, W. Shin, D. Laleyan, K. Mashooq, E. Reid, E. Kioupakis, P. Bhattacharya and Z. Mi, Physical Review Materials **3** (5), 053401 (2019).
95. B. So, J. Kim, E. Shin, T. Kwak, T. Kim and O. Nam, physica status solidi (a) **215** (10), 1700677 (2018).
96. L. Li, Y. Zhang, S. Xu, W. Bi, Z.-H. Zhang and H.-C. Kuo, Materials **10** (10), 1221 (2017).
97. Z.-H. Zhang, S.-W. Huang Chen, Y. Zhang, L. Li, S.-W. Wang, K. Tian, C. Chu, M. Fang, H.-C. Kuo and W. Bi, Acs Photonics **4** (7), 1846-1850 (2017).
98. A. Pandey, W. Shin, X. Liu and Z. Mi, Optics Express **27** (12), A738-A745 (2019).
99. Y. Zhang, Z. Jamal-Eddine, F. Akyol, S. Bajaj, J. M. Johnson, G. Calderon, A. A. Allerman, M. W. Moseley, A. M. Armstrong and J. Hwang, Applied Physics Letters **112** (7), 071107 (2018).

100. Y. Zhang, S. Krishnamoorthy, F. Akyol, A. A. Allerman, M. W. Moseley, A. M. Armstrong and S. Rajan, Applied Physics Letters **109** (19), 191105 (2016).
101. Y. Zhang, S. Krishnamoorthy, F. Akyol, J. M. Johnson, A. A. Allerman, M. W. Moseley, A. M. Armstrong, J. Hwang and S. Rajan, Applied Physics Letters **111** (5), 051104 (2017).
102. Y. Zhang, S. Krishnamoorthy, J. M. Johnson, F. Akyol, A. Allerman, M. W. Moseley, A. Armstrong, J. Hwang and S. Rajan, Applied Physics Letters **106** (14), 141103 (2015).
103. A. Pandey, J. Gim, R. Hovden and Z. Mi, Applied Physics Letters **117** (24), 241101 (2020).
104. A. Pandey, W. J. Shin, J. Gim, R. Hovden and Z. Mi, Photonics Research **8** (3), 331-337 (2020).
105. F. Glas, Physical Review B **74** (12), 121302 (2006).
106. Z. Mi, S. Zhao, S. Woo, M. Bugnet, M. Djavid, X. Liu, J. Kang, X. Kong, W. Ji and H. Guo, Journal of Physics D: Applied Physics **49** (36), 364006 (2016).
107. S. Zhao, A. Connie, M. Dastjerdi, X. Kong, Q. Wang, M. Djavid, S. Sadaf, X. Liu, I. Shih and H. Guo, Scientific reports **5** (1), 1-5 (2015).
108. N. H. Tran, B. H. Le, S. Zhao and Z. Mi, Applied Physics Letters **110** (3), 032102 (2017).
109. M. Djavid and Z. Mi, Applied Physics Letters **108** (5), 051102 (2016).
110. S. Zhao, S. Woo, S. Sadaf, Y. Wu, A. Pofelski, D. Laleyan, R. Rashid, Y. Wang, G. Botton and Z. Mi, Apl Materials **4** (8), 086115 (2016).
111. B. Le, X. Liu, N. Tran, S. Zhao and Z. Mi, Optics express **27** (4), 5843-5850 (2019).
112. B. J. May, A. G. Sarwar and R. C. Myers, Applied Physics Letters **108** (14), 141103 (2016).
113. H. Sun, M. K. Shakfa, M. M. Muhammed, B. Janjua, K.-H. Li, R. Lin, T. K. Ng, I. S. Roqan, B. S. Ooi and X. Li, ACS Photonics **5** (3), 964-970 (2017).
114. H. P. T. Nguyen, M. Djavid, S. Y. Woo, X. Liu, A. T. Connie, S. Sadaf, Q. Wang, G. A. Botton, I. Shih and Z. Mi, Scientific reports **5** (1), 1-7 (2015).
115. T. Moustakas, E. Iliopoulos, A. Sampath, H. Ng, D. Doppalapudi, M. Misra, D. Korakakis and R. Singh, Journal of crystal growth **227**, 13-20 (2001).
116. H. M. Ng, D. Doppalapudi, D. Korakakis, R. Singh and T. D. Moustakas, Journal of crystal growth **189**, 349-353 (1998).
117. H. Morkoç, Journal of Materials Science: Materials in Electronics **12** (12), 677-695 (2001).
118. C. Foxon, Journal of Vacuum Science & Technology B: Microelectronics Processing and Phenomena **1** (2), 293-297 (1983).
119. S.-K. Jerng, K. Joo, Y. Kim, S.-M. Yoon, J. H. Lee, M. Kim, J. S. Kim, E. Yoon, S.-H. Chun and Y. S. Kim, Nanoscale **5** (21), 10618-10622 (2013).
120. N. Bansal, M. R. Cho, M. Brahlek, N. Koirala, Y. Horibe, J. Chen, W. Wu, Y. D. Park and S. Oh, Nano letters **14** (3), 1343-1348 (2014).
121. H. Ibach and H. Lüth, *Solid-state physics: an introduction to theory and experiment*. (Springer Science & Business Media, 2012).
122. https://www.staibinstruments.com/products/rheed/.
123. https://www.staibinstruments.com/products/rheed/#iLightbox[image_carousel_1]/0.
124. J. G. Amar and F. Family, MRS Online Proceedings Library (OPL) **367** (1994).
125. W. P. McCray, Nature nanotechnology **2** (5), 259-261 (2007).
126. J. Singh, S. Dudley, B. Davies and K. Bajaj, Journal of applied physics **60** (9), 3167-3171 (1986).

127. M. Volmer and A. Weber, Zeitschrift für physikalische Chemie **119** (1), 277-301 (1926).
128. I. N. Stranski and L. Krastanow, Monatshefte für Chemie und verwandte Teile anderer Wissenschaften **71** (1), 351-364 (1937).
129. F. C. Frank and J. H. van der Merwe, Proceedings of the Royal Society of London. Series A. Mathematical and Physical Sciences **198** (1053), 205-216 (1949).
130. D. Mishra, D. Greving, G. B. Confalonieri, J. Perlich, B. Toperverg, H. Zabel and O. Petracic, Nanotechnology **25** (20), 205602 (2014).
131. O. Landré, V. Fellmann, P. Jaffrennou, C. Bougerol, H. Renevier, A. Cros and B. Daudin, Applied Physics Letters **96** (6), 061912 (2010).
132. S. Deshpande, T. Frost, L. Yan, S. Jahangir, A. Hazari, X. Liu, J. Mirecki-Millunchick, Z. Mi and P. Bhattacharya, Nano letters **15** (3), 1647-1653 (2015).
133. C. Bayram and M. Razeghi, Applied Physics A **96** (2), 403-408 (2009).
134. C. Adelmann, J. Simon, N. Pelekanos, Y. Samson, G. Feuillet and B. Daudin, physica status solidi (a) **176** (1), 639-642 (1999).
135. C. Adelmann, J. Simon, G. Feuillet, N. Pelekanos, B. Daudin and G. Fishman, Applied Physics Letters **76** (12), 1570-1572 (2000).
136. T. Yamaguchi, S. Einfeldt, S. Figge, C. Kruse, C. Roder and D. Hommel, MRS Online Proceedings Library **831** (1), 323-328 (2004).
137. F. Widmann, B. Daudin, G. Feuillet, Y. Samson, J. Rouviere and N. Pelekanos, Journal of Applied Physics **83** (12), 7618-7624 (1998).
138. M. Zhang, P. Bhattacharya and W. Guo, Applied Physics Letters **97** (1), 011103 (2010).
139. T. Frost, A. Hazari, A. Aiello, M. Z. Baten, L. Yan, J. Mirecki-Millunchick and P. Bhattacharya, Japanese Journal of Applied Physics **55** (3), 032101 (2016).
140. A. C. Espenlaub, D. J. Myers, E. C. Young, S. Marcinkevičius, C. Weisbuch and J. S. Speck, Journal of Applied Physics **126** (18), 184502 (2019).
141. D. J. Myers, A. C. Espenlaub, K. Gelzinyte, E. C. Young, L. Martinelli, J. Peretti, C. Weisbuch and J. S. Speck, Applied Physics Letters **116** (9), 091102 (2020).
142. B. P. Gunning, E. A. Clinton, J. J. Merola, W. A. Doolittle and R. C. Bresnahan, Journal of Applied Physics **118** (15), 155302 (2015).
143. T. D. Moustakas, Y. Liao, C.-k. Kao, C. Thomidis, A. Bhattacharyya, D. Bhattarai and A. Moldawer, presented at the Light-Emitting Diodes: Materials, Devices, and Applications for Solid State Lighting XVI, 2012 (unpublished).
144. T. D. J. M. C. Moustakas, **6** (3), 247-269 (2016).
145. M. A. Herman and H. Sitter, *Molecular beam epitaxy: fundamentals and current status*. (Springer Science & Business Media, 2012).
146. K. K. Min, P. S. Win, H. M. Tun, Z. M. Naing and W. K. Moe, Optics **7** (1), 38-42 (2018).
147. https://www.jawoollam.com/resources/ellipsometry-tutorial.
148. https://serc.carleton.edu/research_education/geochemsheets/BraggsLaw.html.
149. http://hyperphysics.phy-astr.gsu.edu/hbase/magnetic/Hall.html.
150. A. Raman, S. Dasgupta, S. Rajan, J. S. Speck and U. K. Mishra, Japanese Journal of Applied Physics **47** (5R), 3359 (2008).
151. R. Kaplar, A. A. Allerman, A. Armstrong, M. H. Crawford, J. R. Dickerson, A. J. Fischer, A. Baca and E. Douglas, ECS Journal of Solid State Science and Technology **6** (2), Q3061 (2016).

152. S.-i. Inoue, N. Tamari and M. Taniguchi, Applied Physics Letters **110** (14), 141106 (2017).
153. K. Li, X. Liu, Q. Wang, S. Zhao and Z. Mi, Nature nanotechnology **10** (2), 140 (2015).
154. C. Stampfl and C. G. Van de Walle, Applied physics letters **72** (4), 459-461 (1998).
155. U. Kaufmann, P. Schlotter, H. Obloh, K. Köhler and M. Maier, Physical Review B **62** (16), 10867 (2000).
156. M. Nakarmi, N. Nepal, C. Ugolini, T. Altahtamouni, J. Lin and H. Jiang, Applied Physics Letters **89** (15), 152120 (2006).
157. K. Ebata, J. Nishinaka, Y. Taniyasu and K. Kumakura, Japanese Journal of Applied Physics **57** (4S), 04FH09 (2018).
158. T. Zheng, W. Lin, R. Liu, D. Cai, J. Li, S. Li and J. Kang, Scientific reports **6** (1), 1-10 (2016).
159. P. Kozodoy, M. Hansen, S. P. DenBaars and U. K. Mishra, Applied Physics Letters **74** (24), 3681-3683 (1999).
160. M. Nakarmi, K. Kim, M. Khizar, Z. Fan, J. Lin and H. Jiang, Applied Physics Letters **86** (9), 092108 (2005).
161. K. Kumakura and N. Kobayashi, Japanese journal of applied physics **38** (9A), L1012 (1999).
162. A. Allerman, M. Crawford, M. Miller and S. Lee, Journal of crystal growth **312** (6), 756-761 (2010).
163. M. Suzuki, J. Nishio, M. Onomura and C. Hongo, Journal of crystal growth **189**, 511-515 (1998).
164. H. Yu, E. Ulker and E. Ozbay, Journal of crystal growth **289** (2), 419-422 (2006).
165. A. Kakanakova-Georgieva, D. Nilsson, M. Stattin, U. Forsberg, Å. Haglund, A. Larsson and E. Janzén, physica status solidi (RRL)–Rapid Research Letters **4** (11), 311-313 (2010).
166. M. Kauser, A. Osinsky, A. Dabiran and P. Chow, Applied physics letters **85** (22), 5275-5277 (2004).
167. J. Kim, E. Waldron, Y.-L. Li, T. Gessmann, E. Schubert, H. Jang and J.-L. Lee, Applied physics letters **84** (17), 3310-3312 (2004).
168. I. Goepfert, E. Schubert, A. Osinsky, P. Norris and N. Faleev, Journal of Applied Physics **88** (4), 2030-2038 (2000).
169. S. A. Nikishin, M. Holtz and H. Temkin, Japanese journal of applied physics **44** (10R), 7221 (2005).
170. B. Gunning, J. Lowder, M. Moseley and W. Alan Doolittle, Applied Physics Letters **101** (8), 082106 (2012).
171. M. Brandt, N. Johnson, R. Molnar, R. Singh and T. Moustakas, Applied Physics Letters **64** (17), 2264-2266 (1994).
172. M. Nakarmi, N. Nepal, J. Lin and H. Jiang, Applied Physics Letters **94** (9), 091903 (2009).
173. C. G. Van de Walle, C. Stampfl and J. Neugebauer, Journal of crystal growth **189**, 505-510 (1998).
174. C. G. Van de Walle and J. Neugebauer, Journal of applied physics **95** (8), 3851-3879 (2004).
175. Y. Liang and E. Towe, Journal of Applied Physics **123** (9), 095303 (2018).
176. A. Bhattacharyya, W. Li, J. Cabalu, T. Moustakas, D. J. Smith and R. Hervig, Applied physics letters **85** (21), 4956-4958 (2004).

177. E. Iliopoulos and T. Moustakas, Applied physics letters **81** (2), 295-297 (2002).
178. W. Hoke, A. Torabi, J. Mosca and T. Kennedy, Journal of Vacuum Science & Technology B: Microelectronics and Nanometer Structures Processing, Measurement, and Phenomena **25** (3), 978-982 (2007).
179. A. Tian, J. Liu, M. Ikeda, S. Zhang, Z. Li, M. Feng, K. Zhou, D. Li, L. Zhang and P. Wen, Applied Physics Express **8** (5), 051001 (2015).
180. N. H. Tran, B. H. Le, S. Zhao and Z. Mi, Applied Physics Letters **110** (3), 032102 (2017).
181. C. G. Van de Walle and D. Segev, Journal of Applied Physics **101** (8), 081704 (2007).
182. J. E. Northrup and J. Neugebauer, Physical Review B **53** (16), R10477 (1996).
183. M. Crawford, Semiconductors and Semimetals **96**, 3-44 (2017).
184. K. Takeda, M. Iwaya, T. Takeuchi, S. Kamiyama and I. Akasaki, Japanese Journal of Applied Physics **55** (5S), 05FE02 (2016).
185. R. Collazo, S. Mita, J. Xie, A. Rice, J. Tweedie, R. Dalmau and Z. Sitar, physica status solidi (c) **8** (7-8), 2031-2033 (2011).
186. E. F. Schubert, T. Gessmann and J. K. Kim, Kirk-Othmer Encyclopedia of Chemical Technology (2000).
187. Z. Liu, J. Ma, X. Yi, E. Guo, L. Wang, J. Wang, N. Lu, J. Li, I. Ferguson and A. Melton, Applied Physics Letters **101** (26), 261106 (2012).
188. C. S. Xia, Z. S. Li, W. Lu, Z. H. Zhang, Y. Sheng, W. D. Hu and L. W. Cheng, Journal of Applied Physics **111** (9), 094503 (2012).
189. G. Alahyarizadeh, M. Amirhoseiny and Z. Hassan, Optics & Laser Technology **76**, 106-112 (2016).
190. S.-H. Han, D.-Y. Lee, S.-J. Lee, C.-Y. Cho, M.-K. Kwon, S. Lee, D. Noh, D.-J. Kim, Y. C. Kim and S.-J. Park, Applied Physics Letters **94** (23), 231123 (2009).
191. Y. Ji, Z.-H. Zhang, Z. Kyaw, S. Tiam Tan, Z. Gang Ju, X. Liang Zhang, W. Liu, X. Wei Sun and H. Volkan Demir, Applied Physics Letters **103** (5), 053512 (2013).
192. Z.-H. Zhang, Y. Ji, W. Liu, S. Tiam Tan, Z. Kyaw, Z. Ju, X. Zhang, N. Hasanov, S. Lu and Y. Zhang, Applied Physics Letters **104** (7), 073511 (2014).
193. H. Hirayama, Y. Tsukada, T. Maeda and N. Kamata, Applied Physics Express **3** (3), 031002 (2010).
194. T. Kolbe, A. Knauer, J. Rass, H. K. Cho, S. Hagedorn, S. Einfeldt, M. Kneissl and M. Weyers, Materials **10** (12), 1396 (2017).
195. D. A. Laleyan, X. Liu, A. Pandey, W. J. Shin, E. T. Reid, K. Mashooq, M. Soltani and Z. Mi, Journal of Crystal Growth **507**, 87-92 (2019).
196. A. Aiello, A. Pandey, A. Bhattacharya, J. Gim, X. Liu, D. A. Laleyan, R. Hovden, Z. Mi and P. Bhattacharya, Journal of Crystal Growth **508**, 66-71 (2019).
197. http://my.ece.ucsb.edu/mgrundmann/bandeng.htm.
198. N. Maeda, M. Jo and H. Hirayama, Physica Status Solidi (a) **215** (8), 1700435 (2018).
199. S.-H. Yen, M.-C. Tsai, M.-L. Tsai, Y.-J. Shen, T.-C. Hsu and Y.-K. Kuo, IEEE Photonics Technology Letters **21** (14), 975-977 (2009).
200. A. Chitnis, J. Sun, V. Mandavilli, R. Pachipulusu, S. Wu, M. Gaevski, V. Adivarahan, J. Zhang, M. A. Khan and A. Sarua, Applied Physics Letters **81** (18), 3491-3493 (2002).
201. J. Iveland, L. Martinelli, J. Peretti, J. S. Speck and C. Weisbuch, Physical review letters **110** (17), 177406 (2013).
202. E. Kioupakis, P. Rinke, K. T. Delaney and C. G. Van de Walle, Applied Physics Letters **98** (16), 161107 (2011).

203. F. Nippert, M. Tollabi Mazraehno, M. J. Davies, M. P. Hoffmann, H.-J. Lugauer, T. Kure, M. Kneissl, A. Hoffmann and M. R. Wagner, Applied Physics Letters **113** (7), 071107 (2018).
204. Y. Li, Y. Gao, M. He, J. Zhou, Y. Lei, L. Zhang, K. Zhu and Y. Chen, Journal of Display Technology **9** (4), 244-248 (2013).
205. in *Global Guidelines for the Prevention of Surgical Site Infection* (World Health Organization, Geneva, 2018).
206. in *Guidelines for Drinking-Water Quality: Fourth Edition Incorporating the First Addendum* (World Health Organization, Geneva, 2017).
207. J. Shakya, K. Knabe, K. Kim, J. Li, J. Lin and H. Jiang, Applied Physics Letters **86** (9), 091107 (2005).
208. M. Guttmann, F. Mehnke, B. Belde, F. Wolf, C. Reich, L. Sulmoni, T. Wernicke and M. Kneissl, Japanese Journal of Applied Physics **58** (SC), SCCB20 (2019).
209. J. Northrup, C. Chua, Z. Yang, T. Wunderer, M. Kneissl, N. Johnson and T. Kolbe, Applied Physics Letters **100** (2), 021101 (2012).
210. H. Hirayama, S. Fujikawa, N. Noguchi, J. Norimatsu, T. Takano, K. Tsubaki and N. Kamata, physica status solidi (a) **206** (6), 1176-1182 (2009).
211. V. Mymrin, K. Bulashevich, N. Podolskaya and S. Y. Karpov, Journal of Crystal Growth **281** (1), 115-124 (2005).
212. M. S. Shur and R. Gaska, IEEE Transactions on Electron Devices **57** (1), 12-25 (2009).
213. Y. Kashima, N. Maeda, E. Matsuura, M. Jo, T. Iwai, T. Morita, M. Kokubo, T. Tashiro, R. Kamimura, Y. Osada, H. Takagi and H. Hirayama, Applied Physics Express **11** (1) (2018).
214. S. Zhao, H. P. Nguyen, M. G. Kibria and Z. Mi, Progress in Quantum Electronics **44**, 14-68 (2015).
215. P. Dong, J. Yan, J. Wang, Y. Zhang, C. Geng, T. Wei, P. Cong, Y. Zhang, J. Zeng, Y. Tian, L. Sun, Q. Yan, J. Li, S. Fan and Z. Qin, Applied Physics Letters **102** (24), 241113 (2013).
216. H. Hirayama, T. Yatabe, N. Noguchi, T. Ohashi and N. Kamata, Applied Physics Letters **91** (7), 071901 (2007).
217. N. Susilo, S. Hagedorn, D. Jaeger, H. Miyake, U. Zeimer, C. Reich, B. Neuschulz, L. Sulmoni, M. Guttmann, F. Mehnke, C. Kuhn, T. Wernicke, M. Weyers and M. Kneissl, Applied Physics Letters **112** (4), 041110 (2018).
218. J. Zhang, X. Hu, Y. Bilenko, J. Deng, A. Lunev, M. Shur, R. Gaska, M. Shatalov, J. Yang and M. A. Khan, Applied Physics Letters **85** (23), 5532-5534 (2004).
219. S. Vilhunen, H. Särkkä and M. Sillanpää, Environmental Science and Pollution Research **16** (4), 439-442 (2009).
220. S.-i. Inoue, T. Naoki, T. Kinoshita, T. Obata and H. Yanagi, Applied Physics Letters **106** (13), 131104 (2015).
221. G.-D. Hao, N. Tamari, T. Obata, T. Kinoshita and S.-i. Inoue, Optics Express **25** (16), A639-A648 (2017).
222. Y. Liao, C. Kao, C. Thomidis, A. Moldawer, J. Woodward, D. Bhattarai and T. Moustakas, Physica Status Solidi (c) **9** (3-4), 798-801 (2012).
223. G.-B. Lin, D. Meyaard, J. Cho, E. Fred Schubert, H. Shim and C. Sone, Applied Physics Letters **100** (16), 161106 (2012).
224. J. Zhang, Y. Zhu, T. Egawa, S. Sumiya, M. Miyoshi and M. Tanaka, Applied Physics Letters **92** (19), 191917 (2008).

225. A. Chitnis, J. Sun, V. Mandavilli, R. Pachipulusu, S. Wu, M. Gaevski, V. Adivarahan, J. Zhang, M. A. Khan, A. Sarua and M. Kuball, Applied Physics Letters **81** (18), 3491-3493 (2002).
226. J. Yun, J.-I. Shim and H. Hirayama, Applied Physics Express **8** (2), 022104 (2015).
227. W. Sun, M. Shatalov, J. Deng, X. Hu, J. Yang, A. Lunev, Y. Bilenko, M. Shur and R. Gaska, Applied Physics Letters **96** (6), 061102 (2010).
228. H. Hirayama, N. Maeda, S. Fujikawa, S. Toyoda and N. Kamata, Japanese Journal of Applied Physics **53** (10), 100209 (2014).
229. Y. Zhang, Z. Jamal-Eddine, F. Akyol, S. Bajaj, J. M. Johnson, G. Calderon, A. A. Allerman, M. W. Moseley, A. M. Armstrong, J. Hwang and S. Rajan, Applied Physics Letters **112** (7), 071107 (2018).
230. Y. Zhang, S. Krishnamoorthy, F. Akyol, S. Bajaj, A. A. Allerman, M. W. Moseley, A. M. Armstrong and S. Rajan, Applied Physics Letters **110** (20), 201102 (2017).
231. F. Akyol, S. Krishnamoorthy, Y. Zhang, J. Johnson, J. Hwang and S. Rajan, Applied Physics Letters **108** (13), 131103 (2016).
232. E. A. Clinton, E. Vadiee, S.-C. Shen, K. Mehta, P. D. Yoder and W. A. Doolittle, Applied Physics Letters **112** (25), 252103 (2018).
233. Z.-H. Zhang, S. Tiam Tan, Z. Kyaw, Y. Ji, W. Liu, Z. Ju, N. Hasanov, X. Wei Sun and H. Volkan Demir, Applied Physics Letters **102** (19), 193508 (2013).
234. T. Takeuchi, G. Hasnain, S. Corzine, M. Hueschen, R. P. Schneider Jr, C. Kocot, M. Blomqvist, Y.-l. Chang, D. Lefforge and M. R. Krames, Japanese Journal of Applied Physics **40** (8B), L861 (2001).
235. S. Lee, C. A. Forman, C. Lee, J. Kearns, E. C. Young, J. T. Leonard, D. A. Cohen, J. S. Speck, S. Nakamura and S. P. DenBaars, Applied Physics Express **11** (6), 062703 (2018).
236. C. Kuhn, L. Sulmoni, M. Guttmann, J. Glaab, N. Susilo, T. Wernicke, M. Weyers and M. Kneissl, Photonics Research **7** (5), B7-B11 (2019).
237. Y. Zhang, S. Krishnamoorthy, F. Akyol, A. A. Allerman, M. W. Moseley, A. M. Armstrong and S. Rajan, Applied Physics Letters **109** (12), 121102 (2016).
238. M. Auf der Maur, B. Galler, I. Pietzonka, M. Strassburg, H. Lugauer and A. Di Carlo, Applied Physics Letters **105** (13), 133504 (2014).
239. X. Cao, E. Stokes, P. Sandvik, S. LeBoeuf, J. Kretchmer and D. Walker, IEEE Electron Device Letters **23** (9), 535-537 (2002).
240. C. Bayram, Z. Vashaei and M. Razeghi, Applied Physics Letters **97** (18), 181109 (2010).
241. V. Fan Arcara, B. Damilano, G. Feuillet, S. Vézian, K. Ayadi, S. Chenot and J.-Y. Duboz, Journal of Applied Physics **126** (22), 224503 (2019).
242. E. Vadiee, E. A. Clinton, H. McFavilen, A. S. Weidenbach, Z. Engel, C. Matthews, C. Zhang, C. Arena, R. R. King and C. B. Honsberg, Applied Physics Express **11** (8), 082304 (2018).
243. E. C. Young, B. P. Yonkee, F. Wu, S. H. Oh, S. P. DenBaars, S. Nakamura and J. S. Speck, Applied Physics Express **9** (2), 022102 (2016).
244. Y.-J. Lee, C.-H. Chen and C.-J. Lee, IEEE Photonics Technology Letters **22** (20), 1506-1508 (2010).
245. J. Piprek, Physica Status Solidi (a) **207** (10), 2217-2225 (2010).
246. M.-H. Kim, M. F. Schubert, Q. Dai, J. K. Kim, E. F. Schubert, J. Piprek and Y. Park, Applied Physics Letters **91** (18), 183507 (2007).

247. X. Hai, R. Rashid, S. Sadaf, Z. Mi and S. Zhao, Applied Physics Letters **114** (10), 101104 (2019).
248. D. S. Meyaard, G.-B. Lin, Q. Shan, J. Cho, E. Fred Schubert, H. Shim, M.-H. Kim and C. Sone, Applied Physics Letters **99** (25), 251115 (2011).
249. A. Bhattacharyya, T. Moustakas, L. Zhou, D. J. Smith and W. Hug, Applied Physics Letters **94** (18), 181907 (2009).
250. Y. Wang, A. S. Özcan, K. F. Ludwig Jr, A. Bhattacharyya, T. Moustakas, L. Zhou and D. J. Smith, Applied physics letters **88** (18), 181915 (2006).
251. O. Ambacher, B. Foutz, J. Smart, J. Shealy, N. Weimann, K. Chu, M. Murphy, A. Sierakowski, W. Schaff, L. Eastman, R. Dimitrov, A. Mitchell and M. Stutzmann, Journal of Applied Physics **87** (1), 334-344 (2000).
252. Y. Gu, N. Narendran, T. Dong and H. Wu, presented at the Sixth International Conference on Solid State Lighting, 2006 (unpublished).
253. J. Cho, E. F. Schubert and J. K. Kim, Laser Photonics Reviews **7** (3), 408-421 (2013).
254. S. Karpov, Optical Quantum Electronics **47** (6), 1293-1303 (2015).
255. V. M. Gomez-Lopez, P. Ragaert, J. Debevere and F. Devlieghere, Trends in food science & technology **18** (9), 464-473 (2007).
256. T. Dai, M. S. Vrahas, C. K. Murray and M. R. Hamblin, Expert review of anti-infective therapy **10** (2), 185-195 (2012).
257. M. Buonanno, D. Welch, I. Shuryak and D. J. Brenner, Scientific Reports **10** (1), 10285 (2020).
258. M. Raeiszadeh and B. Adeli, ACS Photonics **7** (11), 2941-2951 (2020).
259. V. Adivarahan, W. H. Sun, A. Chitnis, M. Shatalov, S. Wu, H. Maruska and M. A. Khan, Applied physics letters **85** (12), 2175-2177 (2004).
260. C. Pernot, S. Fukahori, T. Inazu, T. Fujita, M. Kim, Y. Nagasawa, A. Hirano, M. Ippommatsu, M. Iwaya and S. Kamiyama, physica status solidi (a) **208** (7), 1594-1596 (2011).
261. A. Fujioka, K. Asada, H. Yamada, T. Ohtsuka, T. Ogawa, T. Kosugi, D. Kishikawa and T. Mukai, Semiconductor Science and Technology **29** (8), 084005 (2014).
262. C. Pernot, M. Kim, S. Fukahori, T. Inazu, T. Fujita, Y. Nagasawa, A. Hirano, M. Ippommatsu, M. Iwaya and S. Kamiyama, Applied physics express **3** (6), 061004 (2010).
263. J. L. Lyons, A. Janotti and C. G. Van de Walle, Physical review letters **108** (15), 156403 (2012).
264. J. Piprek, physica status solidi (a) **207** (10), 2217-2225 (2010).
265. J. Cho, E. F. Schubert and J. K. Kim, Laser & Photonics Reviews **7** (3), 408-421 (2013).
266. C. Frankerl, F. Nippert, A. Gomez-Iglesias, M. P. Hoffmann, C. Brandl, H.-J. Lugauer, R. Zeisel, A. Hoffmann and M. J. Davies, Applied Physics Letters **117** (10), 102107 (2020).
267. J. Mickevičius, G. Tamulaitis, M. Shur, M. Shatalov, J. Yang and R. Gaska, Applied Physics Letters **101** (21), 211902 (2012).
268. J. Mickevičius, G. Tamulaitis, M. Shur, M. Shatalov, J. Yang and R. Gaska, Applied Physics Letters **103** (1), 011906 (2013).
269. S. Zhao, S. Sadaf, S. Vanka, Y. Wang, R. Rashid and Z. Mi, Applied Physics Letters **109** (20), 201106 (2016).
270. S. Sadaf, S. Zhao, Y. Wu, Y.-H. Ra, X. Liu, S. Vanka and Z. Mi, Nano letters **17** (2), 1212-1218 (2017).
271. S. Bharadwaj, K. Lee, S. M. Islam, V. Protasenko, H. G. Xing and D. Jena, in *2017 Conference on Lasers and Electro-Optics (CLEO)* (2017), pp. 1-2.

272. L. Sang, M. Liao, N. Ikeda, Y. Koide and M. Sumiya, Applied Physics Letters **99** (16), 161109 (2011).
273. Y. Wu, D. A. Laleyan, Z. Deng, C. Ahn, A. F. Aiello, A. Pandey, X. Liu, P. Wang, K. Sun, E. Ahmadi, Y. Sun, M. Kira, P. Bhattacharya, E. Kioupakis and Z. Mi, Advanced Electronic Materials **6** (9), 2000337 (2020).
274. V. N. Jmerik, D. V. Nechaev, S. Rouvimov, V. V. Ratnikov, P. S. Kop'ev, M. V. Rzheutski, E. V. Lutsenko, G. P. Yablonskii, M. Aljohenii and A. Aljerwii, Journal of Materials Research **30** (19), 2871 (2015).
275. V. Jmerik, E. Lutsenko and S. Ivanov, physica status solidi (a) **210** (3), 439-450 (2013).
276. V. Y. Davydov, V. Jmerik, E. Roginskii, Y. E. Kitaev, Y. Beltukov, M. Smirnov, D. Nechaev, A. Smirnov, I. Eliseyev and P. Brunkov, Semiconductors **53** (11), 1479-1488 (2019).
277. E. Iliopoulos, K. Ludwig Jr and T. Moustakas, Journal of Physics and Chemistry of Solids **64** (9-10), 1525-1532 (2003).
278. S. J. Kim and T. G. Kim, physica status solidi (a) **211** (3), 656-660 (2014).
279. M.-C. Tsai, S.-H. Yen, Y.-C. Lu and Y.-K. Kuo, IEEE Photonics Technology Letters **23** (2), 76-78 (2010).
280. D. Jena, J. Simon, A. Wang, Y. Cao, K. Goodman, J. Verma, S. Ganguly, G. Li, K. Karda and V. Protasenko, physica status solidi (a) **208** (7), 1511-1516 (2011).
281. H. Okumura, K. Balakrishnan, H. Hamaguchi, T. Koizumi, S. Chichibu, H. Nakanishi, T. Nagatomo and S. Yoshida, Journal of crystal growth **189**, 364-369 (1998).
282. H.-H. Chen, J. S. Speck, C. Weisbuch and Y.-R. Wu, Applied Physics Letters **113** (15), 153504 (2018).
283. K. Lee, P. Parbrook, T. Wang, J. Bai, F. Ranalli, R. Airey and G. Hill, physica status solidi (b) **247** (7), 1761-1763 (2010).
284. K. Mayes, A. Yasan, R. McClintock, D. Shiell, S. Darvish, P. Kung and M. Razeghi, Applied physics letters **84** (7), 1046-1048 (2004).
285. K. Lee, P. Parbrook, T. Wang, J. Bai, F. Ranalli, R. Airey and G. Hill, Journal of crystal growth **311** (10), 2857-2859 (2009).
286. P. G. Eliseev, P. Perlin, J. Lee and M. Osiński, Applied physics letters **71** (5), 569-571 (1997).
287. A. Bell, S. Srinivasan, C. Plumlee, H. Omiya, F. Ponce, J. Christen, S. Tanaka, A. Fujioka and Y. Nakagawa, Journal of applied physics **95** (9), 4670-4674 (2004).
288. B. Manuela, D. Welch, S. Igor and D. J. Brenner, Scientific Reports (Nature Publisher Group) **10** (1) (2020).
289. Y. Nagasawa and A. Hirano, Applied Sciences **8** (8), 1264 (2018).
290. A. Khan, K. Balakrishnan and T. Katona, Nature photonics **2** (2), 77-84 (2008).
291. H. Hirayama, S. Fujikawa and N. Kamata, Electronics and Communications in Japan **98** (5), 1-8 (2015).
292. S. Bharadwaj, K. Lee, S. Islam, V. Protasenko, H. G. Xing and D. Jena, presented at the CLEO: Science and Innovations, 2017 (unpublished).
293. R. Collazo, S. Mita, J. Xie, A. Rice, J. Tweedie, R. Dalmau and Z. Sitar, physica status solidi c **8** (7-8), 2031-2033 (2011).
294. B. Sarkar, S. Washiyama, M. H. Breckenridge, A. Klump, J. N. Baker, P. Reddy, J. Tweedie, S. Mita, R. Kirste and D. L. Irving, ECS Transactions **86** (12), 25 (2018).
295. C. Chu, K. Tian, J. Che, H. Shao, J. Kou, Y. Zhang, Z.-H. Zhang and H.-C. Kuo, IEEE Photonics Journal **12** (3), 1-7 (2020).

296. Y. Liao, C. Thomidis, C.-k. Kao and T. D. J. A. P. L. Moustakas, **98** (8), 081110 (2011).
297. Y.-H. Liang, N. T. Nuhfer and E. Towe, Journal of Vacuum Science & Technology B, Nanotechnology and Microelectronics: Materials, Processing, Measurement, and Phenomena **34** (2), 02L112 (2016).
298. N. Bochkareva, V. Voronenkov, R. Gorbunov, A. Zubrilov, Y. S. Lelikov, P. Latyshev, Y. Rebane, A. Tsyuk and Y. Shreter, Applied Physics Letters **96** (13), 133502 (2010).
299. J. M. Shah, Y.-L. Li, T. Gessmann and E. F. Schubert, Journal of applied physics **94** (4), 2627-2630 (2003).
300. T. Kolbe, A. Knauer, C. Chua, Z. Yang, S. Einfeldt, P. Vogt, N. M. Johnson, M. Weyers and M. Kneissl, Applied Physics Letters **97** (17), 171105 (2010).
301. C. Reich, M. Guttmann, M. Feneberg, T. Wernicke, F. Mehnke, C. Kuhn, J. Rass, M. Lapeyrade, S. Einfeldt and A. Knauer, Applied Physics Letters **107** (14), 142101 (2015).
302. J. Kim, C. Bayram, H. Park, C.-W. Cheng, C. Dimitrakopoulos, J. A. Ott, K. B. Reuter, S. W. Bedell and D. K. Sadana, Nature communications **5** (1), 1-7 (2014).
303. W. Wong, T. Sands, N. Cheung, M. Kneissl, D. Bour, P. Mei, L. Romano and N. Johnson, Applied physics letters **75** (10), 1360-1362 (1999).
304. W. Guo, M. Zhang, P. Bhattacharya and J. Heo, Nano Letters **11** (4), 1434-1438 (2011).
305. Y. Shen, G. Mueller, S. Watanabe, N. Gardner, A. Munkholm and M. Krames, Applied Physics Letters **91** (14), 141101 (2007).
306. R. Chen, Journal of luminescence **102**, 510-518 (2003).
307. C. Collins, A. Sampath, G. Garrett, W. Sarney, H. Shen, M. Wraback, A. Y. Nikiforov, G. Cargill III and V. Dierolf, Applied Physics Letters **86** (3), 031916 (2005).
308. R. Hui and M. O'Sullivan, *Fiber optic measurement techniques*. (Academic Press, 2009).
309. A. Aiello, Y. Wu, A. Pandey, P. Wang, W. Lee, D. Bayerl, N. Sanders, Z. Deng, J. Gim and K. Sun, Nano Letters **19** (11), 7852-7858 (2019).
310. Y. Park, S. Jahangir, Y. Park, P. Bhattacharya and J. Heo, Optics express **23** (11), A650-A656 (2015).
311. A. Prabaswara, J.-W. Min, C. Zhao, B. Janjua, D. Zhang, A. M. Albadri, A. Y. Alyamani, T. K. Ng and B. S. Ooi, Nanoscale research letters **13** (1), 1-9 (2018).
312. X. Yin and S. Zhao, physica status solidi (b), 2000287 (2020).
313. J. Verma, J. Simon, V. Protasenko, T. Kosel, H. Grace Xing and D. Jena, Applied Physics Letters **99** (17), 171104 (2011).
314. H. Tao, S. Xu, J. Zhang, P. Li, Z. Lin and Y. Hao, IEEE Transactions on Electron Devices **66** (1), 478-484 (2018).
315. G. Deng, Y. Zhang, Y. Yu, L. Yan, P. Li, X. Han, L. Chen, D. Zhao and G. Du, Journal of Materials Science: Materials in Electronics **29** (11), 9321-9325 (2018).
316. Z. Zhuang, D. Iida and K. Ohkawa, Optics Express **28** (21), 30423-30431 (2020).
317. M. D. Brubaker, K. L. Genter, A. Roshko, P. T. Blanchard, B. T. Spann, T. E. Harvey and K. A. Bertness, Nanotechnology **30** (23), 234001 (2019).
318. K. Chung, C.-H. Lee and G.-C. Yi, Science **330** (6004), 655-657 (2010).
319. P. Wang, A. Pandey, J. Gim, W. J. Shin, E. T. Reid, D. A. Laleyan, Y. Sun, D. Zhang, Z. Liu and Z. Zhong, Applied Physics Letters **116** (17), 171905 (2020).
320. F. Sánchez, F. Calle, M. Sanchez-Garcia, E. Calleja, E. Muñoz, C. Molloy, D. Somerford, F. Koschnick, K. Michael and J.-M. Spaeth, Materials Research Society Internet Journal of Nitride Semiconductor Research **3** (1998).

321. C. Ronning, E. Carlson, D. Thomson and R. Davis, Applied physics letters **73** (12), 1622-1624 (1998).
322. O. Brandt, H. Yang, H. Kostial and K. H. Ploog, Applied physics letters **69** (18), 2707-2709 (1996).
323. C. G. Van de Walle, S. Limpijumnong and J. Neugebauer, Physical Review B **63** (24), 245205 (2001).
324. A. Sedhain, T. Al Tahtamouni, J. Li, J. Lin and H. Jiang, Applied Physics Letters **93** (14), 141104 (2008).
325. R. Wu, L. Shen, M. Yang, Z.-D. Sha, Y. Cai, Y. P. Feng, Z. Huang and Q. Y. Wu, Applied Physics Letters **91** (15), 152110 (2007).
326. P. Bhattacharya, S. Ghosh, S. Pradhan, J. Singh, Z.-K. Wu, J. Urayama, K. Kim and T. B. Norris, IEEE Journal of Quantum Electronics **39** (8), 952-962 (2003).
327. J. Heyd, G. E. Scuseria and M. Ernzerhof, The Journal of chemical physics **118** (18), 8207-8215 (2003).
328. P. E. Blöchl, Physical review B **50** (24), 17953 (1994).
329. G. Kresse and D. Joubert, Physical review b **59** (3), 1758 (1999).
330. G. Kresse and J. Furthmüller, Physical review B **54** (16), 11169 (1996).
331. R. Dingle, D. Sell, S. Stokowski and M. Ilegems, Physical Review B **4** (4), 1211 (1971).
332. W. Yim, E. Stofko, P. Zanzucchi, J. Pankove, M. Ettenberg and S. Gilbert, Journal of Applied Physics **44** (1), 292-296 (1973).
333. F. Yun, M. A. Reshchikov, L. He, T. King, H. Morkoç, S. W. Novak and L. Wei, Journal of applied physics **92** (8), 4837-4839 (2002).
334. A. Van de Walle, P. Tiwary, M. De Jong, D. Olmsted, M. Asta, A. Dick, D. Shin, Y. Wang, L.-Q. Chen and Z.-K. Liu, Calphad **42**, 13-18 (2013).
335. C. Freysoldt, J. Neugebauer and C. G. Van de Walle, physica status solidi (b) **248** (5), 1067-1076 (2011).
336. C. Freysoldt, B. Grabowski, T. Hickel, J. Neugebauer, G. Kresse, A. Janotti and C. G. Van de Walle, Reviews of modern physics **86** (1), 253 (2014).
337. P. Rinke, M. Winkelnkemper, A. Qteish, D. Bimberg, J. Neugebauer and M. Scheffler, Physical Review B **77** (7), 075202 (2008).
338. M. Suzuki and T. Uenoyama, Journal of applied physics **80** (12), 6868-6874 (1996).